Modelling of galactic cosmic ray electrons in the heliosphere

Rendani Rejoyce Nndanganeni

(B.Sc. Hons.)

20884648

Dissertation accepted in partial fulfillment of the requirements for the degree *Master of Science in Physics* at the Potchefstroom Campus of the North West University

Supervisor: Prof. M.S. Potgieter

Co-Supervisor: Prof. S.E.S. Ferreira

Potchefstroom

February 2012

Abstract

The Voyager 1 spacecraft is now about 25 AU beyond the heliospheric termination shock and soon it should encounter the outer boundary of the heliosphere, the heliopause. This is set to be at 120 AU in the modulation model used for this study. This implies that Voyager 1, and soon afterwards also Voyager 2, should be able to measure the heliopause spectrum, to be interpreted as the lowest possible local interstellar spectrum, for low energy galactic electrons (1 MeV to 120 MeV). This could give an answer to a long outstanding question about the spectral shape (energy dependence) of the galactic electron spectrum at these low energies. These in situ electron observations from Voyager 1, until the year 2010 when it was already beyond 112 AU, are used for a comparative study with a comprehensive three dimensional numerical model for the solar modulation of galactic electrons from the inner to the outer heliosphere.

A locally developed steady state modulation model which numerically solves the relevant heliospheric transport equation is used to compute and study modulated electron spectra from Earth up to the heliopause. The issue of the spectral shape of the local interstellar spectrum at these low energies is specifically addressed, taking into account modulation in the inner heliosheath, up to the heliopause, including the effects of the transition of the solar wind speed from supersonic to subsonic in the heliosheath. Modulated electron spectra from the inner to the outer heliosphere are computed, together with radial and latitudinal profiles, focusing on 12 MeV electrons. This is compared to Voyager 1 observations for the energy range 6-14 MeV. A heliopause electron spectrum is computed and presented as a new plausible local interstellar spectrum from 30 GeV down to 10 MeV.

The comparisons between model predictions and observations from Voyager 1 and at Earth (e.g. from the PAMELA mission and from balloon flights) and in the inner heliosphere (e.g. from the Ulysses mission) are made. This enables one to make conclusions about diffusion theory applicable to electrons in the heliosphere, in particular the rigidity dependence of diffusion perpendicular and parallel to the local background solar magnetic field. A general result is that the rigidity dependence of both parallel and perpendicular diffusion coefficients needs to be constant below $P < 0.4$ GV and only be allowed to increase above this rigidity to assure compatibility between the modeling and observations at Earth and especially in the

outer heliosphere. A modification in the radial dependence of the diffusion coefficients in the inner heliosheath is required to compute realistic modulation in this region. With this study, estimates of the intensity of low energy galactic electrons at Earth can be made. A new local interstellar spectrum is computed for these low energies to improve understanding of the modulation galactic electrons as compared to previous results described in the literature.

Keywords: Cosmic rays, Galactic electrons, Heliosphere, Heliosheath, Very local interstellar spectrum, Heliospheric modulation, Electron modulation, Electron transport

Opsomming

Die Voyager 1 ruimtetuig is reeds 25 AU verby die sonwind-terminasieskok en behoort binnekort die buitenste grens van die heliosfeer te bereik. Hierdie grens word die heliopouse genoem en word vir hierdie studie op 120 AU in die modulasiemodel gestel. Dit impliseer dat Voyager 1 binnekort, en kort daarna ook Voyager 2, die spektra van galaktiese kosmiese strale by die heliopouse te meet. Hierdie waargenome spektra kan vertolk word as die laagste lokale interstellêre spektra, in besonder vir lae-energie galaktiese elektrone (1 MeV tot 120 MeV). Dit behoort ‘n antwoord te gee op ‘n langkwelende vraag oor die spektraalvorm (energie-afhanklikheid) van die galaktiese elektronspektrum by lae energie. Hierdie in situ elektronwaarnemings van Voyager 1, tot die jaar 2010 toe die ruimtetuig reeds by 112 AU was, word in hierdie verhandeling gebruik om ‘n vergelykende studie te maak met die resultate van ‘n omvattende drie-dimensionele numeriese model. Hierdie model beskryf die heliosferiese modulasie van galaktiese elektrone van die binneste tot die buitenste heliosfeer.

‘n Tydsonafhanklike model wat plaaslik ontwikkel is, word gebruik om die transportvergelyking op te los. Elektronspektra word bereken en gebruik om die modulasie van galaktiese elektrone van die Aarde tot by die heliopouse te bestudeer. Die kwessie van wat die spektraalvorm van die lokale interstellêre spektrum by hierdie lae energie is, word spesifiek bestudeer. Dit word gedoen met inagneming van modulasie in die binneste heliomantel, vanaf die terminasieskok tot by die heliopouse. Die uitwerking van die oorgang van die sonwind-spoed in die heliomantel van supersonies tot subsonies word in ag geneem. Gemoduleerde elektronspektra word bereken, tesame met radiale en breedtegraadsprofiele, met die klem op 12 MeV elektrone. Dit word vergelyk met Voyager 1 waarnemings vir 6-14 MeV. ‘n Heliopause-spektrum vir elektrone word bereken en aangebied as ‘n nuwe geloofwaardige lokale interstellêre spektrum vanaf 30 GeV tot by 10 MeV.

Die vergelykende studie word tussen die modelvoorspellings en waarnemings gemaak, spesifiek met data vanaf Voyager 1, by die Aarde (bv. die PAMELA-missie en ballonvlugte) en in die binneste heliosfeer (bv. die Ulysses-ruimtesending). Dit word gebruik om gevolgtrekkings te maak oor diffusieteorie van toepassing op elektrone in die heliosfeer, oor die styfheidsafhanklikheid van diffusie loodreg en parallel aan die agtergrond magnetiese veld. ‘n Algemene bevinding is dat die styfheidsafhanklikheid van beide die parallelle en

loodregte diffusiekoëffisiënte konstant moet bly onder 0.4 GV maar toeneem bo hierdie grens. Dit word vereis om die modellering met waarnemings versoenbaar te maak, by die Aarde maar veral in die buitenste heliosfeer. ‘n Wysiging in die radiale afhanklikheid van die diffusiekoëffisiënte in die binneste heliomantel is nodig om realistiese modulasie vir hierdie streek te bereken. Met hierdie studie kan ‘n goeie raming van die intensiteit van galaktiese elektrone by die Aarde gemaak word. ‘n Nuwe plaaslike interstellêre spektrum is bereken om kennis en begrip van die modulasie van 12 MeV galaktiese elektrone te verbeter, en in vergelyking met vorige resultate wat in die literatuur beskryf is.

Steutelwoorde: Kosmiese strale, Galaktiese elektrone, Heliosfeer, Heliomantel, Nabye lokale interstellêre spektrum, Heliosferiese modulasie, Elektron modulasie, Elektrontransport

Nomenclature

3D	Three-Dimensional
ACRs	Anomalous Cosmic Rays
AMS	Alpha Magnetic Spectrometer
AU	Astronomical units = 1.49×10^{8} km
CIRs	Corotating Interaction Regions
CME	Coronal Mass Ejection
CRs	Cosmic Rays
DCs	Diffusion Coefficients
DR	Distributed reacceleration
DRD	Diffusive reacceleration with damping
ESA	European Space Agency
GCR	Galactic Cosmic Ray
GCRs	Galactic Cosmic Rays
GS	Galactic Spectra
HCS	Heliospheric Current Sheet
HMF	Heliospheric Magnetic Field
HP	Heliopause
IS	Interstellar spectra
LIS	Local Interstellar Spectra
LISM	Local Interstellar Medium
MFP	Mean Free Path
NASA	National Aeronautic and Space Administration
PAMELA	Payload for Antimatter/ Matter Exploration and Light-nuclei Astrophysics
PD	Plain Diffusion
QLT	Quasi-Linear Theory
SEPs	Solar Energetic Particles
SOHO	Solar and Heliospheric Observatory
TPE	Transport Equation
TS	Termination Shock
VLIS	Very Local Interstellar Spectra

TABLE OF CONTENTS

Chapter 1

Introduction

Galactic cosmic rays (GCRs) are charged particles produced from astrophysical sources far from the heliosphere (e.g. supernova explosions). These particles have kinetic energies from ~ 1 MeV up to 10^{11} GeV, and are transported from the galaxy, and beyond, into the solar system and eventually up to Earth.

Low energy galactic electrons (1 MeV to 120 MeV) inside the heliosphere have become a very interesting topic to study since the two Voyager spacecraft crossed the heliospheric termination shock and moved into the heliosheath. These features of the heliosphere will be described in the following chapters. Recently, both spacecraft have returned electron spectra in the mentioned energy range, observed from the termination shock to well inside the inner heliosheath, making it possible to do more detailed modeling of these particles in the outer heliosphere. This should give answers to long outstanding questions as to, how the low energy galactic electron spectrum looks like below 100 MeV, what determines the modulation of these electrons inside the heliosheath, what the rigidity dependence is of the relevant diffusion coefficients at these energies, and what the galactic electron intensity is at Earth.

The transport of these particles inside the heliosphere is described adequately by the heliospheric transport equation, containing most of the physics needed to fully understand the solar modulation of these particles. This equation, applied to a three-dimensional (3D) heliosphere, must however be solved numerically when used to study the solar modulation of GCRs. This model will be described in the thesis.

In this study a 3D numerical model of Ferreira (2002) is used and applied to study the modulation of galactic electrons, from the inner to the outer heliosphere, in terms of spectra, radial and latitudinal profiles at various energies but particularly for 12 MeV radial profiles. This is done by taking into account also the transition of the solar wind speed from supersonic to subsonic in the inner heliosheath.

A particular aim of this study is to determine a new galactic spectrum (as initial input spectrum for modulation models) for low energy electrons by comparing Voyager 1 observations and the results of the applied model. At these low energies galactic propagation models, such as GALPROP Strong et al. (2007), seem inadequate because of lack of understanding turbulence in the galaxy, especially when it comes to the local interstellar medium. Another objective is to use the comparison between the model and the observations to determine the rigidity dependence of the relevant diffusion coefficients used in the model and to establish how this may change from the inner to the outer heliosphere. Subsequently, the model will be used to predict the intensity of these low energy galactic electrons at Earth, an aspect of electron modulation that is controversial because around 10 MeV electrons from Jupiter are dominating the galactic component.

The structure of this thesis is as follows

Chapter 2: The reader is introduced to the basic concepts about cosmic rays and the heliosphere. This includes a brief discussion of the Sun, the solar wind, the heliospheric magnetic field (HMF) and the geometry of the heliosphere. A broad classification of cosmic rays is given with the focus on galactic electrons since they are the main focus of this study. Lastly, the spacecraft missions relevant to the study will be briefly discussed.

Chapter 3: The theory and the numerical model of the heliospheric modulation of GCRs will be discussed, including a brief history of 3D modulation models and a discussion of the relevant transport equation and modulation processes, without going into too much detail. Aspects of the diffusion tensor, such as its spatial and rigidity dependence, will be discussed with the focus on parallel and perpendicular diffusion. This information will be required for the next three chapters.

Chapter 4: Background and information about published galactic electron spectra will be given, including various approaches that have been presented in the literature on the topic of galactic and local interstellar electron spectra. A few examples will be given and discussed. The chapter will focus on the heliospheric modulation of these electrons, using two particular galactic spectra as input for the 3D modulation model. It will be shown that the two selected input spectra do not give good compatibility with Voyager observations and that this development leads to determining a new local interstellar spectrum for galactic electrons, as

an outcome of this study. The consequences for the diffusion coefficients required in the numerical model will be shown and critically discussed.

Chapter 5: The modeling of 12 MeV galactic electrons in the heliosheath using the new local interstellar spectrum will be given as derived in Chapter 4. The transition of the solar wind speed in the heliosheath will be taken into account and the computed results will be compared to Voyager 1 observations, especially for 2010 when it was just beyond 112 AU, which is already well into the inner heliosheath. Spectra at 90 AU and 110 AU will also be computed at three different polar angles. The polar dependence of 12 MeV electron intensities at the above mentioned radial distances will also be shown, as well as the radial intensity profiles of these electrons in the outer heliosphere. Comparisons between modeling solutions and Voyager 1 observations in the energy range of 6-14 MeV will be done in particular. A conclusion about a suitable local interstellar electron spectrum will be made.

Chapter 6: The modeling of 12 MeV galactic electrons will be continued but from the inner to the outer heliosphere using the new LIS derived Chapter 5. Spectra at Earth and in the outer heliosphere will be shown to establish how the modulation pattern changes from the inner to the outer heliosphere. The radial and latitudinal gradients of these low energy electrons will be computed. The polar dependence of the electron intensities from the inner and the outer heliosphere will be given here in order to have a complete picture of how different it is at Earth compared to the outer heliosphere. The computed radial dependence of these electrons will be presented from Earth to the heliopause. The results at 12 MeV will be compared to the Voyager 1 observations for 6-14 MeV. Conclusions about the diffusion coefficients selected for this study will be made.

Chapter 7: A summary of the work as presented in this study will be given along with the main results and conclusions. Pending aspects and future prospects related to this study will be listed and discussed.

Chapter 2

Cosmic rays, the Sun and the Heliosphere

2.1. Introduction

In this chapter the reader is introduced to the basic concepts that are important to galactic cosmic ray (GCR) modulation in the heliosphere. An overview is given about the main features of GCRs and the so-called anomalous component, the Sun, the solar wind, and the heliospheric magnetic field. The heliospheric geometry and its structure are also introduced. Relevant spacecraft missions are briefly discussed, in particular the Voyager 1 and Voyager 2 missions, the Ulysses mission and the PAMELA mission.

2.2. Cosmic rays in the heliosphere

Cosmic rays (CRs) are charged particles (not rays), which after being accelerated to very high energies at e.g. supernova shocks, propagate through the galaxy towards the solar system. These particles were discovered by Victor Hess during the historic balloon flights between 1911 and 1912, when it was established that these particles were from an extraterrestrial origin. They were later called cosmic rays by Millikan. As reviewed by Simpson (1997) and Fichtner (2001), Compton and Clay had shown in 1930 that these particles were electrically charged (fully ionized). Today it is known that they have kinetic energy E from ~ 1 MeV to as high as 3×10^{21} eV (Beatty and Westerhoff 2009). Those that are detected at Earth around a few GeV consist of ~ 97 % protons, ~ 2 % electrons and positrons, and ~ 1 % heavier nuclei, such as Helium, Carbon, Oxygen, Iron etc. These nuclei consist of various isotopes, with a composition slightly different from their solar abundance (see e.g. Longair 1990; Simpson

1992). CRs, in the general context of charged particles, are usually divided into four distinctive populations.

(1) Galactic Cosmic Rays (GCRs) which originate far outside the solar system. It is believed that they are accelerated during supernova explosions and subsequent blast waves; see the detailed review by Jones and Ellison (1991). These charged particles experience the galactic wind and magnetic field before entering interplanetary space so that their original position of creation is hidden.

(2) Anomalous Cosmic Rays (ACRs) are formed due to ionization of interstellar neutral atoms relatively close to the Sun, which then, as charged particles, get picked-up by the solar wind and transported outwards (away from the Sun) to be accelerated at the solar wind termination shock (Garcia-Munoz et al. 1973; Fichtner 2001). As they propagate back to Earth, they experience modulation in energy and number density (intensity). The degree to which ACRs are modulated in the heliosphere changes with the solar cycle (Fisk 1979). The process of their acceleration in the outer heliosphere has recently become highly controversial (see e.g. Potgieter 2008; Potgieter and Strauss 2010; Strauss 2010; Strauss et al. 2010).

(3) Solar Energetic Particles (SPEs) originate from solar flares especially when the Sun gets more active (Forbush 1946). The interplanetary medium, through diffusive shock acceleration, following on coronal mass ejections can also produce these particles. SPEs usually have energies up to several hundred MeV, but are observed only for a few hours before they dissipate. (Remark: strictly speaking these charged particles, also ACRs, should not be called cosmic rays).

(4) Jovian electrons that originate from Jupiter's large magnetosphere. They dominate the low energy electron spectrum within the first 10 AU from the Sun (see e.g. Ferreira 2002; reviews by Potgieter 2008, and Ferreira and Potgieter 2004).

Galactic electrons originate as primary GCRs from astrophysical phenomena such as supernova explosions distributed throughout the galaxy. They penetrate the heliosphere isotropically to be modulated by four physical processes, which will be briefly described in section 3.3. They differ from the nuclear component in the sense that they are less massive, and of course, oppositely charged, making it significantly more difficult to measure their intensities. Until recently, space experiments could not distinguish between electrons and positrons and thus present observations as the sum of electrons and positrons. As mentioned

above, Jovian electrons up to 50 MeV dominate in the equatorial regions of the heliosphere, up to distances of ~20 AU from the Sun but not in the polar regions of the heliosphere at 1 AU. Ferreira et al. (2001b) and Moeketsi (2004) studied Jovian electron modulation in detail. Galactic electrons are the main focus of this thesis.

2.3. The Sun

The Sun is a dynamically active magnetic star that forms the basis of the solar system and sustains life on Earth by being the source of light and heat. It contains about ~ 98% of the total mass of the solar system and consists of ~ 90% Hydrogen and ~ 10% Helium with a small fraction of heavier elements. Its atmosphere consists of four layers: the photosphere, the chromosphere, the transition region and the corona.

Figure 2.1 shows this basic structure of the Sun. The first layer is the photosphere which is the apparent solar surface and it emits most of the Sun's light and heat. The second layer is the chromosphere, a layer clearly visible during a solar eclipse. It extends some 10^3 km above the photosphere. The temperature on this layer increases from a surface temperature of 4300 K to about 10^4 K owing to the absorption of acoustic waves emerging from the convective zone. The third layer is the transition region above the chromosphere, where the temperature increases rapidly from ~ 10^4 K to 10^6 K. The fourth layer is the solar corona which is observable beyond the chromosphere. This is the region where prominences appear as immense plasma clouds that erupted from the upper chromosphere. This is the outermost tenuous region of the solar atmosphere extending to large distances and eventually becomes the solar wind.

The corona is characterized by very high temperatures, the presence of low density, and fully ionized plasma. Near the solar poles the coronal intensity is generally depressed particularly around solar maximum. The corona has dark extended regions in x-ray solar images called coronal holes. These coronal holes are characterized by low density, cold plasma and unipolar magnetic fields. During solar activity coronal holes cover the north and the south polar caps of the Sun. Coronal holes are regions of very low density and have an open magnetic field structure. This open structure allows very low energy charged particles to escape from the Sun so that coronal holes are the source of solar wind and the exclusive source of high speed components.

Solar activity is characterized by sunspots which are dark spots that appear on the surface of the Sun. They appear dark because they are cooler than their surrounding gas. They develop owing to strong local concentrations of the magnetic field on the solar surface.

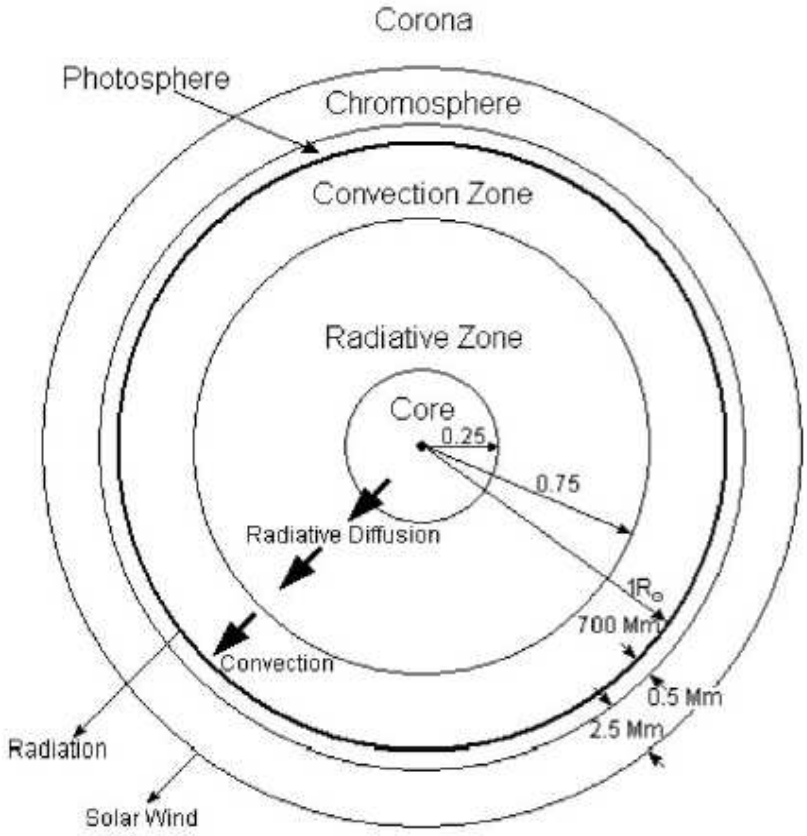

Figure 2.1: This figure shows the basic structure of the Sun, adapted from: www.oulu.fi/spaceweb/textbook/sun.html.

Figure 2.2 shows the monthly averaged sunspot numbers from 1750 to early 2010. During periods of high activity called solar maximum more spots are visible on the surface of the Sun. Periods with less active and few or no sunspots are called solar minima. From the figure it is evident that the Sun has a period of ~11 years called a solar cycle.

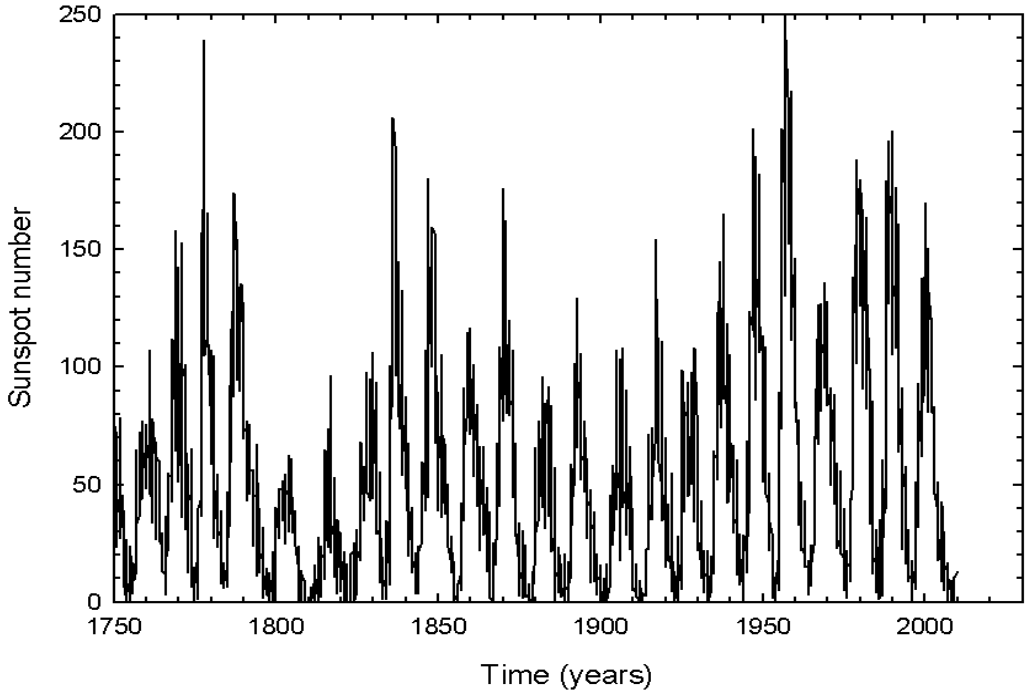

Figure 2.2: Monthly sunspot number from 1750 to early 2010, data from http:/solarscience.msfc.nasa.gov/sunspotcycle.shtml.

2.4. Solar wind

The solar wind constitutes of streams of charged particles ejected from the upper atmosphere of the Sun. It consists of approximately the same number of electrons and protons with few heavier ions. The existence of solar wind was predicted by Ludwig Biermann in 1951 from studying the shape of cometary tails (see review by Fichtner 2001). The first spacecraft to confirm this was the Soviet Lunik 2 and Lunik 3 in 1960. These observations were verified by observations of Marine 2 in 1960.

The theory explaining the solar wind and its characteristics was first introduced by Eugene Parker (Parker 1958). He also proposed the first mathematical model for the solar wind. The source of the solar wind is the Sun's hot corona; the temperature of the corona is so high that the Sun's gravity cannot hold on to it. The solar wind is always flowing in the outward direction and carries magnetic clouds and interaction regions with it. An interaction region forms when the high solar wind stream catches up with the slow solar wind. The high and slow speed streams interact with each other and pass by the Earth as the Sun rotates. The bimodal solar wind flow is most evident near solar minimum. The origin and the acceleration

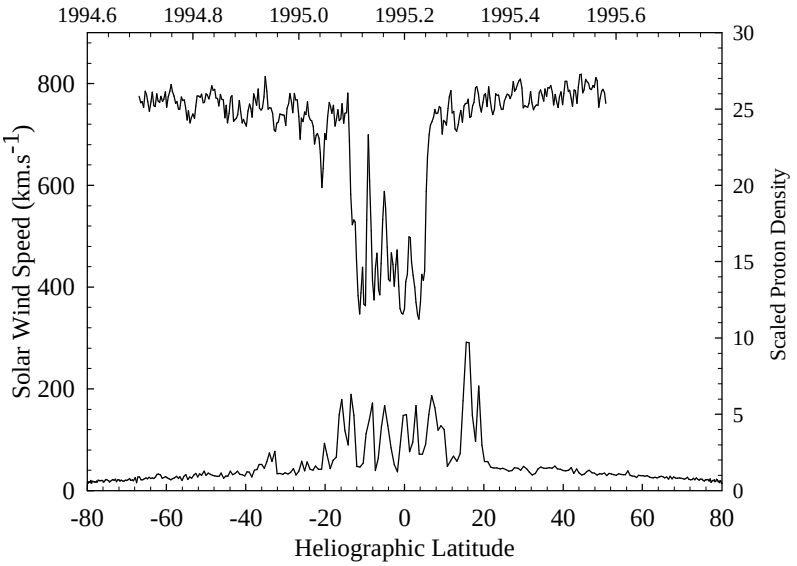

Figure 2.3: Solar wind speed and proton density variations from heliographic pole to pole as observed by Ulysses from 1994 to 1995. Upper plot shows the solar wind speed variation; bottom plot shows the proton density variation. Data obtained from http:/cohoweb.gsfc.nasa.gov.

of the fast and slow solar wind are not well understood, but observations from SOHO (Cranmer 2002) provide new insight. Among the important results obtained from these observations are that the fast and slow wind originates and accelerates in very different ways, related to the global structure of the corona.

The fast solar wind is characterized by speeds of ~750-800 km.s^{-1} with small fluctuations and is directly associated with coronal holes and polar coronal holes and are often stable over a long periods of time. The high speed solar wind is dominant during periods of low solar activity and occupies the whole heliosphere at solar latitude > 20^{o}. The slow solar wind originates from equatorial coronal holes located in the vicinity of active regions and is characterized by an average speed of ~ 450 km.s^{-1} but with very large fluctuations.

For the purpose of this numerical study, the solar wind velocity **V** is assumed as

$$\mathbf{V}(r,\theta) = V(r,\theta)\mathbf{e}_r = V_r(r)V_\theta(\theta)\mathbf{e}_r, \tag{2.1}$$

where r is radial distance in AU, θ the polar angle and $\mathbf{e}_r$ the unit vector component in the radial direction. The radial dependence of the solar wind speed is given by

$$V(r) = V_0 \left\{ 1 - exp\left[\frac{40}{3} \left(\frac{r_\odot - r}{r_0} \right) \right] \right\}, \tag{2.2}$$

with $V_0 = 400\,\text{km.s}^{-1}, r_\odot$ the solar radius, and $r_0 = 1$ AU (e.g. Potgieter 1984).

The latitude dependence of the solar wind speed $V_\theta(\theta)$ during solar minimum conditions is given by

$$V_\theta(\theta) = 1.5 \mp 0.5 \tanh\left[\frac{2\pi}{45^\circ} \left(\theta - 90^\circ \pm \varphi \right) \right]. \tag{2.3}$$

In the northern and southern hemisphere respectively with $\varphi = 35^o$ (e.g. Hattingh 1998). For solar maximum conditions it is assumed to be independent of latitude so that

$$V_\theta(\theta) = 1. \tag{2.4}$$

Figure 2.4 shows the latitude dependence of the solar wind speed as given by Equations (2.3) and (2.4) for solar minimum and maximum conditions, respectively. The solid line shows solar minimum whereas the dotted line shows solar maximum conditions. For solar minimum, the solar wind speed is assumed 400 km.s^{-1} in the equatorial regions, increasing to 800 km.s^{-1} in the polar regions. For solar maximum conditions the solar wind speed on average is 400 km.s^{-1} for all heliolatitudes.

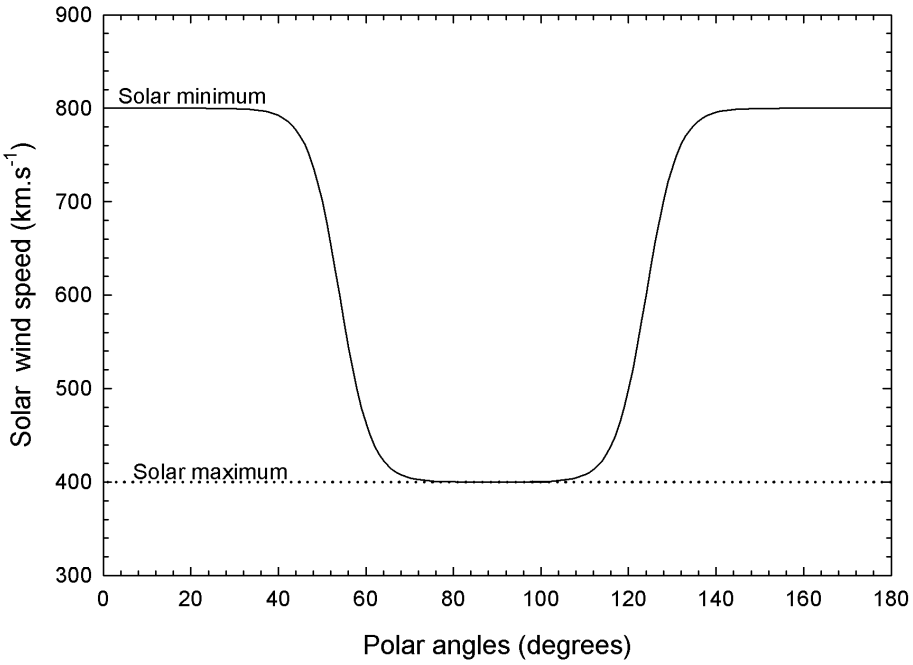

Figure 2.4: Latitude dependence of the solar wind speed for solar minimum and maximum given by Equations (2.3) and (2.4) respectively.

2.5. The heliosphere

The heliosphere exists because of the presence of Sun and the solar wind which excludes the charged particles of the local interstellar medium (LISM) from the vicinity of the Sun. The size and the boundaries of the heliosphere are determined through interaction between the solar wind and the LISM. The internal properties, structure and dynamics of the heliospheric medium are thus defined by the spatial and temporal variability of the solar wind. The most important time scale is imposed by the 11 year cycle.

The volume of space filled with the expanding solar wind is called the heliosphere. It is the modest representative of an astrosphere; an interstellar bubble blown into surrounding interstellar medium by a stellar wind. The extent of the heliosphere depends on the ram pressure of the solar wind compared to the total pressure of the LISM. It is separated from LISM by the heliopause (HP). The heliosphere is believed to be moving at a speed of ~ 25 $km.s^{-1}$ through the interstellar medium. The speed of the local interstellar medium has been estimated from direct measurements of interstellar neutral particles coming into the

heliosphere. The LISM is not an empty space but consist of some combination of dust, neutral gas, plasma, magnetic fields and galactic cosmic rays.

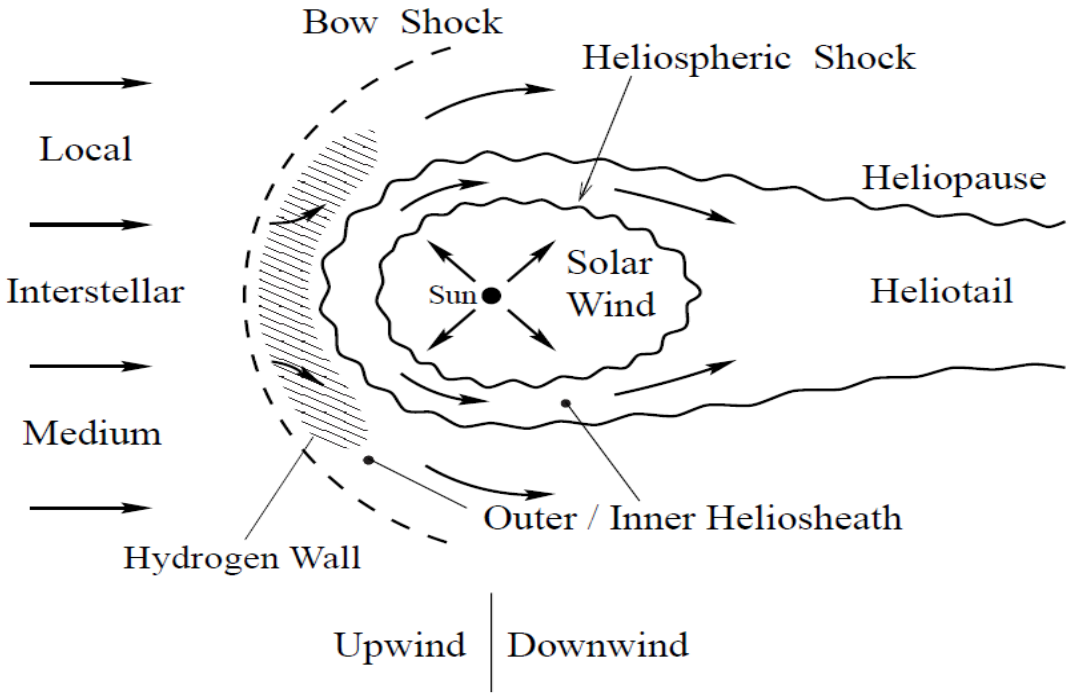

Figure 2.5: Sketch of the heliosphere as seen in the rest frame of the Sun (from Fichtner 2001).

The geometry of the heliosphere, as sketched in Figure 2.5, is globally defined by the mutual interaction between two plasmas, the solar wind plasma and the interstellar medium plasma. Hydrodynamic and magneto-hydrodynamic models are used to calculate the geometry of the heliosphere. Figure 2.6 shows such a contour plot of the heliosphere with computed proton number density and proton speed for an anisotropic solar wind, as occurs during solar minimum periods (Ferreira and Scherer 2004). The results are shown in the rest frame of the Sun, where its motion relative to the LISM appears as the interstellar wind blowing to the left. The dashed lines indicate two structures of importance to GCR modulation, the solar wind termination shock as the oval dashed line and the HP which in this case is an open structure, called the heliotail. The direction in which the heliosphere is moving is called the heliospheric nose. Magneto-hydrodynamic models show similar geometry but with the tail region somewhat narrower, and asymmetries due to the pressure of the interstellar magnetic field.

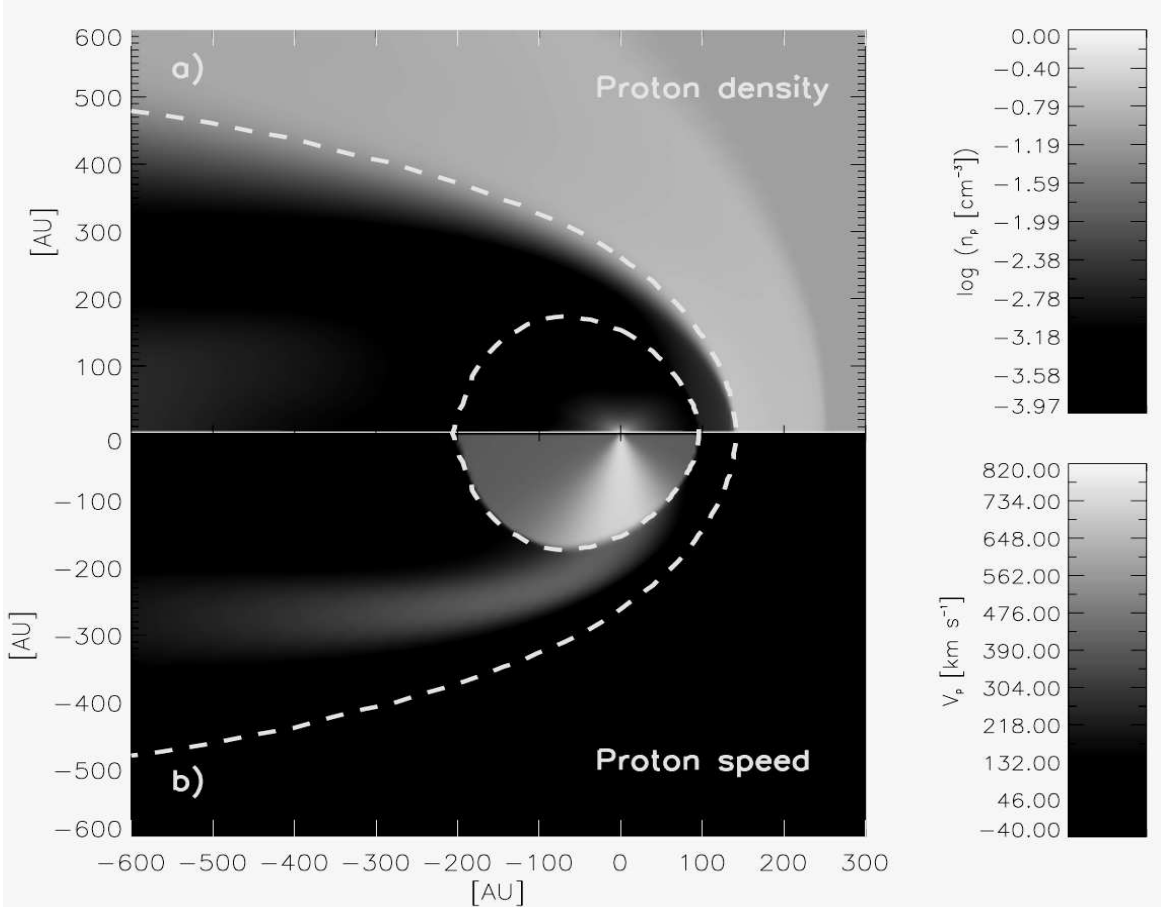

Figure 2.6: Contour plot of the heliosphere showing the computed proton density (top) and proton speed (bottom). Shown by the dashed lines are the positions of the termination shock (dashed oval) and the heliopause (Ferreira and Scherer 2004).

2.5.1. Solar wind termination shock

The region in the heliosphere where the solar wind changes from supersonic speeds to subsonic speeds is called the termination shock (TS). This occurs because of the interaction with the interstellar medium. The existence of the TS was first suggested by Parker in 1961 (Parker 1961). The TS position was estimated to vary from ~ 80 AU and ~ 100 AU (e.g. Stone et al. 1996, Whang and Burlaga 2000), which was pretty close to what the twin Voyager spacecraft observed during their crossings of the TS. In 2004, Voyager 1 crossed the TS at 94 AU (Stone et al. 2005), while Voyager 2 crossed it at 84 AU in 2007 (Burlaga et al. 2008). The TS can be considered as the first important heliospheric boundary away from the Sun, with the main feature that the Sun's supermagnetosonically expanding solar wind abruptly slows to become a submagnetosonic flow, also described as a collisionless shock.

2.5.2. Heliosheath

The heliopause forms where the solar wind and the interstellar medium pressure are in equilibrium, called a contact discontinuity, separating the two plasmas from each other and as such it can be regarded as the outer boundary of the heliosphere. The region between the TS and the HP is called the inner heliosheath whereas the region between the HP and the bow shock is called the outer heliosheath. The shape of the HP is highly asymmetrical, as shown in Figure 2.6, from the nose to the tail. It is well defined in the nose direction predicted to be about 40-50 AU beyond the TS, but it is ill defined in the tail direction so more modeling is required to understand it (e.g. Opher et al. 2009). In the inner heliosheath the solar wind is slower, hotter and denser as it interacts with the surrounding interstellar matter. The heliospheric magnetic field is still frozen into the solar wind plasma and increases in proportion to the increase in plasma density in the inner heliosheath. In this region the slowed solar wind must be diverted backwards away from the upstream medium. In this work the inner heliosheath will simply be referred to as the heliosheath.

2.6. The heliospheric magnetic field

It is important to study and understand the heliospheric magnetic field (HMF) because it plays a significant role in the transportation of the cosmic rays in the heliosphere. It is embedded in the solar wind and rotates with the Sun's rotation period so that it is transported into an Archimedean spiral by the combination of the solar wind’s outward motion and the Sun’s rotation. The solar activity cycle also determines the shape and the structure of this magnetic field. The magnetic field is directed outward from the Sun in one of its hemispheres and inwards in the other. This changes during extreme solar activity when the polarity of the HMF changes, causing a 22 year cycle.

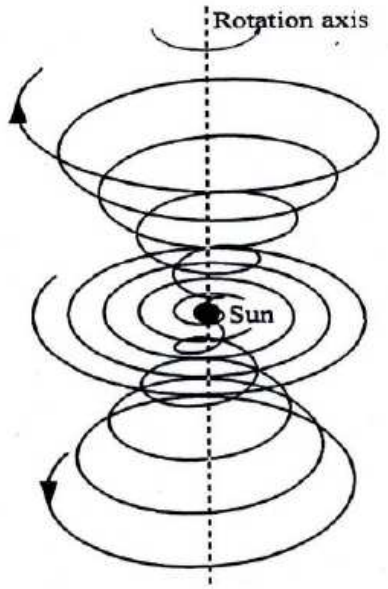

Figure 2.7: A 3D representation of the Parker HMF spiral structure with the Sun at the origin. Spiral rotates around the polar axis, here with polar angles of θ = 45°, θ = 90° and θ = 135°. From Hattingh (1998).

The equation for the HMF spirals as derived by Parker (1958) is:

$$\mathbf{B} = B_0 \left(\frac{r_0}{r} \right)^2 \left(\mathbf{e}_r - \tan\psi \mathbf{e}_\phi \right), \tag{2.5}$$

where $\mathbf{B}$ is the HMF with unit vector components $\mathbf{e}_r$ and $\mathbf{e}_\phi$ in the radial and azimuthal direction respectively. Here φ is the spiral angle defined as the average angle between the radial direction and the average HMF at a certain position. A typical value at Earth is $\psi \approx 45^\circ$, increasing with $\psi \approx 90^\circ$ beyond ~10 AU in the equatorial plane. The magnitude of the HMF at Earth is B_0, with an average value of $B_0 = 5$ nT for solar minimum. The spiral angle is given by

$$\psi = \arctan\left(\frac{\Omega(r - r_\odot)\sin\theta}{V} \right), \tag{2.6}$$

where Ω is the angular speed of the Sun. Substituting Equation (2.6) into (2.5) yields for the magnitude of the HMF

$$B = \frac{B_0 r_0^2}{r^2}\sqrt{1+\left(\frac{\Omega\left(r-r_\odot\right)\sin\theta}{V}\right)^2}. \tag{2.7}$$

The polar angle θ is measured from 0° at the polar axis of the Sun with θ = 90° at the equatorial plane.

Jokipii and Kóta (1989) made a modification to the Parker HMF so that the expression for the HMF becomes

$$B_m = \frac{B_0 r_0^2}{r^2}\sqrt{1+\left(\frac{\Omega\left(r-r_\odot\right)\sin\theta}{V}\right)^2+\left(\frac{r\delta_m}{r_\odot}\right)}, \tag{2.8}$$

with $\delta_m = 8.7\times10^{-5}$ so that for $\delta_m = 0$ the standard Parker geometry will be obtained (see also Langner 2004).

2.7. The heliospheric current sheet

Heliospheric current sheet (HCS) is the surface within the HMF that separates regions where it points toward or away from the Sun, thus dividing the heliosphere into two halves with opposite magnetic polarities. The thickness of the HCS is about 10^{-4} km. The structure of the HCS is shaped by the Sun's rotation causing it to have a wavy structure. This waviness is correlated to solar activity. The angle between the rotation axis of the magnetic field and the Sun's rotation axis is called the tilt angle α.

During solar minimum conditions when solar activity is low, the tilt α is small so that the waviness of the HCS is reduced. During solar maximum, α can be as large as 75^o. Every ~11 years the HMF reverses its polarity, changing sign across the HCS.

For a constant and radial V, the wavy HCS satisfies the following equation given by Jokipii and Thomas (1981):

$$\theta' = \frac{\pi}{2}+\sin^{-1}\left\{\sin\alpha\sin\left[\phi+\frac{\Omega\left(r-r_0\right)}{V}\right]\right\}. \tag{2.9}$$

For small values of α, this equation can be reduced to the equation given by Hattingh (1998)

$$\theta' = \frac{\pi}{2} + \alpha \sin\left[\phi + \frac{\Omega(r - r_0)}{V}\right]. \tag{2.10}$$

To include the polarity of the HMF, Equation (2.5) is modified so that

$$\mathbf{B} = A_c B_0 \left(\frac{r_0}{r}\right)^2 \left(\mathbf{e}_r - \tan\psi \mathbf{e}_\phi\right)\left[1 - 2H\left(\theta - \theta'\right)\right], \tag{2.11}$$

with θ' the polar angle of the HCS and $A_c = \pm 1$ a constant that determines the polarity of the HMF: A > 0 is the period when the magnetic lines are directed outward in the northern hemisphere and inwards in the southern hemisphere, with $A_c = +1$. For A < 0 periods, $A_c = -1$ and the direction of the HMF is reversed.

The Heaviside step function in Equation (2.11) is given by

$$H\left(\theta - \theta'\right) = \begin{cases} 0 \text{ when } \theta < \theta' \\ 1 \text{ when } \theta > \theta' \end{cases}. \tag{2.12}$$

If this function is used directly in the numerical model, the discontinuity causes severe numerical problems (Hattingh 1998 and Langner 2004). To overcome this problem, the step function is approximated by

$$H'\left(\theta - \theta'\right) \approx \tanh\left[2.75\ \left(\theta - \theta'\right)\right]. \tag{2.13}$$

2.8. Solar cycle variations

The Sun has another important cycle, the ~ 22 year cycle, which is directly related to the reversal of the HMF during each period of extreme solar activity. These cycles have been termed A > 0 and A < 0 polarity cycles respectively. The bottom panel of Figure 2.8 shows the long term modulation of GCRs intensities as measured at Earth by the Hermanus neutron monitor.

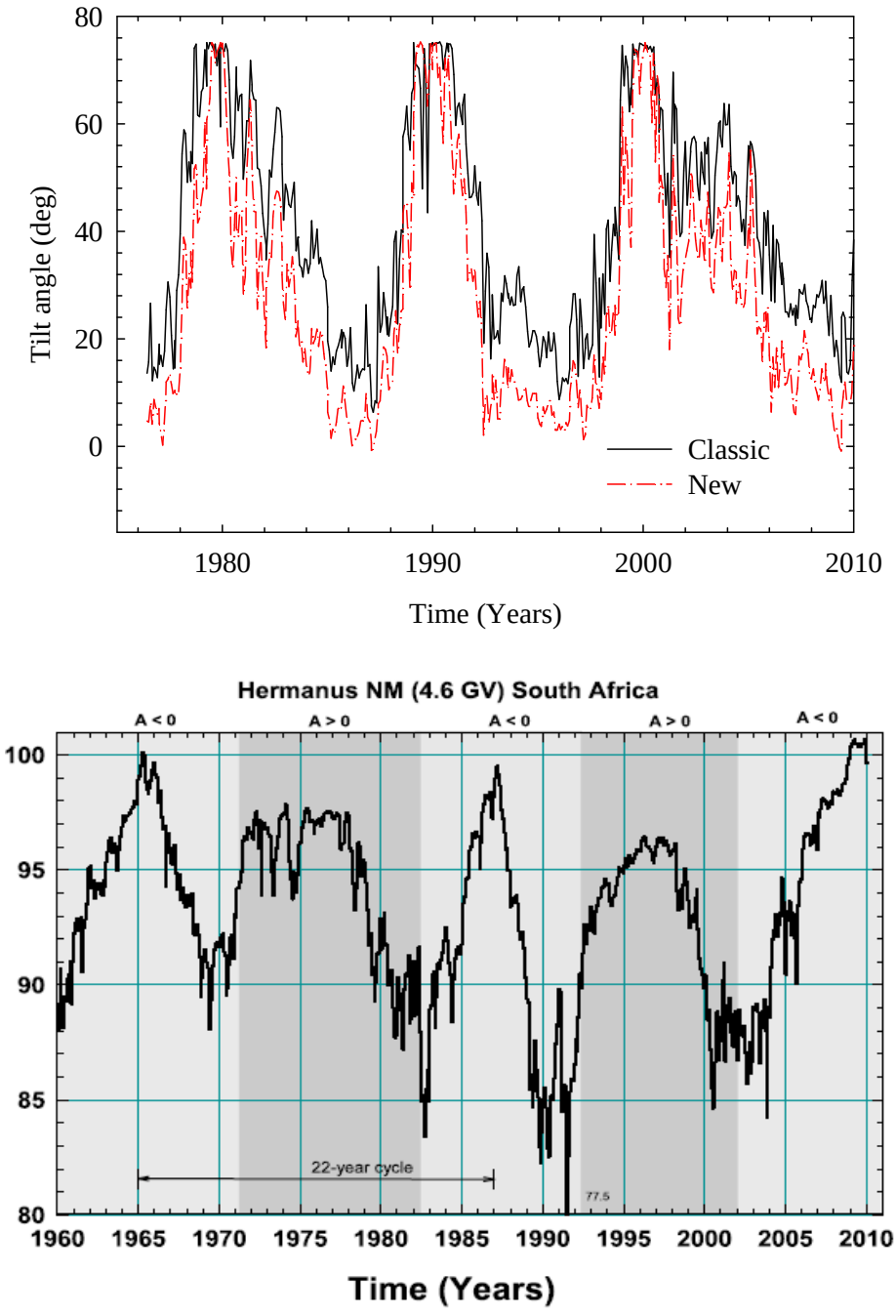

Figure 2.8: Top panel shows the tilt angle α from 1976 until recently Two different models for α are shown namely "new" (dashed dot line) and "classic" (solid line). (Wilcox Solar observatory: http://wso.stanford.edu; see also Hoeksema 1992). Bottom panel shows the long term modulation of GCRs as recorded by the Hermanus neutron monitor in South Africa with a cutoff rigidity of 4.6 GV.

The GCRs intensity time profiles reach maximum values in ~1965, ~1976, ~1987, ~1998 and ~2009 corresponding to solar minimum conditions. Minimum values were observed in 1969-1970, 1981-1982, 1990-1991, 2000-2001 which corresponds to solar maximum conditions. The alternating A > 0 and A < 0 magnetic polarity cycles are indicted in this figure. This means that the present cycle is an A < 0 cycle. The 22 year cycle is also clearly evident.

The top panel of Figure 2.8 shows how the tilt angle is varying with solar activity. Two models are shown, the classic and the new model. The classic model uses a line of sight boundary condition while the new model uses radial boundary conditions at the photosphere to calculate α. For both models, α varies from a minimum of ~5° to 10° (at solar minimum activity) to higher values with increased solar activity with α ~75° the observed maximum.

2.9. Spacecraft missions

In this section different spacecraft missions relevant to this study are briefly discussed.

2.9.1. Ulysses mission

The Ulysses mission was a joint venture between the European Space Agency (ESA) and the National Aeronautic and Space Administration (NASA). The spacecraft was launched on 6 October 1990 with its main objective to explore the 3D heliosphere and to gain understanding of the dynamic heliosphere in the heliospheric polar regions. It was the first spacecraft to take measurements far above the ecliptic plane, over the polar regions of the Sun, obtaining firsthand knowledge concerning the high latitudes of the inner heliosphere with r < ~5 AU.

After its launch, the spacecraft stayed close to the ecliptic plane to reach Jupiter at ~5 AU from where it started to move to higher heliolatitudes south of the ecliptic plane. In the mid-1994 the highest southern point was reached at minimum solar activity. Ulysses moved to the northern polar region and reached it in mid-1995, returning to the equatorial plane region again in 1998. It started the second out-of- ecliptic orbit after 1998 by moving into the southern heliospheric regions.

The mission was highly successful and had contributed significantly to the current knowledge regarding the inner heliosphere. Several major discoveries were made e.g. the strong latitude

dependence of the solar wind speed changing with solar activity. Concerning GCRs, the main discoveries and highlights were discussed in several reviews, the recent ones by Heber and Potgieter (2006, 2007). For more detailed information about the spacecraft mission, see also the NASA Ulysses homepage at htttp://ulysses.jpl.nasa.gov/.

2.9.2. Voyager mission

The twin Voyager spacecraft, called Voyager 1 and Voyager 2, have made GCRs, solar wind and magnetic field observations for more than three decades. These observations have been used to study the spatial and temporal variations of GCRs and ACRs at distances now extending beyond 95 AU. The two spacecraft were launched in 1977, Voyager 2 first in August, and Voyager 1 in September. The spacecraft have thus been in flight for almost 35 years. They are the first and so far only spacecraft to study the outer solar system, the TS and now the heliosheath. The spacecraft also returns data about the HMF but unfortunately the solar wind detector is not working.

The first objectives were to explore and study the planets Jupiter and Saturn, but Voyager 2 also went by the giant planets Uranus and Neptune. Voyager 1 is speeding away at ~ 3.5 AU per year, out of the ecliptic plane at a heliolatitude of 34.4°, whereas Voyager 2 travels at ~ 3.3 AU per year, out of the ecliptic plane at a heliolatitude of -28.8° (i.e. below the equatorial plane). Voyager 1 was the first to cross the TS in 2004 at a distance of 94 AU and it has been exploring the heliosheath since. This knowledge has been very handy in modulation studies and modeling and will continue to be so for another decade. Voyager 2 crossed the TS in 2007 at 84 AU that is 10 AU closer to the Sun than Voyager 1. This is confirmation that the shock is not stationary, it moves inwards and outwards depending on solar activity (see e.g. Snyman 2007 and Intriligator and Webber 2011).

Both Voyagers are heading towards the HP nose, the region that is separating the solar wind plasma from the interstellar plasma, and the heliosphere from the local interstellar medium. Voyager 1 is currently at 118.9 AU meaning that it should reach the HP within the next year or so. This region has never been explored before by any spacecraft. Voyager 2 is currently at 96.6 AU. The two are expected to operate until 2020, and maybe by then Voyager 1 could be exploring the local interstellar medium. For the vast number of discoveries and accomplishments of this mission, see reviews by Stone et al. (2008), Richardson et al. (2008)

and Krimigis et al. (2011). For more information about the mission see: http:// voyager.jpl.nasa.gov/mission/intersterllar.html.

2.9.3 PAMELA mission

This is a satellite-borne experiment making long duration measurements of cosmic rays, particularly optimized for their antiparticles such as positrons and anti-protons. It was launched on June 15th, 2006 from the Bajkonur cosmodrome on-board of the Resurs DK1 satellite, and since then, has continued to make cosmic ray observations following a high inclination elliptical orbit with a period of 90 minutes. It is also suited to study particles of solar origin and particles trapped in the Earth's magnetosphere.

The main scientific objective is the simultaneous observations of cosmic ray antiprotons and positrons, performed in the most extended energy range to date (100 MeV to at least 100 GeV). The mission will continue until the satellite fails, hopefully not in the next few years. A major discovery was the large positron excess with respect to electrons between 10 GeV and 100 GeV as well as discovery of antiprotons being trapped in the radiation belts around the Earth (Adriani et al. 2011). For other accomplishments of this mission, see publications and reviews by Adriani et al. (2009), Picozza.et al. (2007), Boezio et al. (2009, 2011), and Mocchiutti et al. (2009). For more detailed information about the PAMELA mission visit its official website, http://pamela.roma2.infn.it.

2.10. Summary

In this chapter the basic concepts that are important to the modulation modeling of GCRs in the heliosphere were given and briefly discussed. A short introduction was given on the various populations of cosmic rays and their origin, the Sun, the heliosphere and its geometry, the HMF and HCS, the solar wind and the solar cycles. Three spacecraft missions were also discussed. The next chapter will give a brief overview about the numerical model, the transport equation and the heliospheric diffusion tensor.

Chapter 3

Heliospheric modulation of galactic cosmic ray: Theory and models

3.1. Introduction

The modulation of GCRs is the process by which their intensities change as a function of position, time and energy as they propagate from the local interstellar medium into the heliosphere. These fully charged galactic particles have to cross various heliospheric boundaries and regions, as described in the previous chapter, on their way to the point of observation. The transport and propagation processes are described by a basic transport equation with several important mechanisms: convection, diffusion, gradient, curvature and HCS drifts and adiabatic cooling (or heating) as discussed briefly in section 3.3. This equation was developed by the Eugene Parker in the early 1960's (Parker 1965) and verified by Gleeson and Axford (1967) and Fisk et al. (1974), and refined by Gleeson and Axford (1968) and Jokipii and Parker (1970).

3.2. The 3D modulation model

For the past four decades GCRs models, in particular numerical models, have been developed with increasing complexity, from steady state to comprehensive time dependent models, including the TS with diffusive shock acceleration. For a brief overview of the history of the development of these models, see Ferreira (1998), Langner (2000, 2004) and references therein. Here a brief overview of a locally developed 3D steady state model as used in this work is given.

Kóta and Jokipii (1983) were the first to develop a full 3D steady state drift model, followed by Williams (1990), Hattingh (1998) and Gil and Alania (2001). Fichtner et al. (2000) developed a 3D steady state non-drift model which included the Jovian magnetosphere as a

source for low energy electrons. In 2001, Ferreira et al. (2001a,b) developed a 3D steady state drift model which included gradient, curvature and current sheet drifts and the Jovian magnetosphere as a source of low energy electrons (see also Ferreira et al. 2001a, b). The motivation for developing this model was the Ulysses observations which revealed 3D modulation effects in the inner heliosphere. These steady state models describe solar cycle effects as a series of steady solutions with each solution containing solar activity related changes in the modulation parameters such as the solar wind, the various diffusion coefficients and the Jovian electron source, neglecting strong time dependent effects such as the reacceleration of GCRs at the TS. This model is the departure point of this study but neglecting Jovian electrons. The latter was studied before by Moeketsi (2004) and Nkosi (2006) – see also Moeketsi et al. (2005) and Nkosi et al. (2008). For this thesis, the focus is on the modulation of GCRs electrons.

3.3. The transport equation

The transport equation is given by

$$\frac{\partial f}{\partial t} = -\mathbf{V}.\nabla f + \nabla.\left(\mathbf{K}.\nabla f\right) + \frac{1}{3}\left(\nabla.\mathbf{V}\right)\frac{\partial f}{\partial \ln P} + Q_{source}, \tag{3.1}$$

where $f(\mathbf{r}, P, t)$ is the omni-directional cosmic ray distribution function dependent on position **r**, rigidity P and time *t*. The rigidity is defined as the momentum per charge for a given species of particles, and is given by $P = pc/q$ where p is the particle momentum, q is the particle's charge and c is the speed of light in empty space; **V** is the solar wind velocity and **K** the diffusion tensor. This TPE includes the following processes:

- The term on the left side describes the change in the CRs distribution with time.
- The first term on the right describes the outward directed particle convection caused by the radially expanding solar wind.
- The second term on the right depends on the diffusion tensor which describes the spatial diffusion parallel and perpendicular to the average HMF of these particles, as well as gradient and curvature drifts of GCRs including any abrupt change in the HMF such as the HCS.

- The third term describes energy changes in the form of adiabatic cooling or heating and acceleration of particles at shocks.
- The last term describes possible sources of CRs inside the heliosphere, e.g. ACRs or the Jovian electron source.

The transport equation in a heliocentric, spherical coordinate system and for a steady state with $\frac{\partial f}{\partial t} = 0,$ is given by

$$\overbrace{\left[\frac{1}{r^2}\frac{\partial}{\partial r}(r^2 K_{rr}) + \frac{1}{r\sin\theta}\frac{\partial K_{\phi r}}{\partial \phi}\right]\frac{\partial f}{\partial r} + \left[\frac{1}{r^2\sin\theta}\frac{\partial}{\partial \theta}(K_{\theta\theta}\sin\theta)\right]\frac{\partial f}{\partial \theta}}^{diffusion}$$
$$+\overbrace{\left[\frac{1}{r^2\sin\theta}\frac{\partial}{\partial r}(rK_{r\phi}) + \frac{1}{r^2\sin\theta}\frac{\partial K_{\phi\phi}}{\partial \phi}\right]\frac{\partial f}{\partial \phi}}^{diffusion} +$$
$$\overbrace{K_{rr}\frac{\partial^2 f}{\partial r^2} + \frac{K_{\theta\theta}}{r^2}\frac{\partial^2 f}{\partial \theta^2} + \frac{K_{\phi\phi}}{r^2\sin^2\theta}\frac{\partial^2 f}{\partial \phi^2} + \frac{2K_{r\phi}}{r^2\sin\theta}\frac{\partial^2 f}{\partial r\partial \phi}}^{diffusion}$$
$$+\overbrace{\left[-\left\langle \mathbf{v}_d \right\rangle_r\right]\frac{\partial f}{\partial r} + \left[-\frac{1}{r}\left\langle \mathbf{v}_d \right\rangle_\theta\right]\frac{\partial f}{\partial \theta} + \left[-\frac{1}{r\sin\theta}\left\langle \mathbf{v}_d \right\rangle_\phi\right]\frac{\partial f}{\partial \phi}}^{drift}$$
$$\overbrace{-V\frac{\partial f}{\partial r}}^{convection} \overbrace{+\frac{1}{3r^2}\frac{\partial}{\partial r}(r^2 V)\frac{\partial f}{\partial \ln P}}^{adiabatic\ energy\ change}$$
$$= \overbrace{-Q}^{sources} \tag{3.2}$$

where $K_{rr}, K_{r\theta}, K_{r\phi}, K_{\theta r}, K_{\theta\theta}, K_{\theta\phi}, K_{\phi r},$ $K_{\phi\theta}$ and $K_{\phi\phi}$ are the elements of the diffusion tensor **K**, discussed further in the next section.

The three components of the drift velocity are related to these tensor elements as follows

$$\left\langle \mathbf{v}_d \right\rangle_r = -\frac{sign(Bq)}{r\sin\theta}\frac{\partial}{\partial \theta}(\sin\theta K_{\theta r}), \tag{3.3}$$

$$\left\langle \mathbf{v}_d \right\rangle_\theta = -\frac{sign(Bq)}{r}\left[\frac{1}{\sin\theta}\frac{\partial}{\partial \phi}(K_{\phi\theta}) + \frac{\partial}{\partial r}(rK_{r\theta})\right], \tag{3.4}$$

$$\left\langle \mathbf{v}_d \right\rangle_\phi = -\frac{sign(Bq)}{r}\frac{\partial}{\partial\theta}\left(K_{\theta\phi}\right). \tag{3.5}$$

Alternatively the drift velocity vector is described by

$$\mathbf{v}_d = \nabla\times K_A\mathbf{e}_B = \nabla\times\left(K_A\mathbf{e}_B\right)\left[1-2H\left(\theta-\theta'\right)\right]+2\delta_D\left(\theta-\theta'\right)\left(K_A\mathbf{e}_B\right)\times\nabla\left(\theta-\theta'\right), \tag{3.6}$$

with $\mathbf{e}_B = \frac{\mathbf{B}_m}{B}$, with $\mathbf{B}_m$ the modified HMF given by Equation (2.8) and H is the Heaviside step function. Here, K_A is the drift coefficient (described below) related to the geometry of the HMF and δ_D is the Dirac delta function (see also Hattingh 1998).

3.4. The diffusion tensor

The heliospheric tensor **K** can be written in terms of diffusion and drift coefficients orientated with respect to the direction of the background HMF:

$$\mathbf{K} = \begin{bmatrix} K_\parallel & 0 & 0 \\ 0 & K_{\perp\theta} & K_A \\ 0 & -K_A & K_{\perp r} \end{bmatrix} \tag{3.7}$$

Where $K_\parallel$ is the diffusion coefficient parallel to the mean HMF, $K_{\perp\theta}$ and $K_{\perp r}$ denote the diffusion coefficient perpendicular to the mean HMF in the polar and radial direction respectively, with the off-diagonal element K_A describing gradient, curvature and HCS drifts of GCRs in the large scale HMF. In order to find the elements of this tensor in a heliocentric spherical coordinate system as in Equation (3.2), the transformation matrix is used:

$$\mathbf{T} = \begin{bmatrix} \cos\psi & 0 & \sin\psi \\ 0 & 1 & 0 \\ -\sin\psi & 0 & \cos\psi \end{bmatrix} \tag{3.8}$$

where ψ is the spiral angle of the HMF given by Equation (2.6). This gives

$$\begin{bmatrix} K_{rr} & K_{r\theta} & K_{r\phi} \\ K_{\theta r} & K_{\theta\theta} & K_{\theta\phi} \\ K_{\phi r} & K_{\phi\theta} & K_{\phi\phi} \end{bmatrix} = \mathbf{TKT}^T \tag{3.9}$$

$$= \begin{pmatrix} \cos\psi & 0 & \sin\psi \\ 0 & 1 & 0 \\ -\sin\psi & 0 & \cos\psi \end{pmatrix} \begin{pmatrix} K_{\parallel} & 0 & 0 \\ 0 & K_{\perp\theta} & K_A \\ 0 & -K_A & K_{\perp r} \end{pmatrix} \begin{pmatrix} \cos\psi & 0 & -\sin\psi \\ 0 & 1 & 0 \\ \sin\psi & 0 & \cos\psi \end{pmatrix} \tag{3.10}$$

$$= \begin{pmatrix} K_{\parallel}\cos^2\psi + K_{\perp r}\sin^2\psi & -K_A\sin\psi & \left(K_{\perp r} - K_{\parallel}\right)\cos\psi\sin\psi \\ K_A\sin\psi & K_{\perp\theta} & K_A\cos\psi \\ \left(K_{\perp r} - K_{\parallel}\right)\sin\psi\cos\psi & -K_A\cos\psi & K_{\perp r}\cos^2\psi + K_{\parallel}\sin^2\psi \end{pmatrix} \tag{3.11}$$

where the superscript T in Equation (3.9) denotes the transpose of the matrix. Evidently, the heliospheric transport of GCRs is determined by four basic coefficients, $K_{||}$, $K_{\perp r}$, $K_{\perp\theta}$ and K_A. They determine

$$K_{rr} = K_{||}\cos^2\psi + K_{\perp r}\sin^2\psi \tag{3.12}$$

which is the effective radial diffusion coefficient,

$$K_{\theta\theta} = K_{\perp\theta} \tag{3.13}$$

which is the effective polar diffusion coefficient,

$$K_{\phi\phi} = K_{\perp r}\cos^2\psi + K_{||}\sin^2\psi, \tag{3.14}$$

which is the effective azimuthal diffusion coefficient and

$$K_{\phi r} = (K_{\perp r} - K_{||})\sin\psi\cos\psi = K_{r\phi}, \tag{3.15}$$

which is the effective azimuthal-radial diffusion coefficient.

3.4.1. The parallel diffusion coefficient

In this section a brief overview of $K_{\parallel}$ is given without going into too much detail. It is responsible for transporting the GCRs parallel to the HMF. This basic transport mechanism is described by quasi-linear theory (QTL) (e.g. Jokipii 1966, 1971; Hasselmann and Wibberenz 1968, 1970; Dröge 2000), with the parallel mean free path $\lambda_{\parallel}$ given by

$$\lambda_{\|} = \frac{3\nu}{2}\int_0^1 \frac{\left(1-\mu^2\right)^2}{\Phi(\mu)}d\mu, \tag{3.16}$$

with ν the speed of particles, μ the cosine of the pitch angle and $\Phi(\mu)$ the Fokker Planck coefficient for pitch-angle scattering (see also Earl 1974; Stawicki 2003). The relationship between the parallel mean free path $(\lambda_{\|})$ and $K_{\|}$ is given by

$$\lambda_{\|} = \frac{3}{\nu}K_{\|}. \tag{3.17}$$

The calculation of $\Phi(\mu)$ in Equation (3.16) is needed as an input power spectrum of the magnetic field fluctuations which can be divided into three ranges namely; the energy range, where the power spectrum is independent of the wave number k, the inertial range where it is proportional to $k^{-5/3}$ and the dissipation range where it is proportional to k^{-3} (see e.g. Bieber et al. 1994). The dissipation range plays an important role in the resonant scattering of low energy particles where the pitch angles of these particles approach 90°. QLT predicts that $\lambda_{\|}$ becomes infinite if the dissipation range is included in the calculation of Equation (3.16). This is because $\Phi(\mu)$ goes to zero in the dissipation range as pitch angle approaches 90°.

In contrast, if the dissipation is neglected, $\lambda_{\|}$ becomes too small for lower rigidities and gives a wrong rigidity dependence, however, this small $\lambda_{\|}$ can be applied when calculating high energy proton modulation since protons experience large adiabatic energy changes below ~300 MeV and the change in $\lambda_{\|}$ will not have any effect on proton modulation (see e.g. Potgieter 1984).

Knowledge of $\lambda_{\|}$ is quite important for electron modulation because electrons with energies (rigidities) below ~300 MeV (300 MV) are diffusion dominated and respond directly to any changes in $\lambda_{\|}$ for rigidities $P < 100$ MV. A higher order theory, which is beyond the scope of this study, is needed to fully understand QLT.

Taking into account theoretical arguments by Burger et al. (2000), a $K_{\parallel}$ for computing GCRs electron modulation in the heliosphere was constructed by Ferreira (2002). This complex coefficient is given by

$$K_{\parallel} = K_0 \beta f_1(r,P), \tag{3.18}$$

where

$$f_1(r,P) = 0.2 g(P) c(r) h(r,P), \tag{3.19}$$

with

$$h(r,P) = 0.02\left(\frac{P}{P_0}\right)^2\left(\frac{r}{r_0}\right)^{1.7} + 0.02\left(\frac{P}{P_0}\right)\left(\frac{r}{r_0}\right)^{2.2} + 0.2\left(\frac{P}{P_0}\right)^{1/3}\left(\frac{r}{r_0}\right) + 7.0e(r), \tag{3.20}$$

$$c(r) = \begin{Bmatrix} 1.0 \text{ if } r > r_c \\ m(r) \text{ if } r \le r_c \end{Bmatrix}, \tag{3.21}$$

$$m(r) = \frac{r_0}{r_c}\xi\left(\frac{r}{r_0}\right)^{\xi}, \tag{3.22}$$

and

$$g(P) = \left(\frac{P_0}{P_s}\right)^{0.6}, \tag{3.23}$$

$$\text{where} \quad \xi = \left(\frac{r}{r_c}\right)^{x},\ x = \left(\frac{0.016}{P/P_0}\right)^{0.2},\ r_c = \frac{r_0}{0.1 + \left(P_s/P_0\right)^{1.4}}, \tag{3.24}$$

and

$$e(r) = \begin{Bmatrix} \left(10 r_0 / r\right)^k \text{ if } r > 10 \text{ AU} \\ 1.0 \text{ if } r \le 10 \text{ AU} \end{Bmatrix}, \tag{3.25}$$

with $k = 125\times10^{-4}\left(r/r_0\right)^2$. Here β is the ratio of the speed of cosmic ray particles to the speed of light, $K_0 = 4.5\times10^{22}$ cm^{2}s^{-1}, $P_0 = 1$ GV, $r_0 = 1$ AU and $P_s = P$ when $P < 1$ GV and $P_s = 1$ GV when $P \ge 1$ GV.

Ndiitwani (2005) constructed a different $\lambda_{\parallel}$, especially in terms of its rigidity dependence, based on the theoretical turbulence work done for $\lambda_{\parallel}$ at Earth by Teufel and Schlickeiser

(2002). In addition, a radial dependence was constructed in order to have a $\lambda_{\parallel}$ which produces realistic modulation in the heliosphere. This parallel mean free path is given by

$$\lambda_{\parallel} = \lambda_1(r,P)\,\lambda_2(r,P), \tag{3.26}$$

where

$$\lambda_1(r,P) = \frac{5}{3}\left(0.0106\left(\left(P/P_0\right)^{1/3} + \frac{3.57}{\left(0.511^2 + \left(P/P_0\right)^2\right)^{1/4}}\right) + (r/r_0)^{1.4}\times 10^{-9}\left(P/P_0\right)^2\right), \tag{3.27}$$

and

$$\lambda_2(r,P) = \frac{c_1(P) + 0.08}{c_1(P)(r/r_0)^{-2.30} + 0.08(r/r_0)^{0.37}}, \tag{3.28}$$

with

$$c_1(P) = 83.0\left(\frac{0.02}{1000P}\right)^{0.75}. \tag{3.29}$$

The parallel diffusion coefficient is then

$$K_{\parallel} = \frac{v}{3}\lambda_{\parallel}(r,P). \tag{3.30}$$

This implies that $\lambda_{\parallel}$ for low energy GCRs electrons has almost no rigidity dependence which is required as will be illustrated in the following chapters.

This mean free path was also used by Nkosi et al. (2008) and Nkosi (2006) to compute modulation for electrons and will be discussed in sections 3.5 to 3.7, in terms of its rigidity dependence, radial and latitudinal dependence. The chapter ends with a discussion of the diffusion coefficients for the purpose of this study and a motivation why they are necessary.

3.4.2. The perpendicular diffusion coefficient

In general $K_{\perp}$ plays a very important role in the transport of GCRs particles in the direction perpendicular to the HMF. It is subdivided into two coefficients, perpendicular to the HMF in the radial direction given by $K_{\perp r}$ and perpendicular to the HMF in the polar direction, given by $K_{\perp\theta}$. It has become a standard practice to scale $K_{\perp}$ spatially as $K_{||}$. It then follows that

$$K_{\perp r} = aK_{||} \tag{3.31}$$

and

$$K_{\perp\theta} = bK_{||} \tag{3.32}$$

where a and b are either constants or if required, a function of rigidity (see also Ferreira 2002; Nkosi 2006 and Ngobeni 2006).

In this work, as done by Ferreira (2002) and Nkosi (2006), it is assumed that

$$K_{\perp\theta} = bK_{||}F(\theta), \tag{3.33}$$

with

$$F(\theta) = A^{+} \pm A^{-} \tanh\left[\frac{1}{\Delta\theta}\left(\theta_A - 90^0 + \theta_F\right)\right], \tag{3.34}$$

where $A^{\pm}=1/2(d\pm1)$, $\Delta\theta = 1/8$, $\theta_A = \theta$ and $\theta_F = 35°$ for $\theta \leq 90°$ while for $\theta > 90°$, $\theta_A = 180°-\theta$ and $\theta_F = -35°$. This means that $K_{\theta\theta} = K_{\perp\theta}$ is enhanced toward the poles by a factor d with respect to the value of $K_{||}$ in the equatorial region as is required to explain Ulysses observations (see Potgieter 1996, 2000; Ferreira et al. 2001a; Heber and Potgieter 2006). This function is illustrated in Figure 3.1 with $d = 6$.

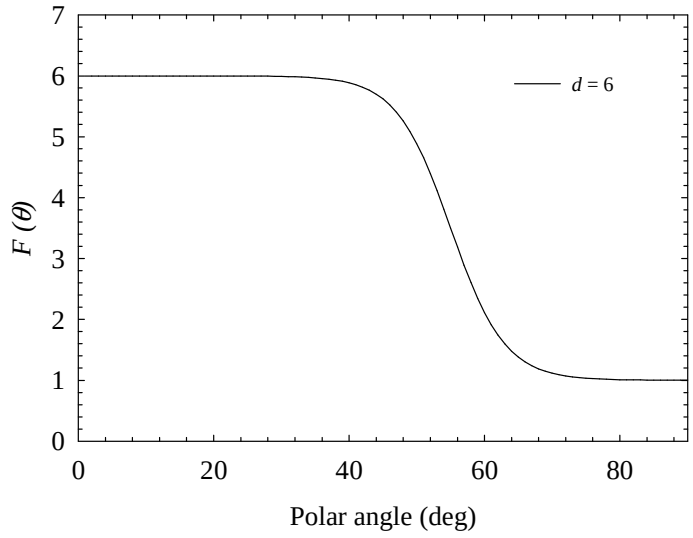

Figure 3.1: $F(\theta)$ in Equation (3.34) as a function of polar angle, for d = 6.

The rigidity dependence, radial and latitudinal dependence of the diffusion coefficients are discussed in the next sections.

3.5. The drift coefficient

The drift coefficient under the assumption of weak scattering is given by

$$(K_A)_{standard} = (K_A)_0 \frac{\beta P}{3B_m}, \tag{3.35}$$

Here, the constant $(K_A)_0$ is dimensionless and varies between 1.0 and 0.0 which describes what Potgieter et al. (1989) called 100% and 0% drifts. The drift coefficient used by Burger et al. (2000) and Ferreira (2002) is different from this standard weak scattering form and is given by

$$K_A = (K_A)_0 \frac{\beta P}{3B_m} K_{drift}(P), \tag{3.36}$$

with B_m being the modified HMF given by Equation (2.8) and $K_{drift}(P)$ given by

$$K_{drift}(P) = \frac{10P^2}{1+10P^2}, \tag{3.37}$$

with $(K_A)_0 = 1.0$. Equation (3.36) means that the drift coefficient is scaling with a spatial dependence of $1/B_m$ and that its rigidity dependence is increased at lower energies to account for observations e.g. Webber (1990) and Heber and Potgieter (2006). This rigidity dependence is shown and discussed below.

3.6. Rigidity dependence of the drift and diffusion coefficients

In any 3D modulation model, the diffusion tensor has nine elements as given by Equations (3.9) to (3.11). As shown above, a spatial dependence needs to be assigned to them, usually based on diffusion and turbulence theory (e.g. Burger et al. 2000). These theoretically based diffusion coefficients (DCs) are usually improved phenomenologically using comparisons between numerical models and observations. The rigidity dependence of these coefficients is equally important and the same procedure is followed. In this section, the rigidity dependence and in the next section the spatial dependence of the DCs used by Nkosi (2006) and Ndiitwani (2005) as given above are reviewed and graphically illustrated, followed by the simplified DCs used for the purpose of this study.

The work of Nkosi (2006) was focused on Jovian electrons in the inner heliosphere, without attempting to explain Voyager observations of GCR electrons in the outer heliosphere. The work of Ndiitwani et al. (2005) was focused on GCR protons along the Voyager trajectories and could reproduce observations in the outer heliosphere. (See also Manuel et al. 2011). The issue investigated here is whether the rather complex rigidity and spatial dependence as shown above are indeed also required for GCR electrons from the inner to the outer heliosphere. It will be illustrated that simplified DCs are adequate to obtain compatibility with Voyager 1 observations in the outer heliosphere while retaining compatibility with the observations at Earth.

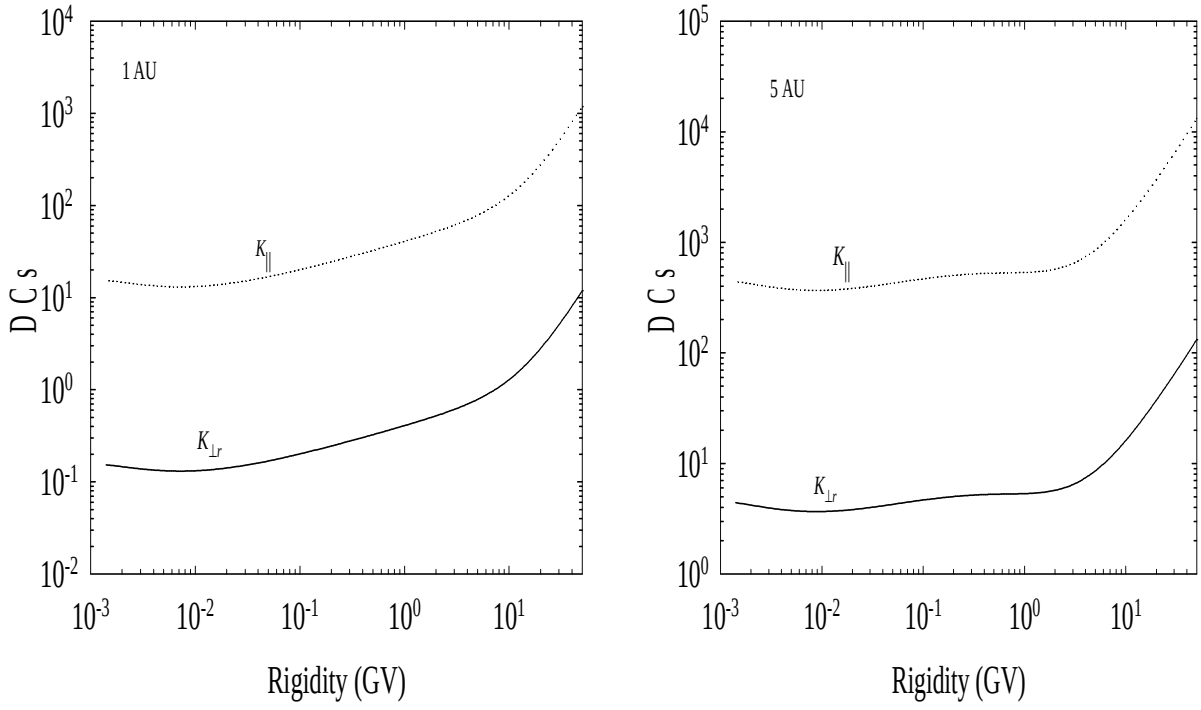

Figure 3.2: Computed rigidity dependence of $K_{||}$ and $K_{\perp r}$ for 12 MeV electrons at 1 AU and 5 AU, respectively, with θ = 60°. The DCs are in units of 6×10^{20} cm^2 s^{-1} in all the figures.

Left panel of Figure 3.2 shows the computed rigidity dependence of $K_{||}$ (dotted line) and $K_{\perp r}$ (solid line) of Ndiitwani (2005) at 1 AU with θ = 60°. At 1 AU, both are almost constant at low rigidity but increase rapidly for $P > 0.1$ GV. The right panel shows the rigidity dependence of $K_{||}$ and $K_{\perp r}$ at 5 AU. In this case both remain almost constant up to $P \simeq 2$ GV, increasing rapidly with higher rigidities. Evidently, $K_{||}$ and $K_{\perp r}$ have the same rigidity dependence but have different values (as in Equation 3.31). The rigidity dependence for larger radial distances looks similar and is thus not shown.

Figure 3.3 shows the computed rigidity dependence of K_{rr}, $K_{\phi\phi}$ and $K_{\theta\theta}$ (top panels) and $-\left(K_{r\phi} = K_{\phi r}\right)$ (bottom panels) for 12 MeV electrons at 1 AU and 5 AU respectively, with θ = 60°, representing the Voyager 1 trajectory. Evidently, they have the same rigidity dependence, changing with radial distance with a strong increasing trend as P increases. At 1 AU, K_{rr} has the largest value but at 5 AU, $K_{\phi\phi}$ is dominating. The bottom panels show the

rigidity dependence of $-(K_{r\phi} = K_{\phi r})$ for 1 AU and 5 AU. At 1 AU for small rigidities i.e. below $P > 0.1$ GV , $-(K_{r\phi} = K_{\phi r})$ is small and almost a constant, but at $P = 0.1$ GV it starts to increase sharply with higher rigidities. At 5 AU, $-(K_{r\phi} = K_{\phi r})$ remains almost constant for P< 4 GV, increasing sharply above this value. The rigidity dependence is thus much stronger at 1 AU for $-\left(K_{r\phi} = K_{\phi r}\right)$ than at 5 AU.

Figure 3.4 shows the rigidity dependence of $K_{\theta\phi}$ and $K_{\theta r}$ (top panels) and $-K_{\phi\theta}$ and $-K_{r\theta}$ (bottom panels) at 1 AU and 5 AU, respectively. This represents the drift term in the diffusion tensor as shown in Equations (3.36) and (3.37). The rigidity dependence for $K_{\theta\phi}$, $K_{\theta r}$, $-K_{\phi\theta}$ and $-K_{r\theta}$ is indistinguishable at 1 AU but this is not the case at 5 AU; $K_{\theta r} > K_{\theta\phi}$ and $-K_{\phi\theta} > -K_{r\theta}$. The stronger decrease in the rigidity dependence below $P \simeq 0.1$ GV is because of the scaling factor in Equation (3.37). The implication of this is that for low energy electrons drifts become negligible so that the transportation of these particles is dominated by diffusion.

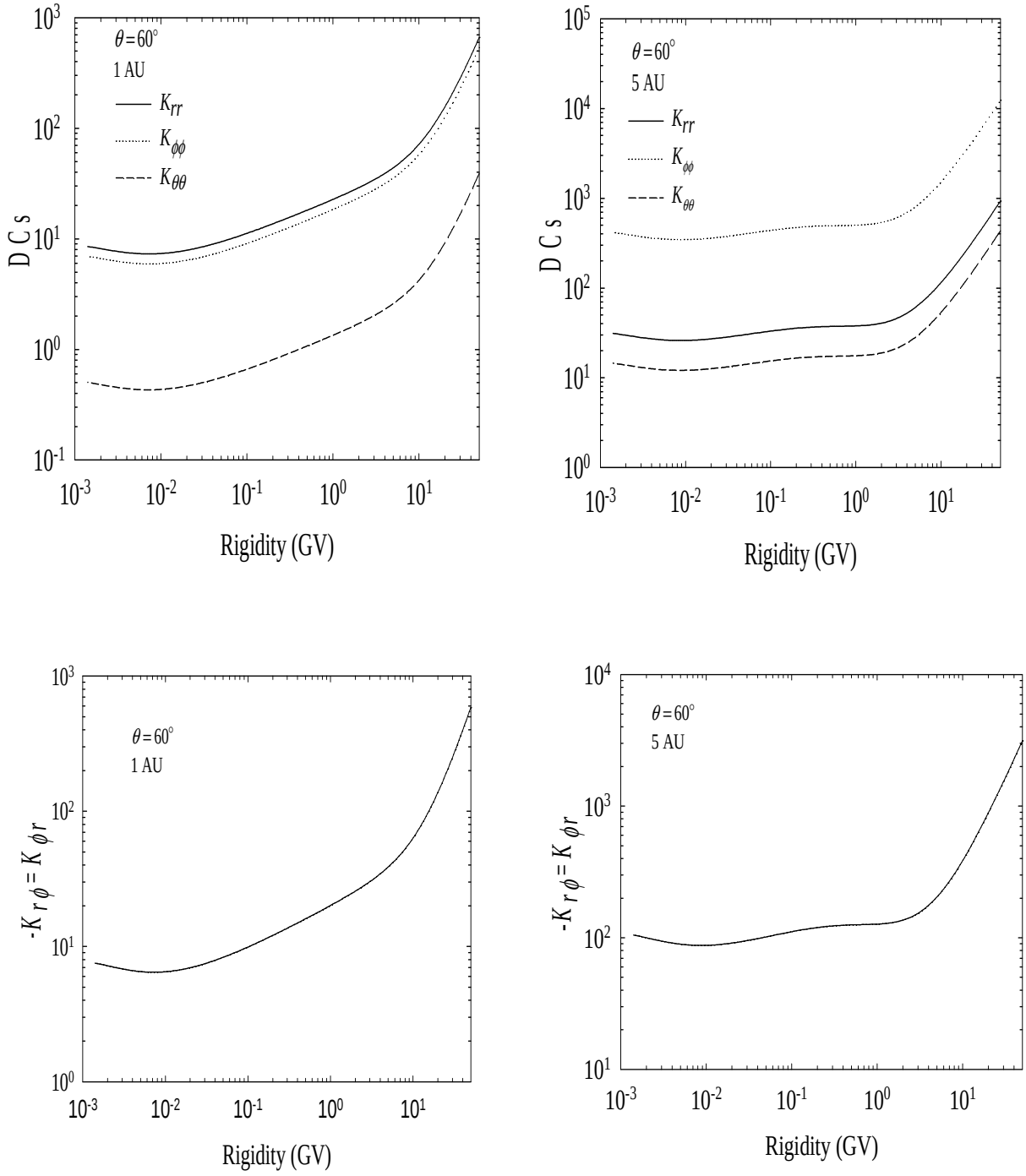

Figure 3.3: Computed rigidity dependence of DCs with θ = 60° at 1 AU and 5 AU respectively. Top panels show the rigidity dependence of K_{rr}, $K_{\phi\phi}$ and $K_{\theta\theta}$; bottom panels show the rigidity dependence for $-(K_{r\phi} = K_{\phi r})$.

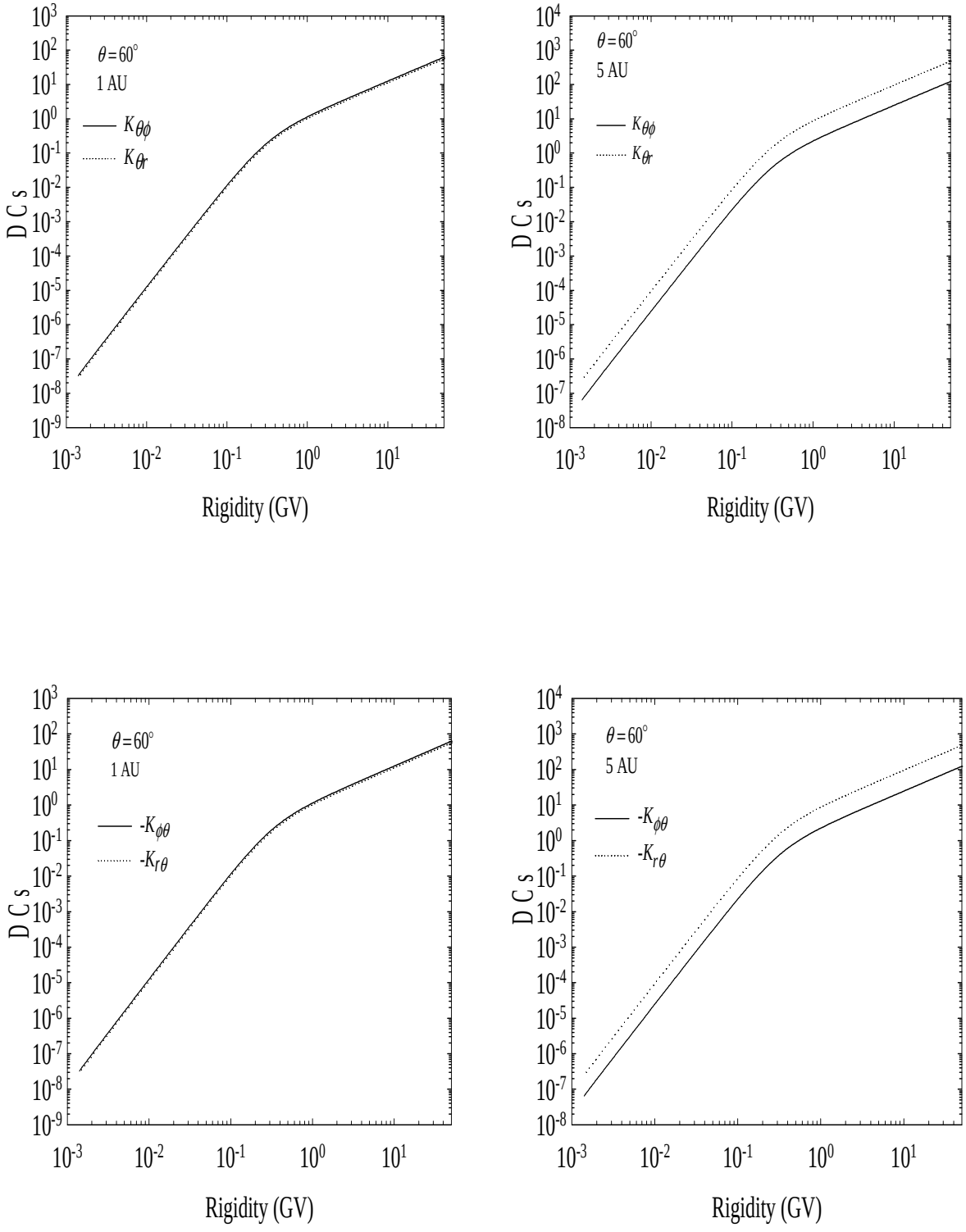

Figure 3.4: Computed rigidity dependence of $K_{\theta\phi}$ and $K_{\theta r}$ (top panels); bottom panels show the rigidity dependence of $-K_{\phi\theta}$ and $-K_{r\theta}$, again at 1 AU and 5 AU, with θ = 60°.

3.7. Radial dependence

The top panel of Figure 3.5 shows the radial dependence of $K_{||}$ and $K_{\perp r}$ for 12 MeV electrons computed with θ = 60° which is the latitude of Voyager 1. Based on the assumptions made as discussed above $K_{||} > K_{\perp r}$, throughout the heliosphere, with both increasing from 1 AU to 10 AU then to remain almost constant. The bottom panel of Figure 3.5 shows the radial dependence of K_{rr}, $K_{\phi\phi}$ and $K_{\theta\theta}$ computed with θ = 60°. According to Equation (3.12), K_{rr} is dominated by $K_{||}$ in the inner heliosphere whereas $K_{\perp r}$ dominates in the outer heliosphere (except at and near the poles) but according to Equation (3.14) it is the other way around for $K_{\phi\phi}$; the reason why these two diffusion coefficients have a different radial dependence. Essentially, this is determined by the combination of $K_{||}$, and $K_{\perp r}$ and the geometry of the assumed HMF (the terms depending on the spiral angle). Note that $K_{\theta\theta} = K_{\perp\theta}$ which increases rapidly within the first 10 AU, to remain then almost constant.

The top panel of Figure 3.6 shows the radial dependence of $-\left(K_{r\phi} = K_{\phi r}\right)$ at 12 MeV again computed with θ = 60°. Within the first 10 AU in the inner heliosphere $-\left(K_{r\phi} = K_{\phi r}\right)$ increases to turn round and decreases sharply with increasing radial distances. The middle panel shows the radial dependence of $K_{\theta\phi}$ and $K_{\theta r}$; $K_{\theta\phi}$ is independent of radial distance for most of the heliosphere, but this is not the case with $K_{\theta r}$, see Equation (3.11). The bottom panel shows the radial dependence of $-K_{\phi\theta}$ and $-K_{r\theta}$, which is identical to the middle panel.

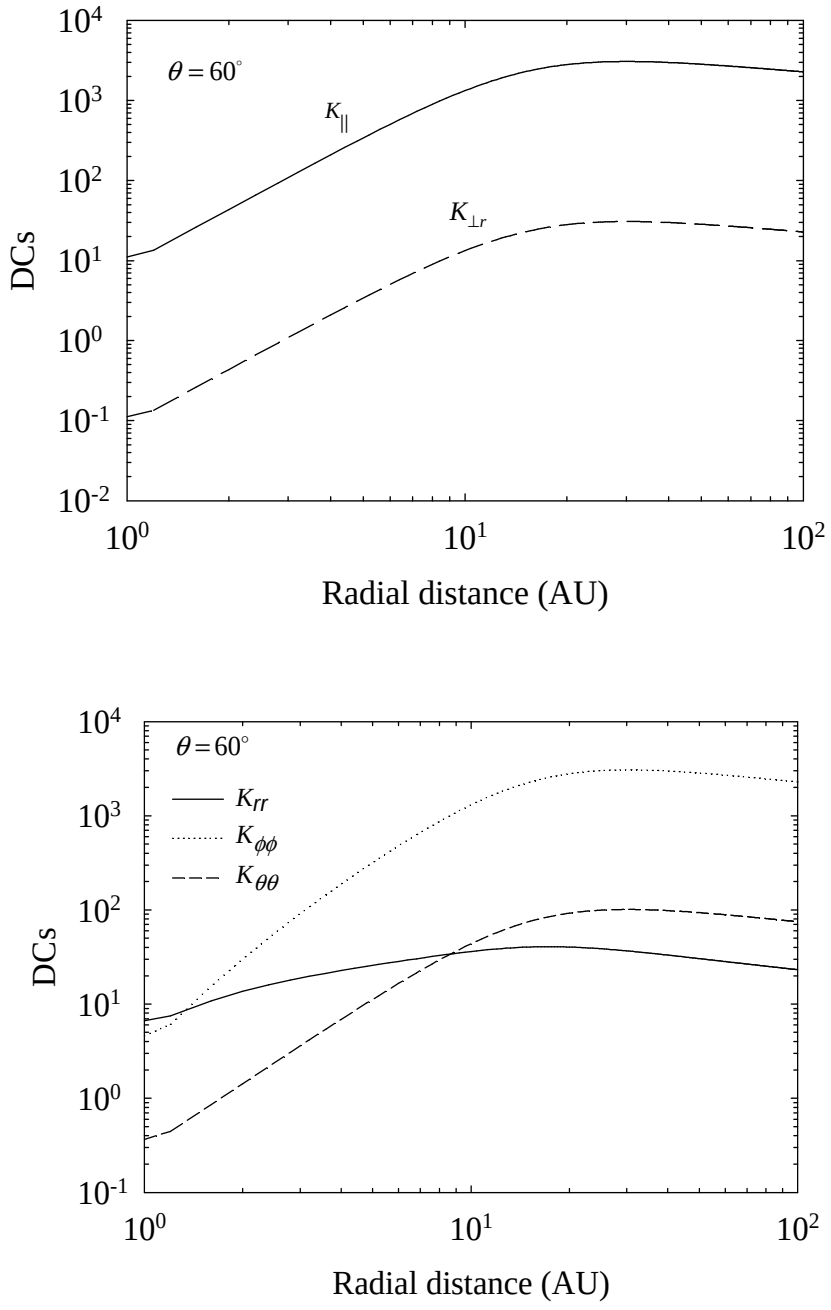

Figure 3.5: Computed radial dependence of $K_{||}$ and $K_{\perp r}$ (top panel) and $K_{rr}, K_{\theta\theta}$ and $K_{\phi\phi}$ (bottom panel) with θ = 60° and at an energy of 12 MeV.

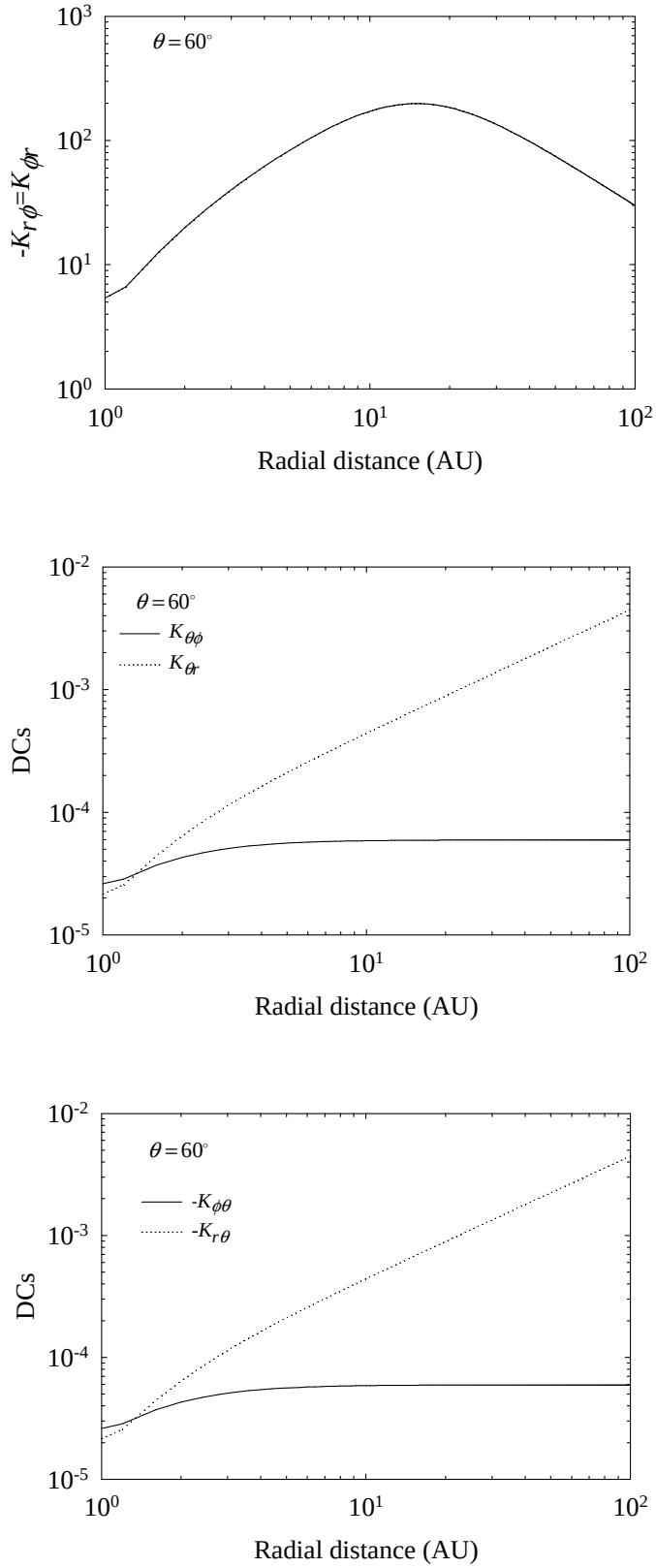

Figure 3.6: Computed radial dependence for 12 MeV electrons of $-\left(K_{r\phi} = K_{\phi r}\right)$ (top panel), $K_{\theta\phi}$ and $K_{\theta r}$ (middle panel) and $-K_{\phi\theta}$ and $-K_{r\theta}$ (bottom panel), with $\theta = 60^{\circ}$.

3.8. Latitudinal dependence

Top panel of Figure 3.7 shows the computed polar (latitudinal) dependence of K_{rr} at 1 AU and 5 AU for 12 MeV electrons; K_{rr} is larger at the poles than at the equatorial plane because it is dominated by $K_{\parallel}$ at the poles. Evidently, K_{rr} increases with increasing radial distance, more so at the poles than at the equatorial plane. The bottom panel shows the polar dependence of $K_{\phi\phi}$, see Equation (3.14). At 1 AU, it decreases strongly close to the poles but remaining otherwise almost constant.

Top panel of Figure 3.8 shows the computed polar dependence of $K_{\theta\theta}$ at 1 AU and 5 AU, respectively. $K_{\theta\theta}$ is small in the equatorial plane and increases significantly between ~70° and ~50° to a constant value up to 0°. The reason for this is the effect of using Equation (3.34) and illustrates the enhancement of $K_{\theta\theta}$ towards the heliospheric poles. The bottom panel shows the polar dependence of $-(K_{r\phi} = K_{\phi r})$, see Equation (3.15). The values drop sharply towards the poles but remain constant close to the equatorial plane.

Figure 3.9 shows the computed polar dependence of $K_{\theta\phi}$ (top left panel) and $K_{\theta r}$ (top right panel) at 1 AU and 5 AU for 12 MeV electrons. The values are quite small at this energy (see also Figure 3.4). These DCs are determined by the drift coefficient K_A according to Equation (3.11) and since it is small at these energies, they obviously contribute little to drift effects. The bottom panels of Figure 3.9 show the latitudinal dependence of $-K_{\phi\theta}$ and $-K_{r\theta}$. The results are similar to what was obtained in the top panels, as it should be. According to Equation (3.11), $K_{\theta\phi} = K_{\phi\theta}$ and $K_{\theta r} = K_{r\theta}$; they differ only in sign.

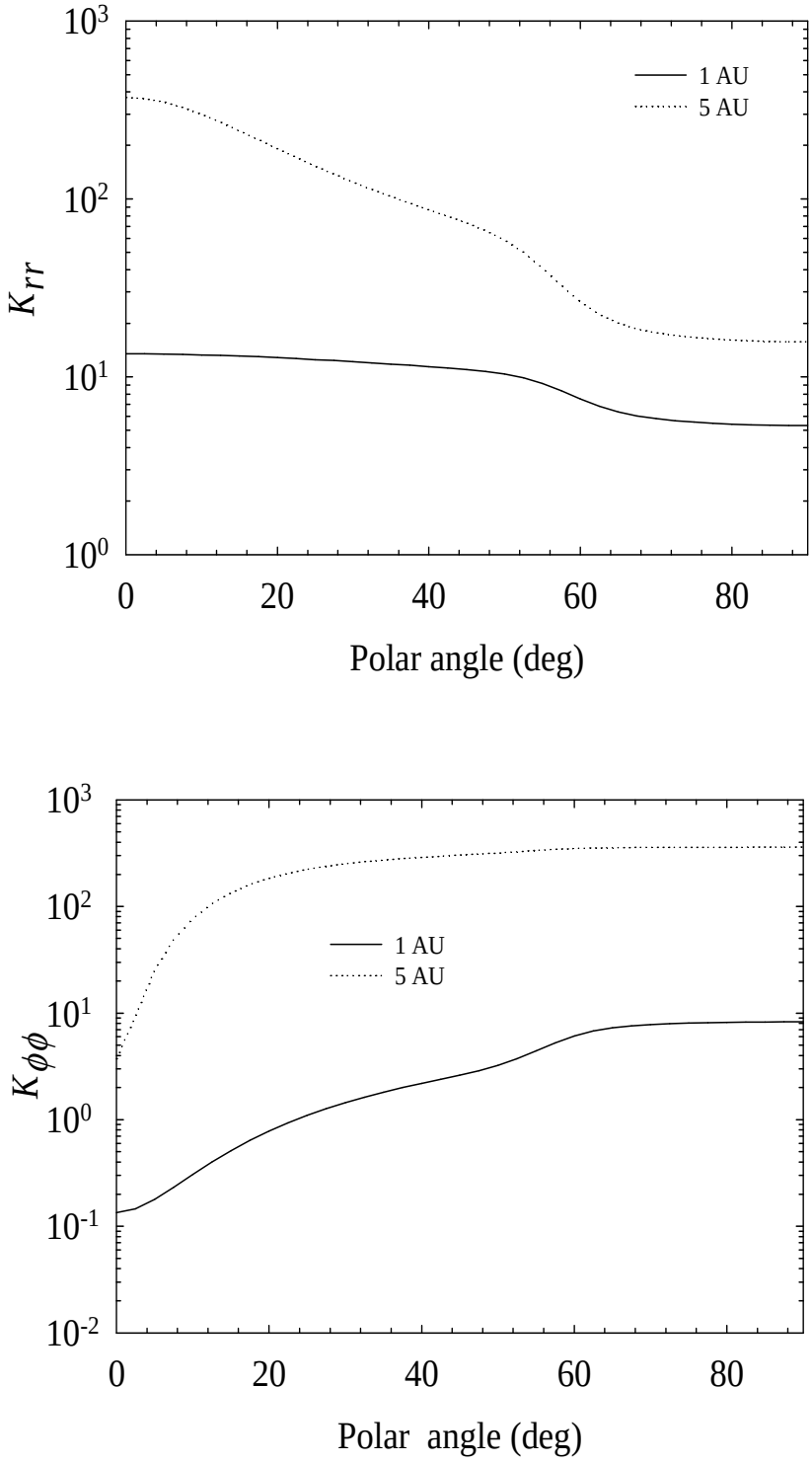

Figure 3.7: DCs K_{rr} and $K_{\phi\phi}$ as a function of polar angle at 1 AU and 5 AU for 12 MeV electrons.

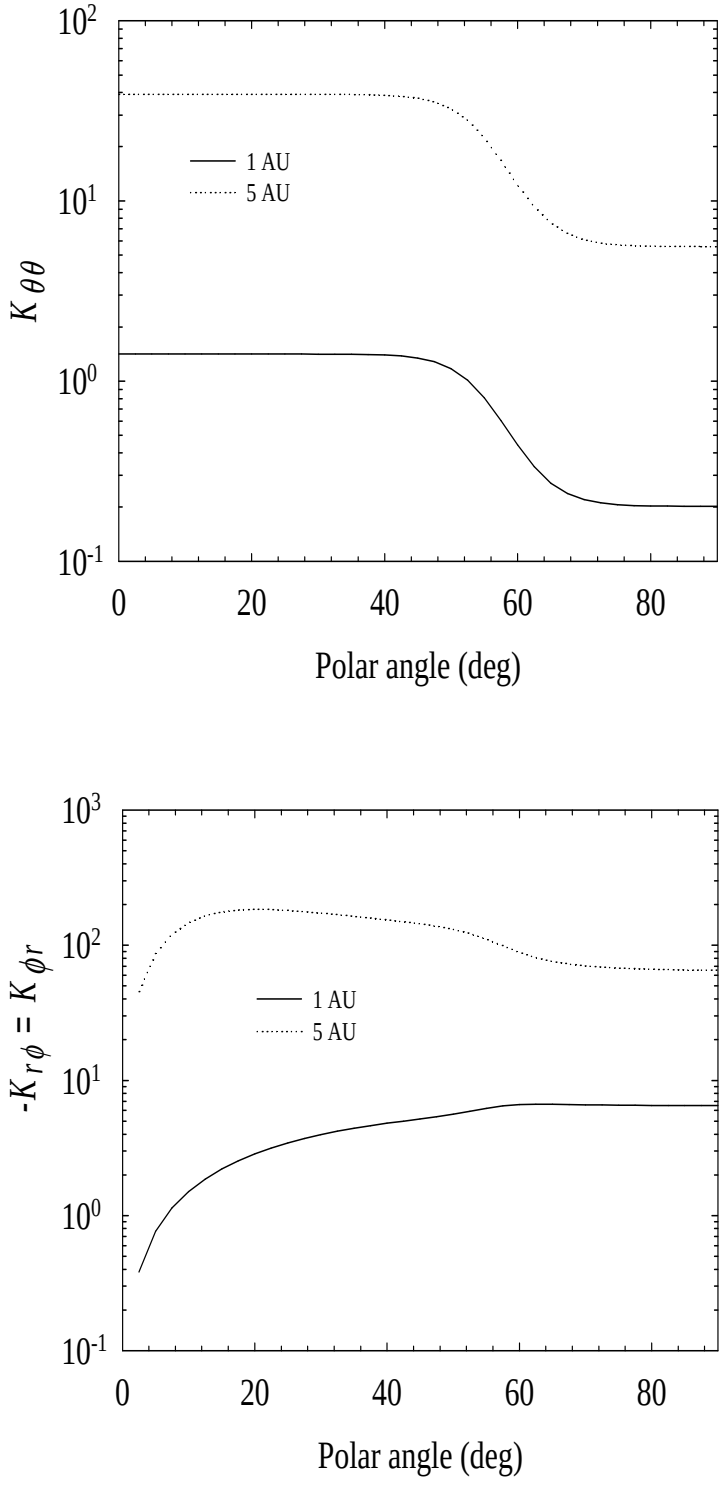

Figure 3.8: DCs $K_{\theta\theta}$ (top panel) and $-(K_{r\phi} = K_{\phi r})$ (bottom panel) as a function of polar angle at 1 AU and 5 AU for the 12 MeV electrons.

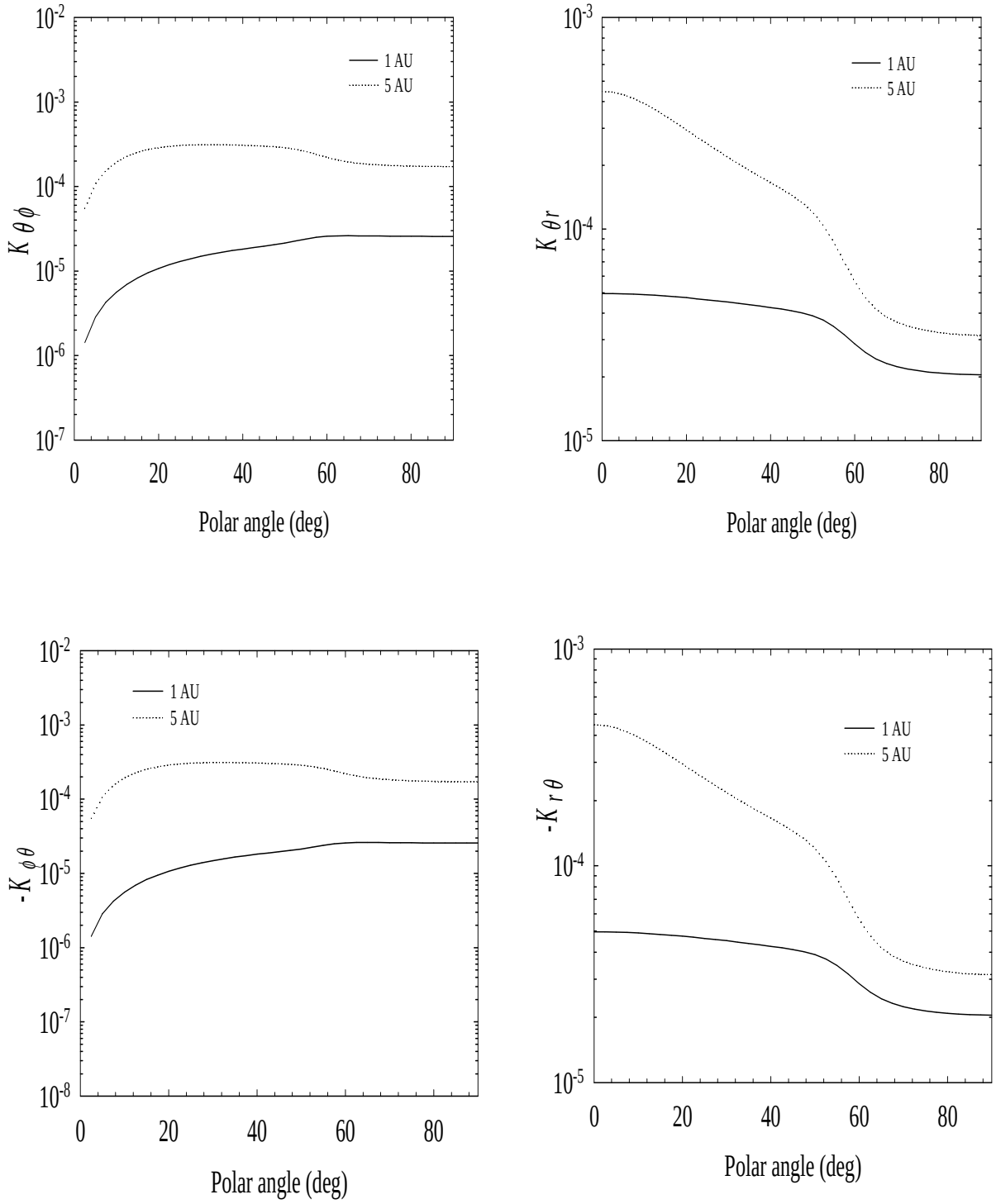

Figure 3.9: Latitudinal dependence of $K_{\theta\phi} = -K_{\phi\theta}$ and $K_{\theta r} = -K_{r\theta}$ at 1 AU and 5 AU for 12 MeV electrons. See also Equation (3.11).

3.9. Diffusion and drift coefficients for the purpose of this study

The DCs illustrated above do not reproduce all aspects of observed GCR electrons in the heliosphere, despite being rather complex, to the extent that it becomes rather tedious to keep the numerical ADI solving procedure stable (e.g. Hattingh 1998). It has become necessary to re-evaluate these complex DCs and compare the solutions they produce with simpler approaches which appear to be at least as good as these complex equations. This will be investigated in this and in the following chapters.

To compute electron modulation in the heliosheath, a simpler approach is to assume: $K_{||} = K_0 \beta f_1(P) f_2(r,\theta)$ with $f_1(P)$ giving the rigidity dependence and $f_2(r,\theta)$ the spatial dependence of $K_{||}$. This approach, which separates the rigidity dependence from the spatial dependence, will be used to compute the modulation of 12 MeV electrons. Following Potgieter and Ferreira (1999), the assumptions made in Equations (3.31) to (3.34) are used. It will be illustrated that such a simplified approach is adequate to obtain compatibility with Voyager 1 observations in the outer heliosphere. In order to be able to achieve this compatibility, a constant rigidity dependence below P < 0.4 GV is needed, but changing significantly when $P > 0.4$ GV. A similar approach was used by Potgieter (1984).

3.9.1. Parallel and perpendicular diffusion coefficients

The diffusion coefficients used for this study have a different radial dependence in the inner heliosphere than in the outer heliosphere. In order to assure compatibility with Voyager 1 electron observations, it is necessary to specify the DCs differently over the first 80 AU than in the outer heliosphere with $r > 80$ AU. This will be discussed further in later chapters.

In the inner heliosphere ($r < 80$ AU), the DCs are given as follows.

If $P <$ 0.4 GV:

$$K_{||} = (K_0 / 5.0)\ \beta\left(1+\left(\frac{r}{r_e}\right)^{1.2}\right), \tag{3.38}$$

$$K_{\perp r} = (a / 5.0)K_{||}. \tag{3.39}$$

If $P \geq 0.4$ GV:

$$K_{||} = (K_0 / 5.0)\beta\left(\frac{P}{P_0}\right)\left(1+\left(\frac{r}{r_e}\right)^{1.2}\right), \tag{3.40}$$

$$K_{\perp r} = (a / 5.0)K_{||}. \tag{3.41}$$

In the outer heliosphere, r > 80 AU, the coefficients become:

If $P < 0.4$ GV:

$$K_{||} = (K_0 / 5.0)\ \beta\left(1+(r / r_e)^{0.6}\right), \tag{3.42}$$

$$K_{\perp r} = (a / 5.0)K_{||}. \tag{3.43}$$

If $P \geq 0.4$ GV:

$$K_{||} = (K_0 / 5.0)\ \beta(\frac{P}{P_0})\left(1+(r / r_e)^{0.6}\right), \tag{3.44}$$

$$K_{\perp r} = (a / 5.0)K_{||}. \tag{3.45}$$

For the perpendicular diffusion in the polar direction:

$$K_{\perp\theta} = aK_{||}F\left(\theta\right), \tag{3.46}$$

with

$$F(\theta) = A^{+} \pm A^{-} \tanh\left[\frac{1}{\Delta\theta}\left(\theta_A - 90^0 + \theta_F\right)\right], \tag{3.47}$$

where $A^{\pm}$*=1/2(d±1),* $\Delta\theta$ *=1/8,* $\theta_A = \theta$ and $\theta = 35°$ for $\theta \leq$ 90° while for $\theta >$ 90°, $\theta_A = 180° - \theta$ and $\theta_F = -35°$.

In these equations, $a = 0.025$ and $K_0 = 76$ in units of $6.0\times10^{20}\,\mathrm{cm^2 s^{-1}}$, r_e = 1 AU and P_0 = 0.4 GV.

3.9.1.1. Rigidity dependence

In this section, the rigidity dependence given in Equations (3.36) and (3.38) to (3.47) is illustrated.

Shown in the top panel of Figure 3.10 is the computed rigidity dependence of $K_{||}$ at 1 AU, 5 AU, 60 AU, 90 AU and 110 AU with θ = 60°. Evidently, it is constant below P < 0.4 GV, increasing proportional to P above 0.4 GV. The choice of using this straight forward rigidity dependence is based on turbulence theory as developed for the innermost heliosphere (Burger et al. 2000), assuming to be applicable also to the outer heliosphere. The illustrated rigidity dependence reflects what is assumed for Equations (3.38) to (3.45). The bottom panel shows the computed rigidity dependence of $K_{\perp r}$ also at 1 AU, 5 AU, 60 AU, 90 AU and 110 AU. As expected, it is identical to that for $K_{||}$ but with $K_{\perp r} < K_{||}$.

Top panels of Figure 3.11 show the computed rigidity dependence of K_{rr}, $K_{\phi\phi}$ and $K_{\theta\theta}$ at 1 AU and 5 AU, respectively, with θ = 60°. These DCs have the same rigidity dependence as $K_{||}$ and $K_{\perp r}$. At 1 AU, K_{rr} has the largest value followed by $K_{\phi\phi}$ and $K_{\theta\theta}$ respectively, but at 5 AU, $K_{\phi\phi}$ has the largest value because it is dominated by other terms. The bottom panels show the rigidity dependence of $-\left(K_{r\phi} = K_{\phi r}\right)$ at 1 AU and 5 AU respectively. Evidently, $\left|K_{r\phi} = K_{\phi r}\right|$ is larger at 5 AU than at 1 AU.

Top panels and bottom panels of Figure 3.12 show the computed rigidity dependence of $K_{\theta\phi}$ and $K_{\theta r}$ and $-K_{\phi\theta}$ and $-K_{r\theta}$, respectively, at 1 AU and 5 AU with θ = 60°. As mentioned before, this is determined by the rigidity dependence of the drift coefficient given in Equations (3.36) and (3.37) with a stronger dependence at lower rigidity than at higher rigidity.

In Figure 3.13 the rigidity dependence of K_{rr}, $K_{\phi\phi}$ and $K_{\theta\theta}$ (top panels), together with $-\left(K_{r\phi} = K_{\phi r}\right)$(bottom panels) is displayed, now at 60 AU and 90 AU. As expected, they have the same rigidity dependence but with different values at these radial distances.

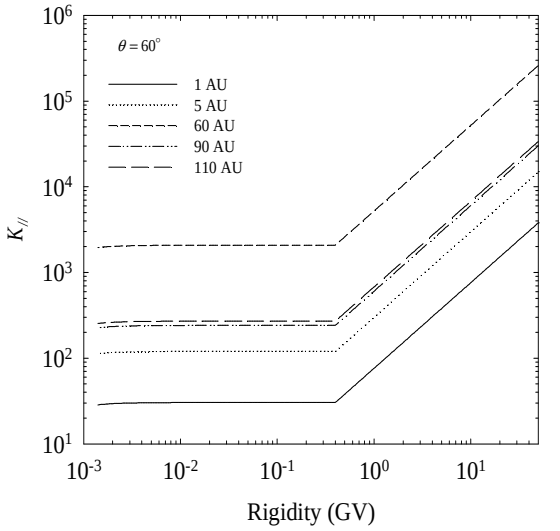

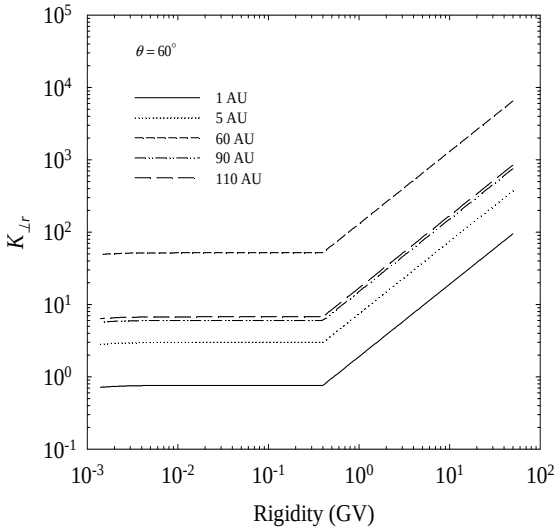

Figure 3.10: Computed rigidity dependence of $K_{||}$ and $K_{\perp r}$ at 1 AU, 5 AU, 60 AU, 90 AU and 110 AU, with θ = 60°. The DCs are in units of 6×10^{20} cm^2 s^{-1} in all figures.

Figure 3.14 shows the rigidity dependence of $K_{\theta\phi}$ and $K_{\theta r}$ (top panels) and $-K_{\phi\theta}$ and $-K_{r\theta}$ (bottom panels) at 60 AU and 90 AU. Similar to Figure 3.12 they have the same rigidity dependence.

Figure 3.15 shows the computed rigidity dependence now at 110 AU for K_{rr}, $K_{\phi\phi}$ and $K_{\theta\theta}$ (top left), for $-\left(K_{r\phi}=K_{\phi r}\right)$ (top right), for $K_{\theta\phi}$ and $K_{\theta r}$ (bottom left) and for $-K_{\phi\theta}$ and $-K_{r\theta}$ (bottom right). As expected, all these DCs have the same rigidity dependence but with different absolute values.

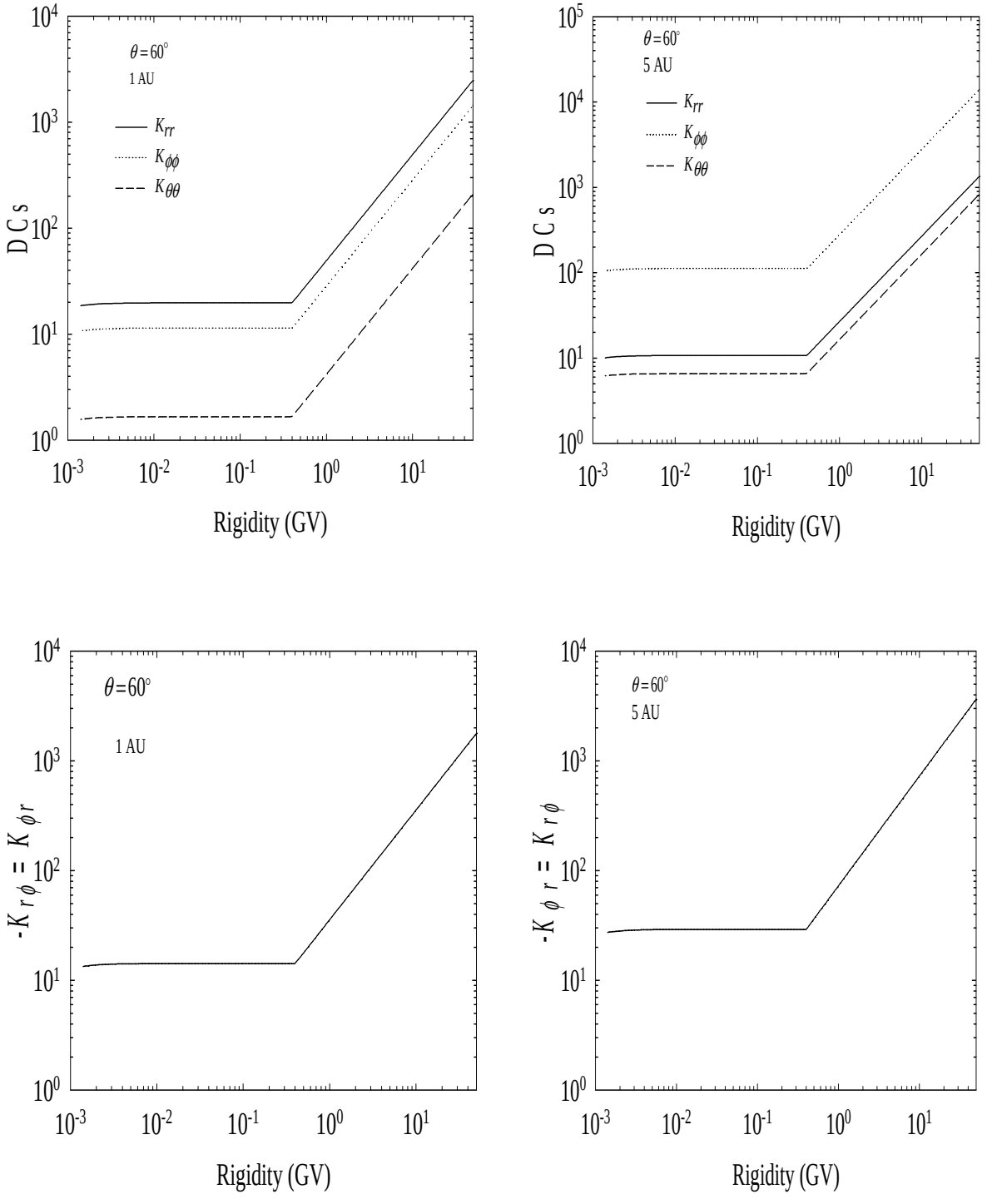

Figure 3.11: Computed rigidity dependence of $K_{rr}, K_{\phi\phi}$ and $K_{\theta\theta}$ (top panels) and $-(K_{r\phi} = K_{\phi r})$ (bottom panels) at 1 AU and 5 AU, with θ = 60°.

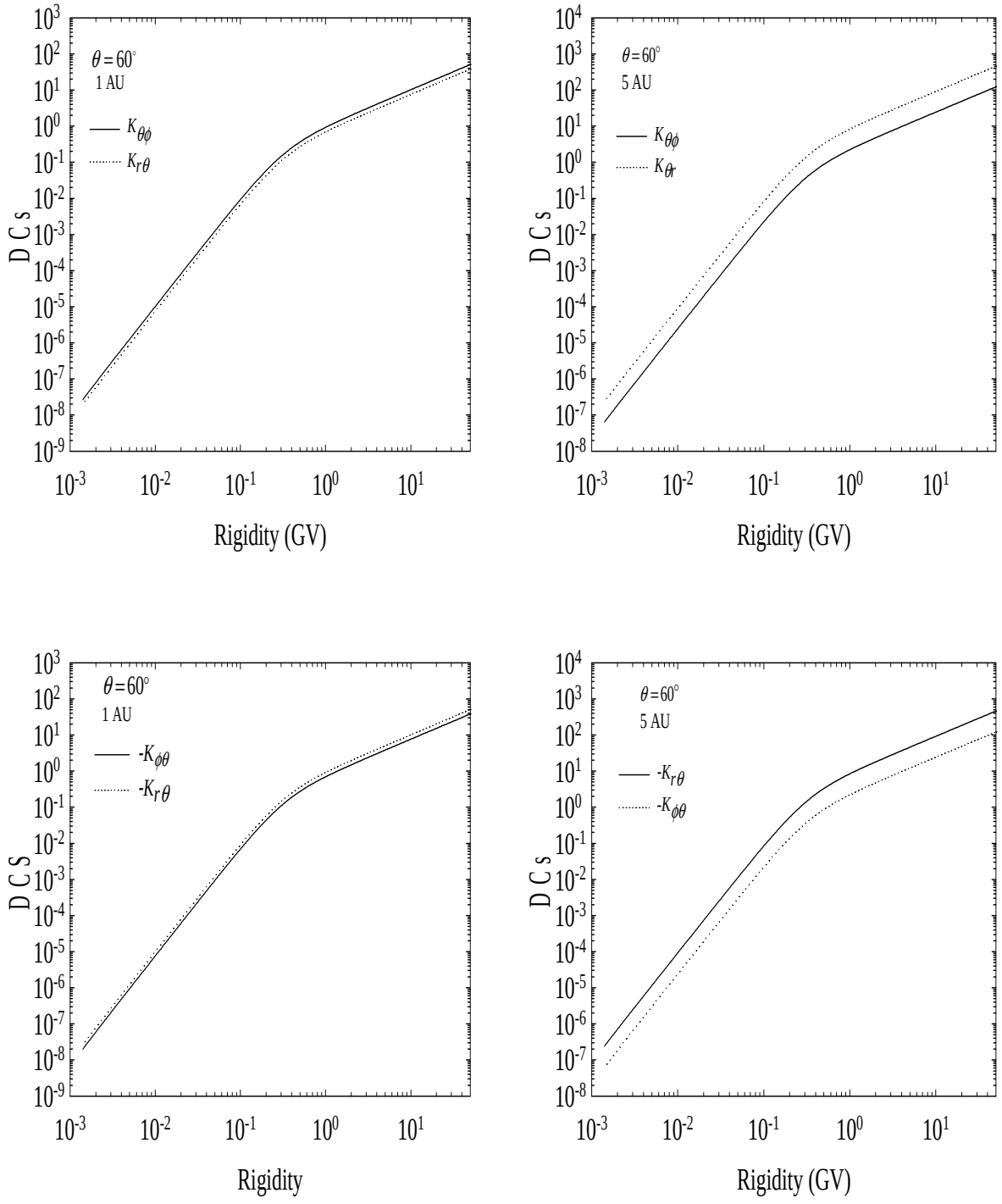

Figure 3.12: Computed rigidity dependence of $K_{\theta\phi}$ and $K_{\theta r}$ (top panels) and $-K_{\phi\theta}$ and $-K_{r\theta}$ (bottom panels) at 1 AU and 5 AU, with θ = 60°.

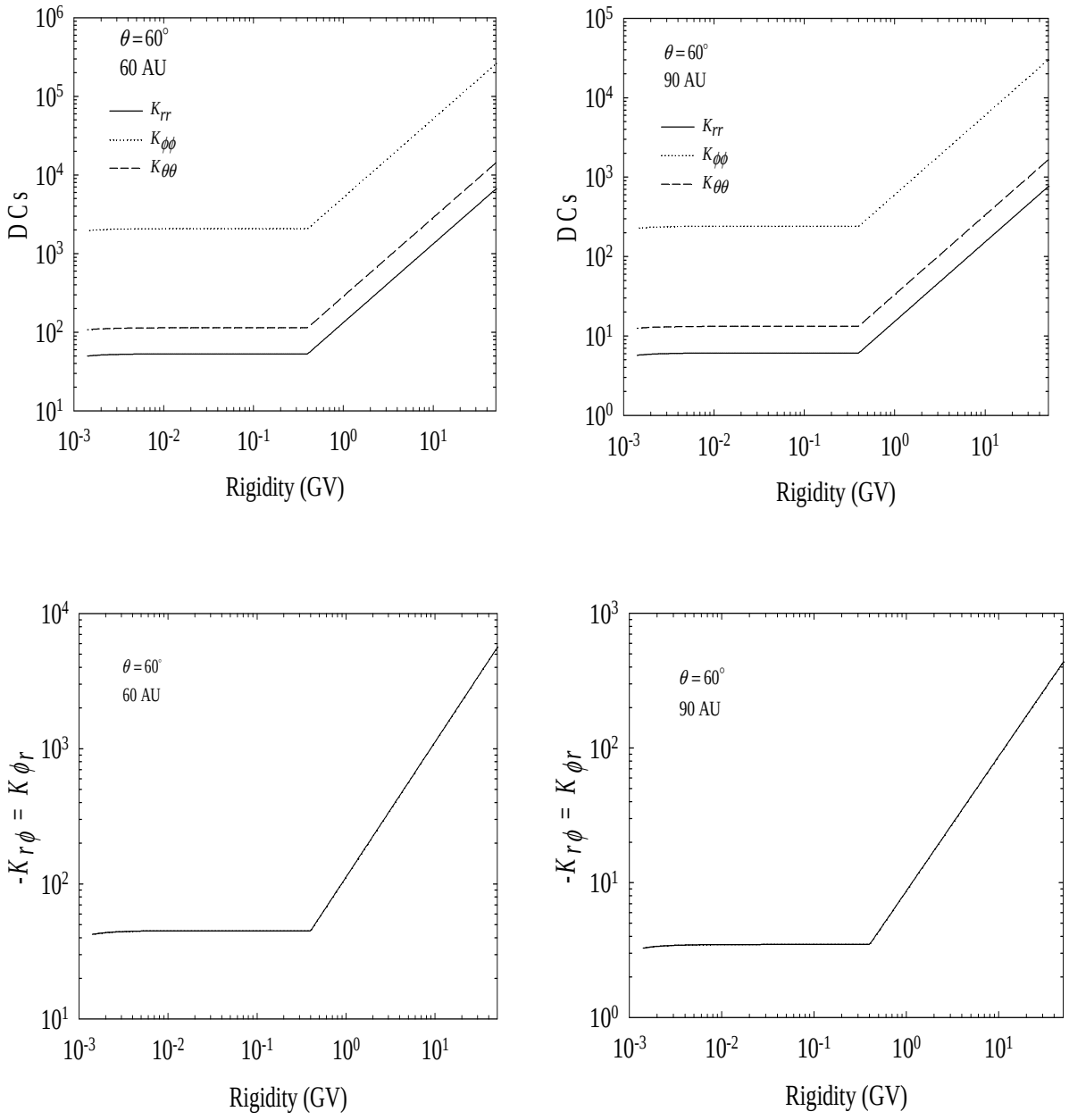

Figure 3.13: Computed rigidity dependence for K_{rr}, $K_{\phi\phi}$ and $K_{\theta\theta}$ (top panels) and $-\left(K_{r\phi} = K_{\phi r}\right)$ (bottom panels) at 60 AU and 90 AU, with θ = 60°.

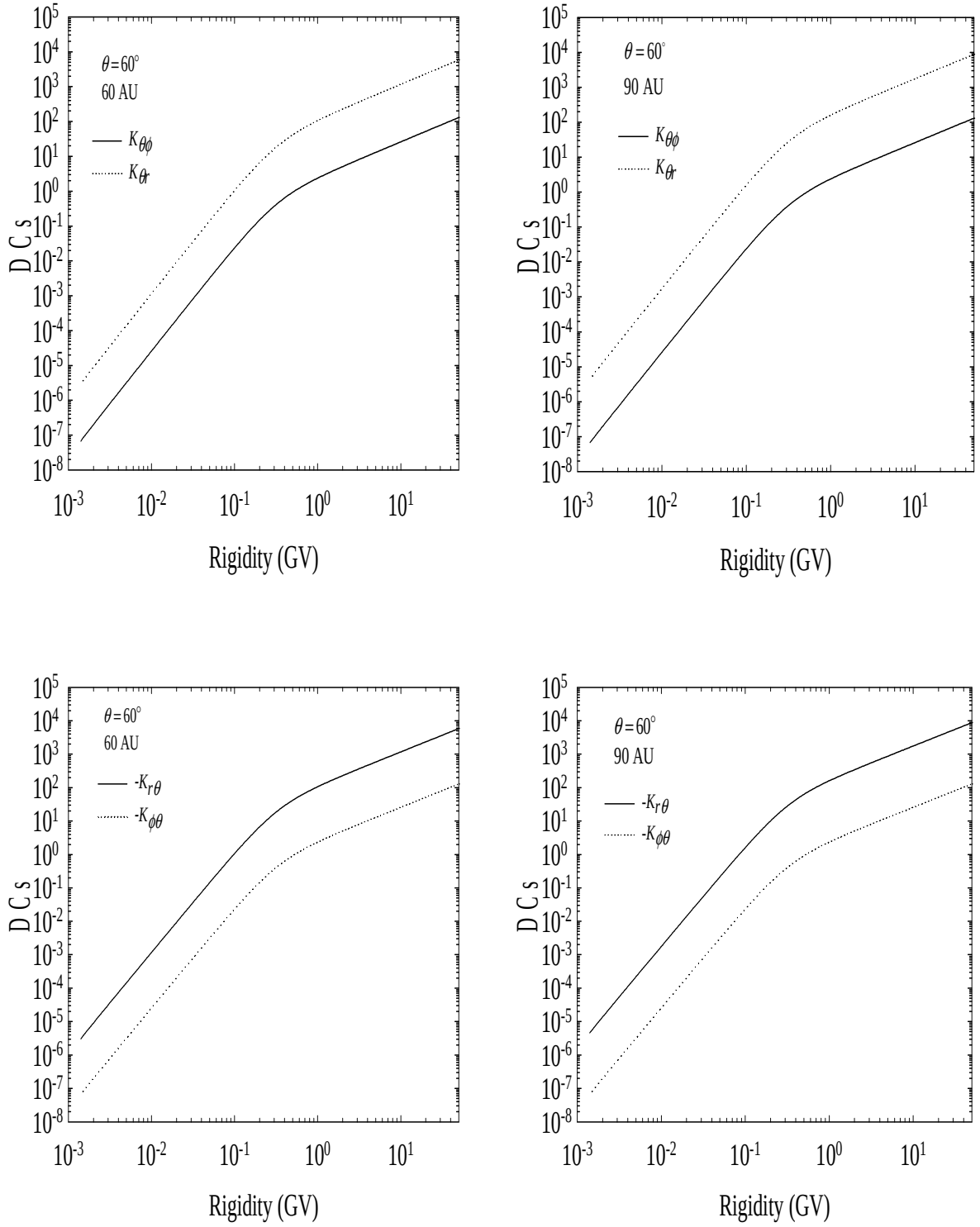

Figure 3.14: Computed rigidity dependence of $K_{\theta\phi}$ and $K_{r\theta}$ (top panels) and $-K_{\phi\theta}$ and $-K_{r\theta}$ (bottom panels) at 60 AU and 90 AU with θ = 60°.

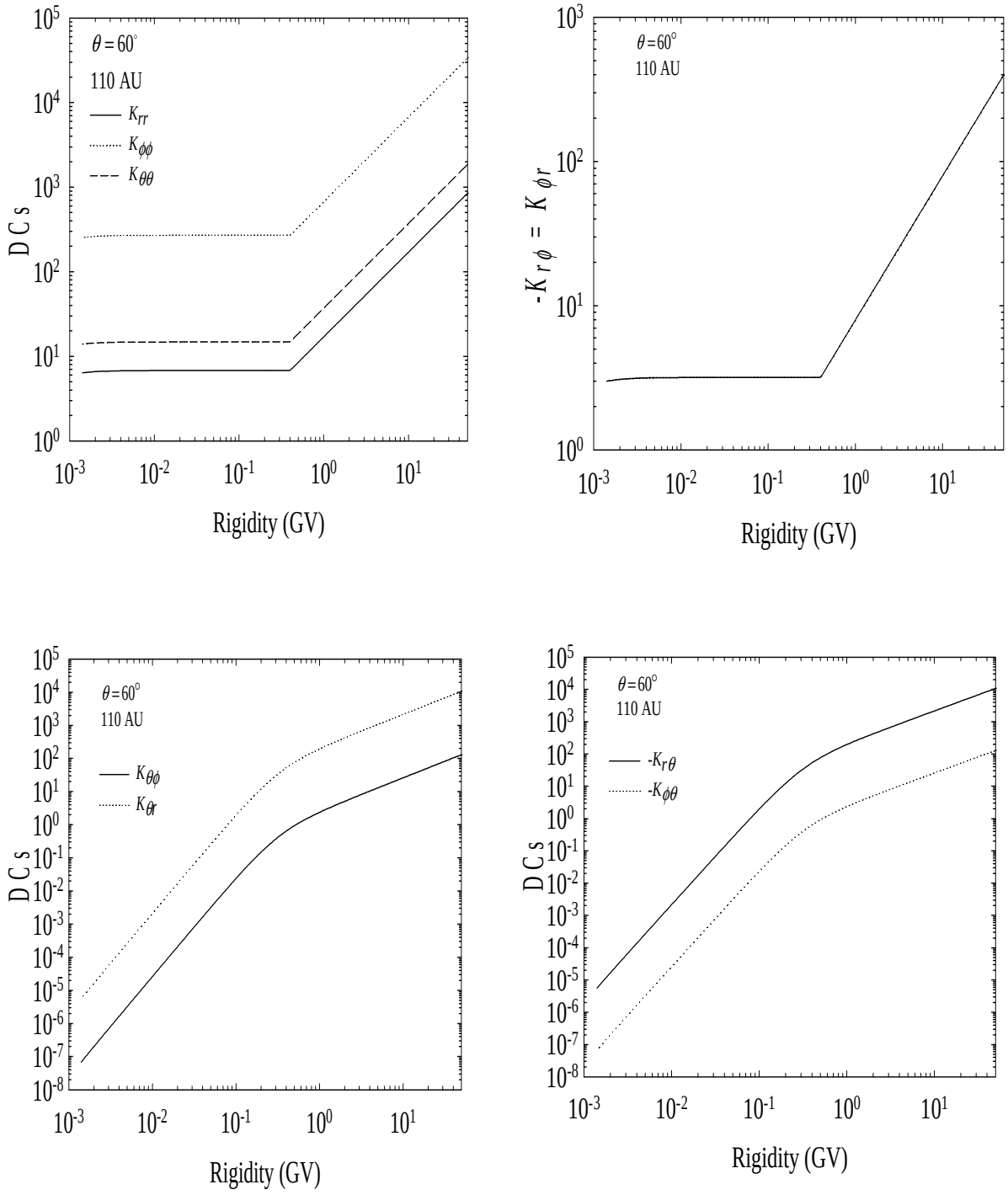

Figure 3.15: Computed rigidity dependence of K_{rr}, $K_{\phi\phi}$ and $K_{\theta\theta}$ (top left) and $-K_{r\phi} = K_{\phi r}$ (top panel right) at 110 AU, with θ = 60°. Bottom panels show the rigidity dependence of $K_{\theta\phi}$ and $K_{\theta r}$ and $-K_{\phi\theta}$ and $-K_{r\theta}$, respectively.

3.9.1.2. Radial dependence

Figure 3.16 shows the computed radial dependence of the DCs with θ = 60° and from 1 AU to 120 AU where the HP boundary is assumed. The jump in the DCs, that is the lower values in the heliosheath, is introduced so that the radial profile intensities observed by Voyager 1 beyond the TS can be reproduced. This will be shown in the next chapters. It is expected that the turbulence beyond the TS and inside the heliosheath increases and thus causing the DCs to drop significantly over the TS to stay smaller up to the HP. See also the discussion by Strauss (2010), Strauss et al. (2010, 2011) and Nkosi et al. (2011).

The top panel of Figure 3.16 shows the radial dependence of $K_{||}$ and $K_{\perp r}$ computed for 12 MeV electrons with θ = 60°. Both are increasing steadily with radial distance for the most of the heliosphere, as expected from Equations (3.38) to (3.41). With r > 80 AU, both $K_{||}$ and $K_{\perp r}$ abruptly decrease to continue with a less strong radial dependence to the HP, according to Equations (3.42) and (3.43). The bottom panel shows the radial dependence of K_{rr}, $K_{\phi\phi,}$ $K_{\theta\theta}$. With $r < 10$ AU, the radial dependence of K_{rr} is different, changed by the terms depending on the spiral angle of the HMF as given by Equation (3.12); with $r > 10$ AU it increases to the abrupt change at r = 80 AU. For $K_{\phi\phi}$ the radial dependence is similar to that of $K_{||}$ except in the inner heliosphere where it differs slightly. The radial dependence of $K_{\theta\theta}$ is identical to that $K_{||}$ and $K_{\perp r}$.

In Figure 3.17 the radial dependence of $-(K_{r\phi} = K_{\phi r})$ (top panel), $K_{\theta\phi}$ and $K_{\theta r}$ (middle panel), $-K_{r\theta}$ and $-K_{\phi\theta}$ (bottom panel) are illustrated for 12 MeV electrons with θ = 60°. Both $-\left(K_{r\phi} = K_{\phi r}\right)$ display the assumed rapid decrease in the outer heliosphere. In contrast, $K_{\theta\phi}$, $K_{\theta r}$, $-K_{r\theta}$ and $-K_{\phi\theta}$ do not show this rapid change because the assumptions is that the drift coefficient which determines these DCs does not change abruptly in the outer heliosphere.

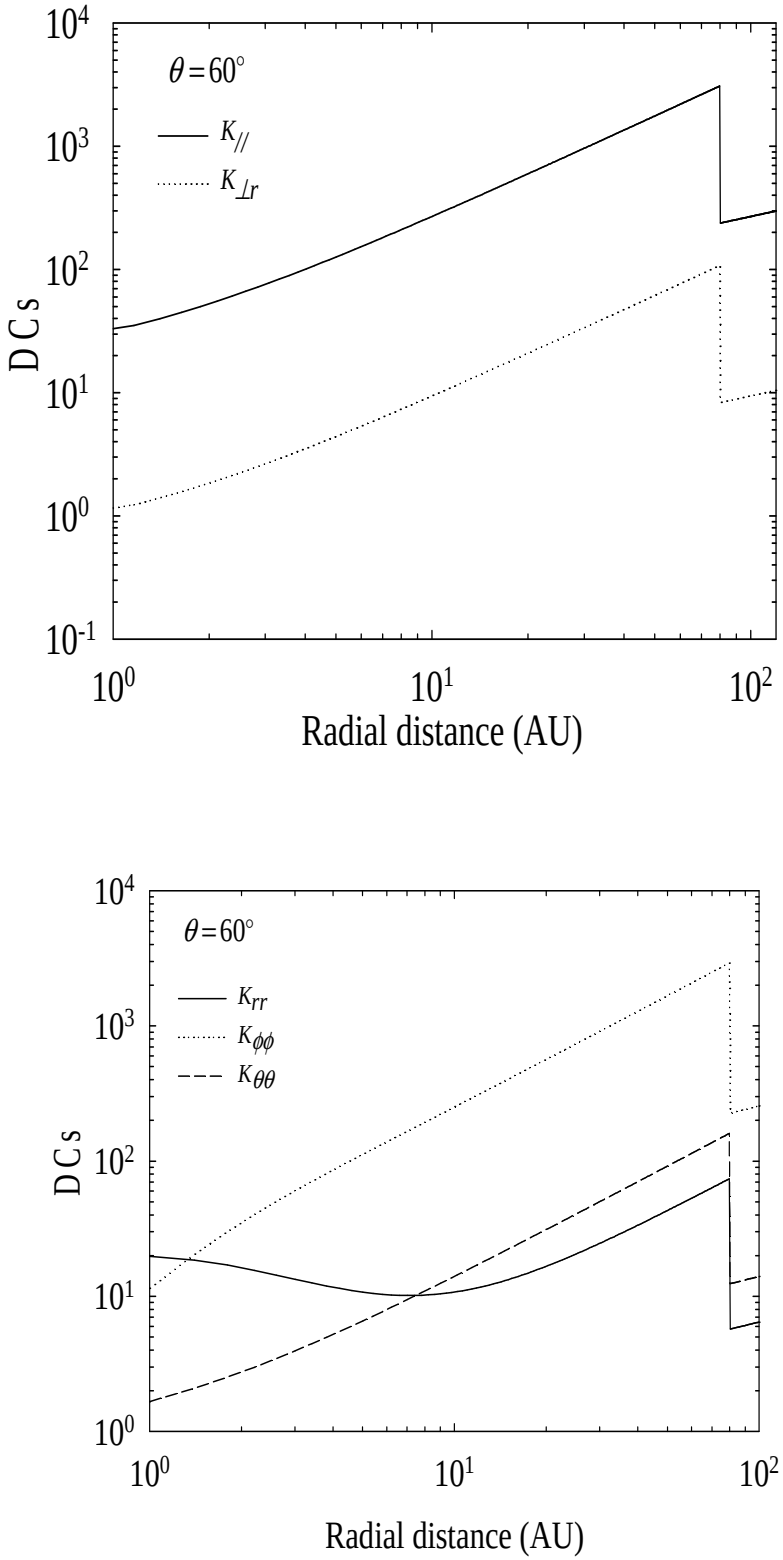

Figure 3.16: Computed radial dependence of the DCs for 12 MeV electrons with θ = 60°. Top panel for $K_{||}$ and $K_{\perp r}$, the bottom panel for K_{rr}, $K_{\phi\phi,}$ $K_{\theta\theta}$.

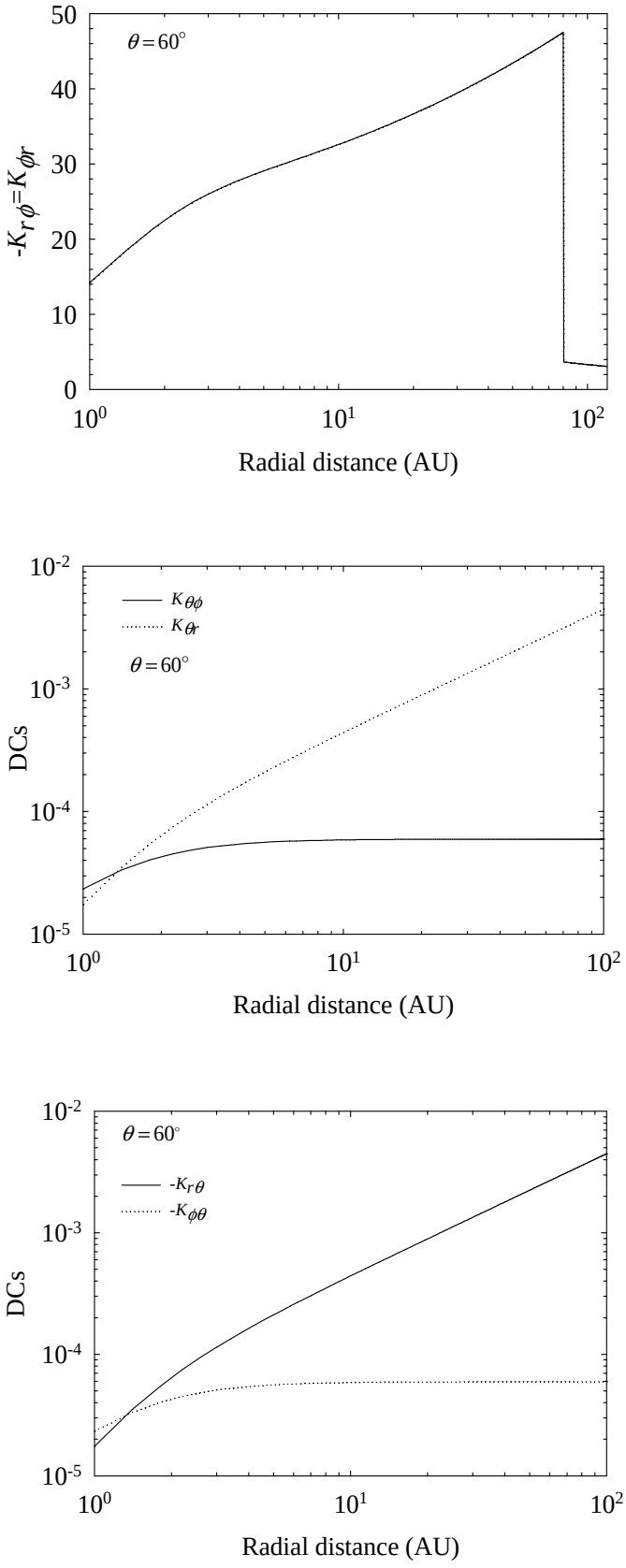

Figure 3.17: Computed radial dependence for 12 MeV electrons with θ = 60°; top panel for $-\left(K_{r\phi} = K_{\phi r}\right)$, middle panel for $K_{\theta\phi}, K_{r\theta}$; bottom panel for $-K_{r\theta}$ and $-K_{\phi\theta}$ respectively.

3.9.1.3. Latitudinal dependence

Figure 3.18 shows the polar (latitudinal) dependence of K_{rr} at 1 AU, 5 AU, 60 AU, 90 AU and 110 AU. It is small in the equatorial plane, large at the pole(s) because it is dominated there by $K_{\parallel}$. For $\theta > 20°, K_{rr}$ is almost constant for 60 AU, 90 AU and 110 AU, increasing significantly below 20° resulting in K_{rr} having large values at the poles. However, the polar dependence at 1 AU and 5 AU is different.

The top panel of Figure 3.19 shows the polar dependence of $K_{\phi\phi}$ again at 1 AU, 5 AU, 60 AU, 90 AU and 110 AU. Unlike K_{rr}, $K_{\phi\phi}$ is large in the equatorial plane and small at the poles because it is dominated by $K_{\perp r}$. For $\theta > 5°, K_{\phi\phi}$ is constant at 60 AU, 90 AU and 110 AU with the largest value obtained at 60 AU; for $\theta < 5°$, $K_{\phi\phi}$ decreases sharply. At 5 AU, $K_{\phi\phi}$ is constant with $\theta > 20°$, to decrease sharply below 20°, becoming small at the poles. At 1 AU, a similar but less pronounced pattern is followed. The middle panel shows the latitudinal

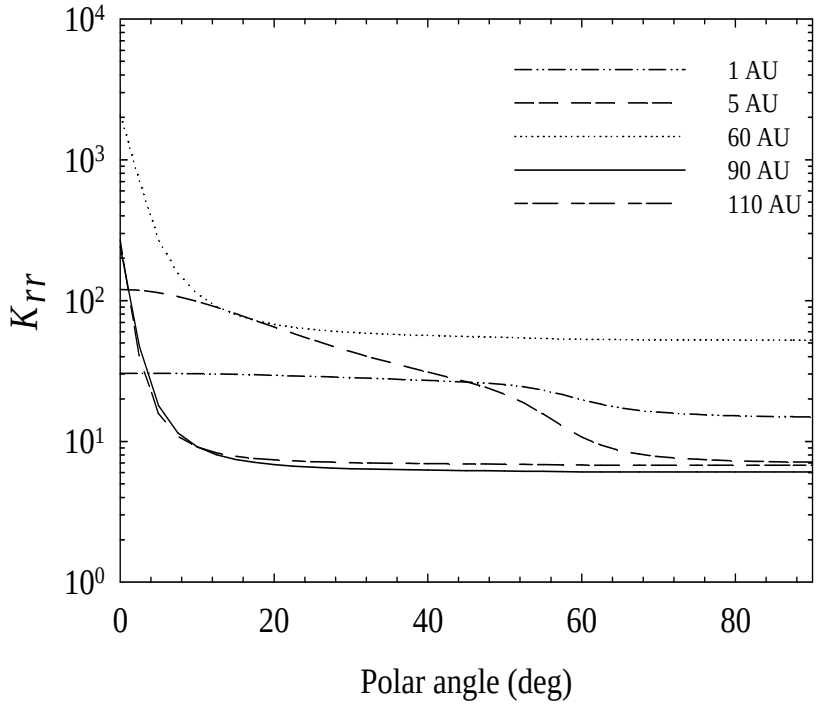

Figure 3.18: Computed polar (latitudinal) dependence of K_{rr} for 12 MeV electrons at 1 AU, 5 AU, 60 AU, 90 AU and 110 AU.

dependence of $K_{\theta\theta}$ at 1 AU and 5 AU. As before it displays the polar dependence caused by enhancing $K_{\theta\theta}$ through Equation (3.33), depending on the value of *d*, the enhancement factor. This has an effect on the computed polar (latitudinal) gradients for electrons, through the whole heliosphere and it will be addressed further in section 6.2.2. See also Potgieter (1996, 2000), Burger et al. (2000) and Ferreira et al. (2001a). The bottom panel shows the polar dependence for $-(K_{r\phi} = K_{\phi r})$ at 1 AU, 5 AU, 60 AU, 90 AU and 110 AU. At 1 AU and 5 AU, they are small at the poles. This is not the case at 60 AU, 90 AU and 110 AU. At these radial distances they have a small value in the equatorial plane, and large at the poles, because for $r > 10$ AU, $K_{\perp r}$ dominates these DCs according to Equation (3.15).

In Figure 3.20, the top left panel shows the polar dependence of $K_{\theta r}$ at 1 AU, 5 AU, 60 AU, 90 AU and 110 AU. The general trend is small in the equatorial plane becoming larger towards the poles. At 60 AU, 90 AU and 110 AU the values are the same. The top right panel shows the polar dependence of $K_{\theta\phi}$ at similar radial distances. Its value is quite small, decreasing towards the poles. At larger radial distances e.g. 60 AU, 90 AU and 110 AU it is larger with an increasing trend towards the poles. The bottom panels show the latitudinal dependence of $-K_{\phi\theta}$ and $-K_{r\theta}$ which are identical to the above mentioned DCs except for their sign, see Equation (3.11). Overall $K_{\theta\phi}$, $K_{\theta r}$ $-K_{\phi\theta}$ and $-K_{r\theta}$ have small values for all the radial distances discussed above.

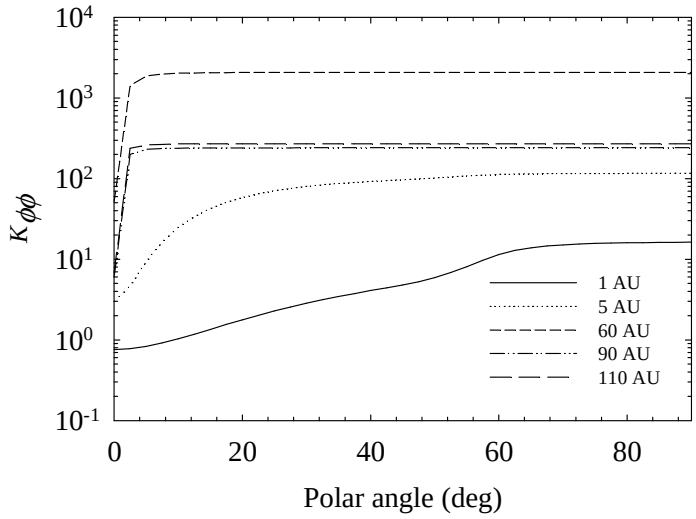

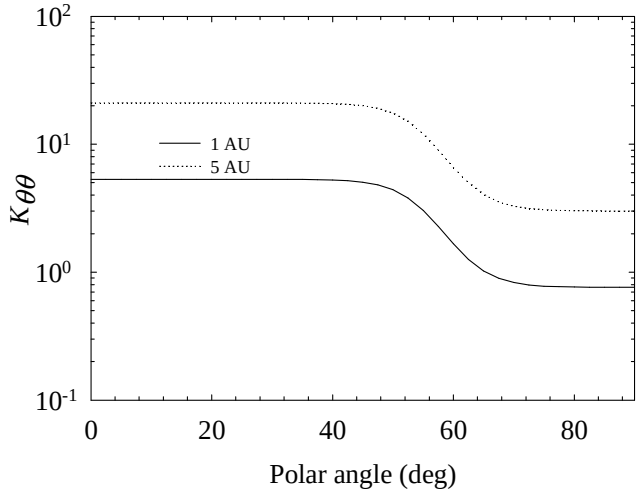

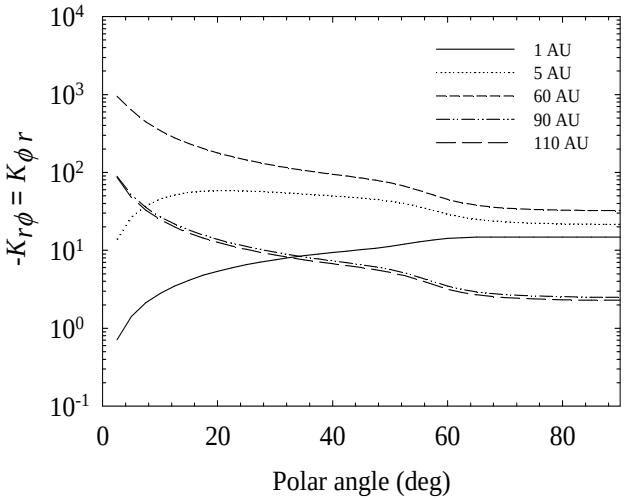

Figure 3.19: Computed latitudinal dependence of $K_{\phi\phi,}$ $K_{\theta\theta}$ and $-(K_{r\phi} = K_{\phi r})$ for 12 MeV electrons. Top panel shows $K_{\phi\phi}$, middle panel shows $K_{\theta\theta}$, bottom panel shows $-(K_{r\phi} = K_{\phi r})$.

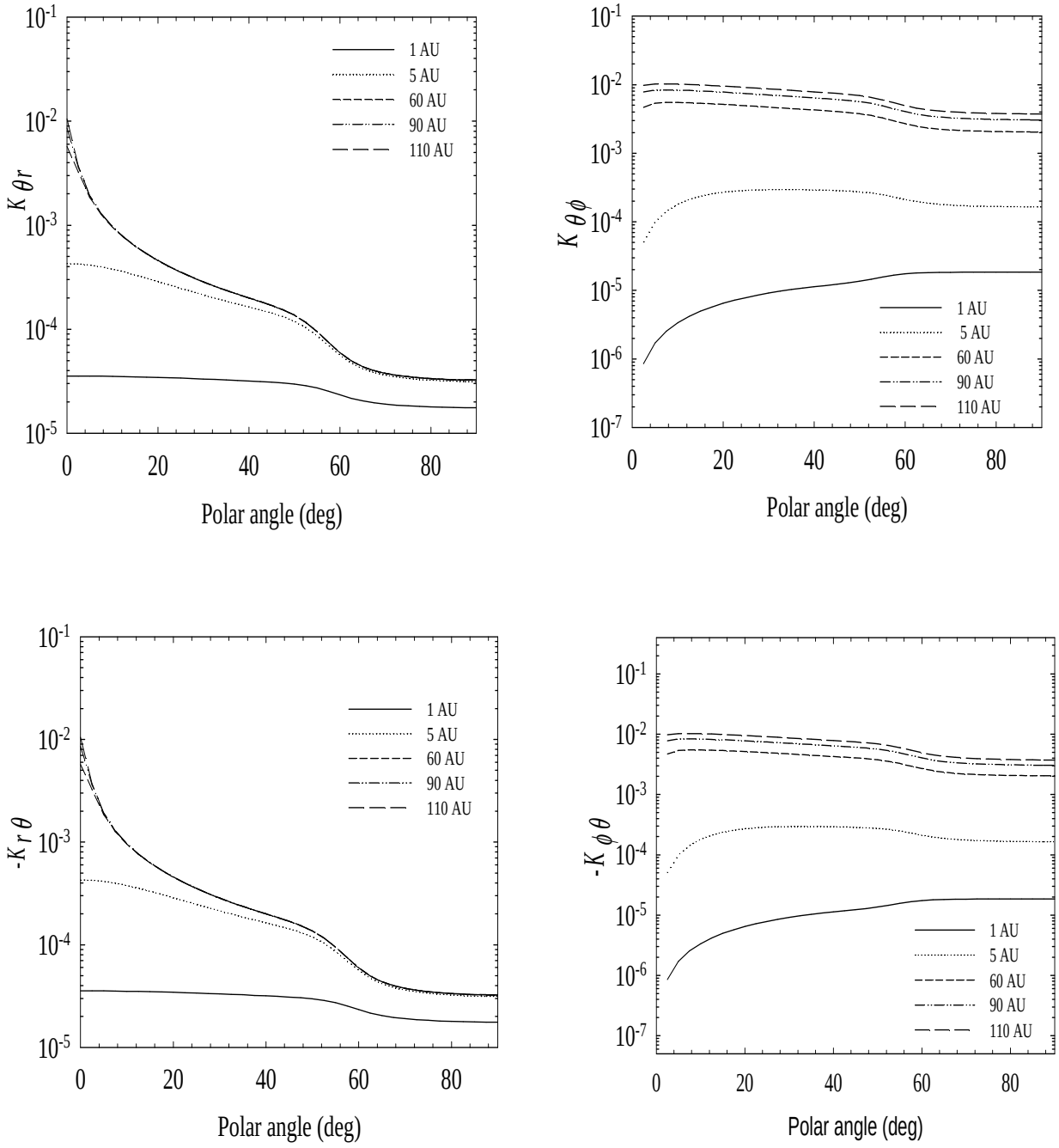

Figure 3.20: Computed polar dependence of $K_{\theta\phi}$, $K_{\theta r}$ $K_{\phi\theta}$ and $K_{r\theta}$ for 12 MeV electrons at 1 AU, 5 AU, 60 AU, 90 AU and 110 AU. Top panels show $K_{\theta r}$ and $K_{\theta\phi}$, bottom panels show - $K_{\phi\theta}$ and- $K_{r\theta}$.

3.10. Summary and conclusions

This chapter gave a brief background on the heliospheric transport equation, the 3D modulation model and aspects of the diffusion tensor. Firstly a brief history about the 3D modulation model was given without going into too much detail. The transport equation and its form in spherical coordinates were discussed. The diffusion tensor and a brief background about the parallel and the perpendicular diffusion coefficients based on the QLT were given.

The rigidity dependence, spatial dependence and latitudinal dependence of the elements of the diffusion tensor were given based on the work from Nkosi (2006) and followed by the rigidity, spatial and latitudinal dependence of the diffusion coefficients constructed for the purpose of this study.

These diffusion coefficients, together with the new local interstellar spectrum constructed in the following chapters, for GCRs electrons assure compatibility with electron observations in the outer heliosphere while maintaining compatibility with observations made at Earth.

In the next chapter, the background about these galactic and local interstellar spectra for GCRs electrons is given together with the reasons why it was necessary to find a new local interstellar spectrum for electrons.

Chapter 4

Very local interstellar spectra

4.1. Introduction

One of the important aspects of the modulation of GCRs in the heliosphere is the local interstellar spectra (LIS). This serves as input spectra specified at an assumed modulation boundary and then modulated throughout the heliosphere as a function of energy and time. Because of this modulation and the fact that the full nature of the heliospheric diffusion coefficients is not yet known, all LIS's at low energies are still not well known and understood, and therefore controversial. Recently the Voyager 1 electron observations, especially since 2010 when it was already beyond 112 AU, have given good insight on how the electron LIS could actually look like at low energies, suggesting a simple power law. In this chapter, different calculations and forms of the electron LIS are discussed, as well as what it implies when used in a modulation model. The electron LIS that gives the best results when modeling is compared to observations will be selected as a research result and will then be used as the electron LIS for the rest of this study.

4.2. Galactic spectra versus very local interstellar spectra

Galactic spectra (GS) are referred to as spectra that are produced from astrophysical sources, usually assumed to be evenly distributed through the Galaxy, typically far from the heliosphere. These spectra are computed using e.g. the well-known GALPROP propagation model (e.g. Moskalenko et al. 2002). Over the years this model has been improved and extended, becoming more and more sophisticated, containing substantial physics. For a review, see Strong et al. (2007).

Figure 4.1 shows examples of computed GS for different cosmic ray species computed with the GALPROP model. From this figure it is clear how diverse these GS can be. In heliospheric modulation studies, these GS, wrongly referred to as LIS's, are commonly used as input spectra in models, to be modulated up to Earth (e.g. Moskalenko et al. 2002; Webber 1999 and Langner et al. 2001).

Since GS do not contain the contributions of any specific (local) sources within parsecs from the heliosphere, an interstellar spectrum could be different from a GS, which could on its turn be different from a local interstellar spectrum (thousands of AU away), which could be different from a very local interstellar spectrum (VLIS), say 300 AU away from the Sun. If known, the latter should be the ideal spectrum to be used as an input spectrum for modulation models.

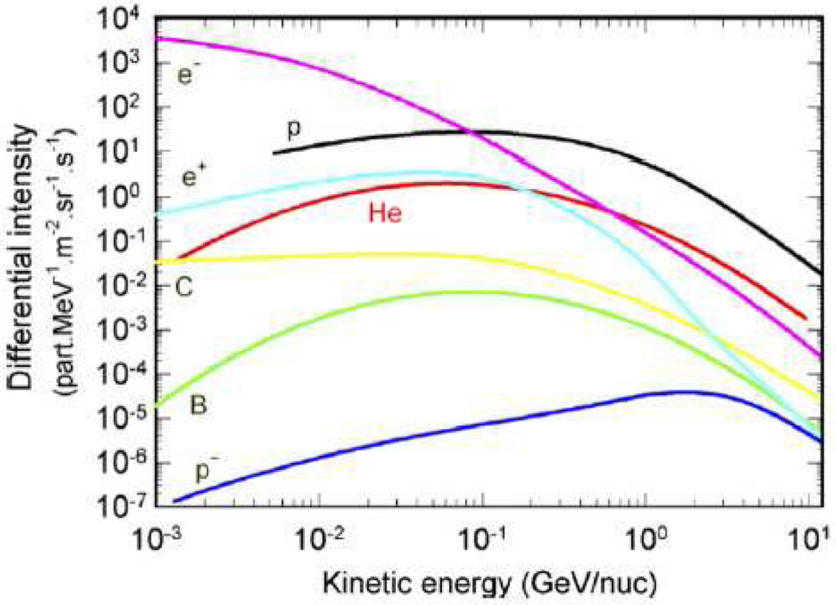

Figure 4.1: A compilation of computed galactic spectra, from Potgieter (2008), for cosmic ray protons, anti-protons, electrons, anti-electrons, Helium, Boron and Carbon (see also Langner et al. 2001 and Moskalenko et al. 2002).

A VLIS may be defined as the spectrum just outside the heliosphere, that is, the location where the heliosphere does not disturb the local interstellar medium any more. Scherer et al. (2011) showed that a VLIS for protons may be slightly modulated in the outer heliosheath, so that there may be a difference between a VLIS and the proton spectrum at the HP. Both Voyager spacecraft seem to be close to the HP, so that one can argue that at least Voyager 1

is already observing HP spectra. Potgieter and Ferreira (2002), Ferreira and Potgieter (2002), Langner and Potgieter (2004a) and Langner and Potgieter (2004b) showed that the heliospheric TS can indeed re-accelerate low-energy galactic electrons to higher energies so that strictly speaking a HP spectrum could be different from a TS spectrum. In fact, such a TS spectrum could even be higher than a HP spectrum, depending on the energies considered. However, because the TS has been observed as rather weak (Richardson et al. 2008) this effect is expected to be small.

Because of the controversy surrounding the terminology involved in defining these spectra and the lack of observations beyond the HP, the habit of calling the GS a LIS, and assuming the VLIS equal to the HP spectrum, is continued in this work. The next section gives some examples of computed galactic electron spectra as found in the literature**.**

4.3. Computed galactic electron spectra

Figure 4.2 shows several GS for electrons computed with earlier versions of the GALPROP propagation model, done between 1994 and 2000. In the top panel, the differential intensity is multiplied by E^2 and compared to Pioneer 10 data. The first and highest LIS, indicated as Strong94 in the top panel, was reported by Strong et al. (1994). This GS for electrons was used as the LIS in earlier modulation studies (e.g. Potgieter 1996 and Ferreira et al. 2000). Later, Strong et al. (2000) argued that this LIS was too high and much lower spectra were computed, indicated as 19-004526 (dashed line) and as 19-004508 (dashed dotted line), in the lower panel according to their numbering (see also Moskalenko et al. 2000). Langner et al. (2001) recalculated the electron spectrum using a phenomenological approach, including also radio data for calculations at lower energies, and found a LIS value that was between the spectra reported by Strong et al. (1994, 2000). This LIS is shown together with the GALPROP LIS's in the bottom panel, this time in units of particles m^{-2} s^{-1} sr^{-1} MeV^{-1}, as is mostly used in modulation studies.

Significant theoretical modifications were made to the GALPROP code as reported by Ptuskin et al. (2006) when they re-examined some of the physical processes in galactic space, involving in particular the rigidity dependence of the diffusion of cosmic rays through the Galaxy. They computed the primary and secondary spectra for different cosmic ray species.

Here, only the different GS for electrons are discussed and shown in Figure 4.3, without going into too much detail.

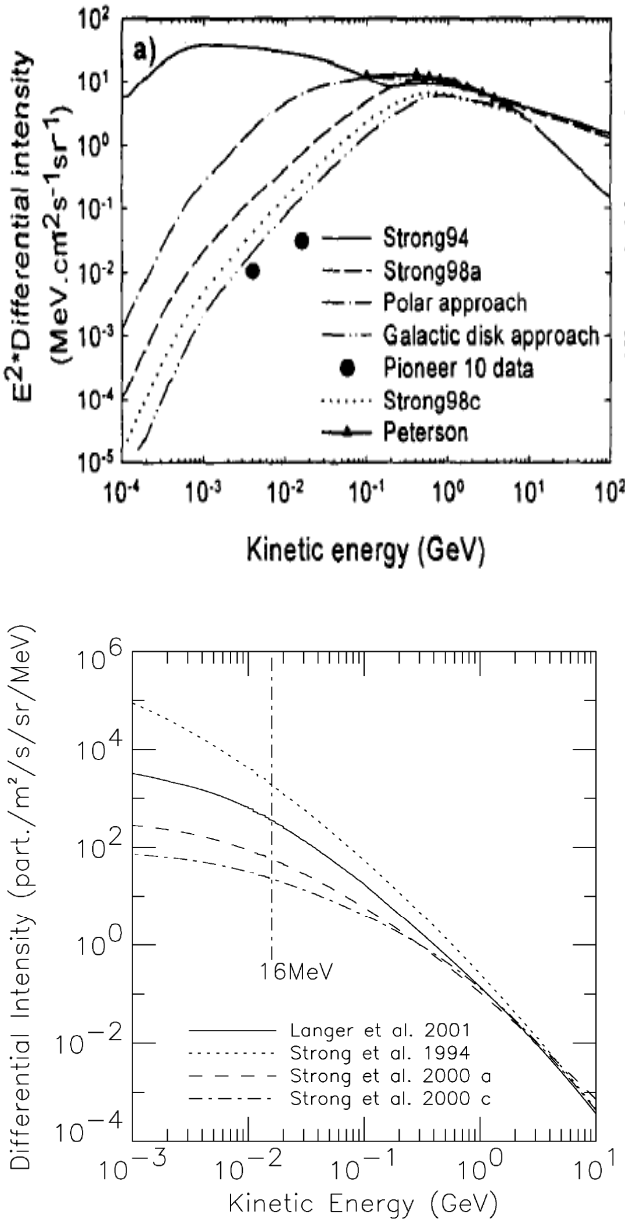

Figure 4.2: The computed galactic electron spectra from the GALPROP model. Top panel shows the intensities multiplied by E^2 together with Pioneer 10 data: Strong94 (Strong et al. 1994), Strong98a,c (Strong et al. 2000). Bottom panel shows these galactic spectra in a form that is normally used in modulation models together with the Langner LIS (Langner et al. 2001; Ferreira and Potgieter 2002).

They used three different approaches, diffusive reacceleration with damping (DRD model); plain diffusion (PD model) with an ad hoc break in the galactic diffusion coefficient (only

one is used) and an approach with distributed reacceleration (DR model) and power law diffusion with no breaks (see also Moskalenko et al 2002; Ptuskin et al. 2006). The PD and the DR models give a GS with relatively high intensities at low energies while the DRD model produced a completely different GS, with much lower intensities, already for $E < 3$ GeV. The modulated spectra compare reasonably to the observations for all three models but only down to about 1 GeV. At lower energies, the modulated spectra are far too high, especially for the DR and PD models, indicating that these GS are too high at energies below ~ 1 GeV. It must also be noted that the Force-Field modulation model is strictly not valid for electron modulation at energies below about 1 GeV.

Webber and Higbie et al. (2008) used a Monte Carlo Diffusion Model for electron propagation in the galaxy to calculate new electron GS below 1-2 GeV. They referred to these GS as interstellar spectra. This study was motivated by new experimental and theoretical developments (Ptuskin et al. 2006) related to both electron propagation in the galaxy and to the electron spectrum observed in the outer heliosphere by the Voyager spacecraft. From this observationally influenced point of view, they argued that the computed GS presented as an interstellar spectrum were too high at lower energies, in particular for electrons. They also emphasized that solar modulation effects should be properly handled in the outer heliosphere to reconcile Voyager 1 observations and observations at Earth with computed GS (Langner et al. 2001). For the details about the physics of these models, see Ptuskin et al. (2006) and references therein.

Figure 4.4 is taken from Webber and Higbie (2008); see their Figures 2 and 4. The two panels show a variety of their computed electron LIS spectra together with the calculated LIS from Langner et al. (2001) and Ptuskin et al. (2006), in comparison with observations near the Earth as described in the caption and Voyager 1 observations when it crossed the TS in 2004.95 at 94 AU and also ~3 years later in 2007.7 when it was at 105 AU, approximately 20 AU beyond the TS (McDonald et al. 2007). The top panel of Figure 4.4 shows three of their spectra (IS 2.4, 2.3 and 2.4) together with the PD and DRD approaches of Ptuskin et al. (2006) and the LIS of Langner et al. (2001). The three new spectra are basically the same down to ~500 MeV with IS 2.3 very similar to the LIS by Langner et al. (2001). Note that Webber and Higbie (2008) and Langner et al. (2001) utilized observed radio data to improve the spectral shape of the LIS at energies below ~50 MeV so that it is not so surprising that these LIS are about the same.

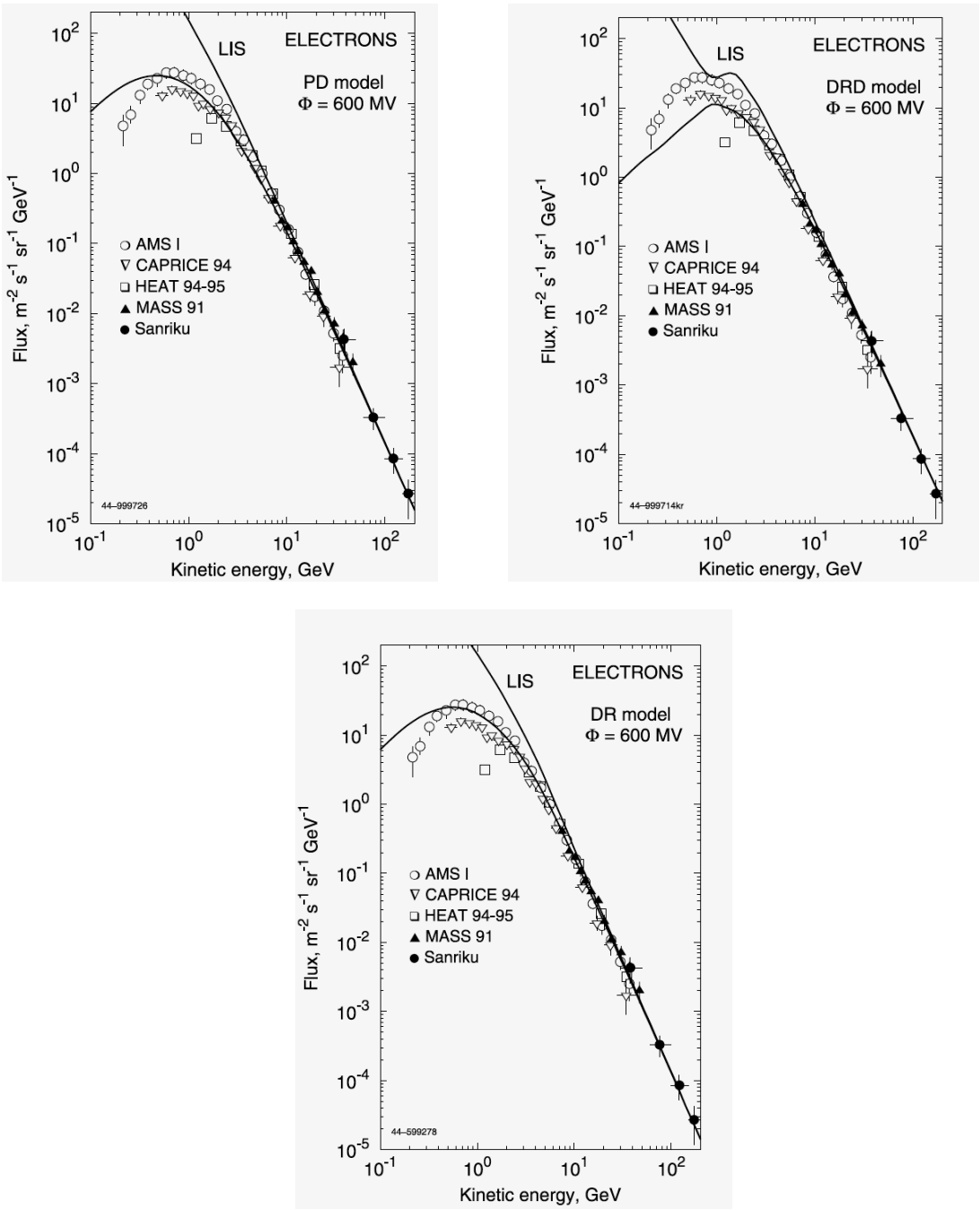

Figure 4.3: Computed galactic electron primary plus secondary spectra. Top panels show respectively the GS as calculated by Ptuskin et al. (2006) with a plain diffusion model (PD) and a re-acceleration and damping model (DRD), whereas the bottom panel shows the GS calculated with a re-acceleration model (DR). Also shown are modulated spectra at Earth obtained by using a simple Force-Field modulation model in comparison with observations from AMS-I (Alcaraz et al. 2000); CAPRICE 4 (Boezio et al. 2000); HEAT 94-95 (Du Vernois et al. 2001); MASS 91 (Grimani et al. 2002) and Sanriku (Kobayashi et al. 1999).

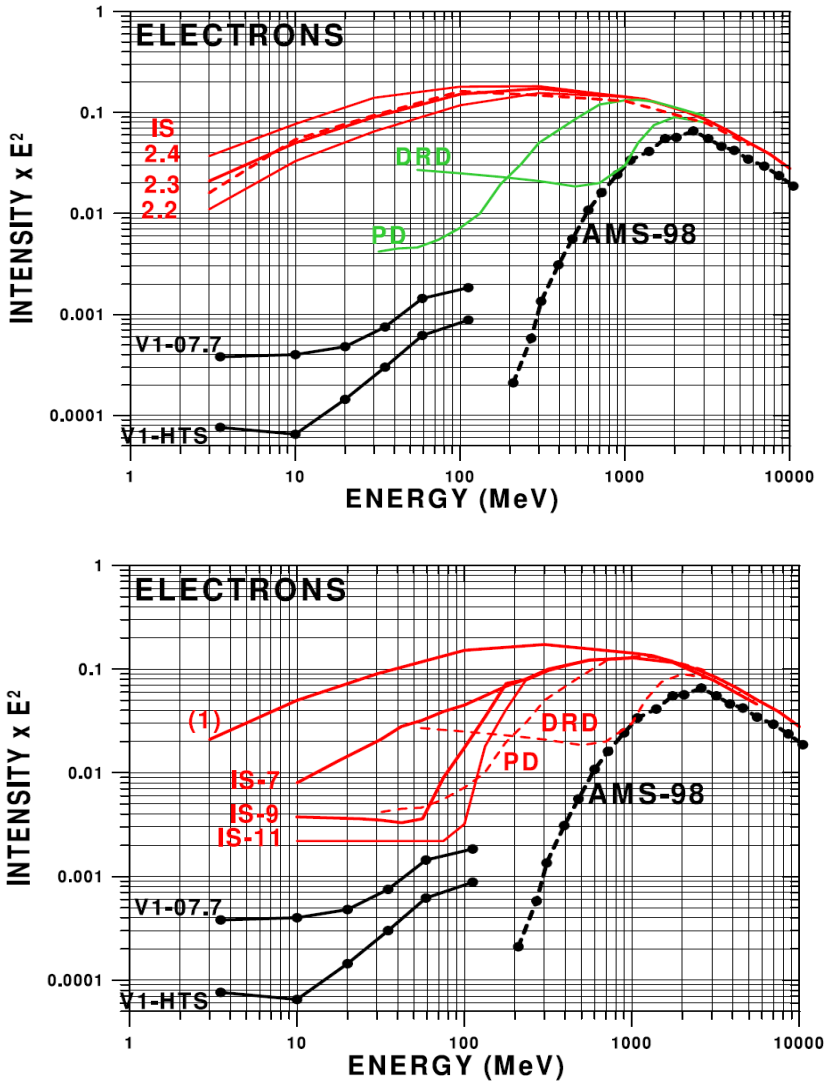

Figure 4.4: Top panel shows various computed electron LIS from Webber and Higbie (2008), indicated by IS 2.4, 2.3 and 2.2 in comparison with the LIS electron spectra calculated by Ptuskin et al. (2006), indicated by PD and DRD, whereas the dashed line is the LIS electron spectrum from Langner et al. (2001). The data points are AMS-1 electron measurements (Alcaraz et al. 2000) at Earth at the time of the 1998 modulation minimum (AMS-98) and Voyager 1 electron measurements (McDonald et al. 2007) at the time of its HTS crossing (V1-HTS) and ~3 years later (V1-07.7). Bottom panel shows again the observations with the PD and DRD approaches as mentioned above, now with various attempts by Webber and Higbie (2008) of computing the LIS using their Monte Carlo Diffusion model. Here, (1) indicates a reference spectrum with a source spectral index of -2.3 and a constant galactic diffusion coefficient below ~3.0 GV, and three computed spectra, indicated as IS-7, IS-9, and IS-11, all with a different rigidity dependence for the galactic diffusion coefficient. The intensities are in units of electrons m^2 sr^{-1} s^{-1} MeV^{-1} $\times E^2$ $(GeV)^2$.

Obviously, the PD and DRD approaches are drastically different because complex rigidity dependences for the galactic diffusion coefficient were utilized in the GALPROP code in order to calculate them. Webber and Higbie (2008) followed this approach, shown in the bottom panel of Figure 4.4 as spectra IS-7, IS-9 and IS-11. They are compared to a reference spectrum, indicated by (1), for which the galactic diffusion coefficient is simply assumed to be constant below ~3.0 GV. The peculiar form of spectra PD, DRD and IS-7, IS-9 and IS-11 are caused by different rigidity dependences for the galactic diffusion coefficient. This is clearly shown in Figure 4.5, taken from Webber and Higbie (2008); see their Figure 3.

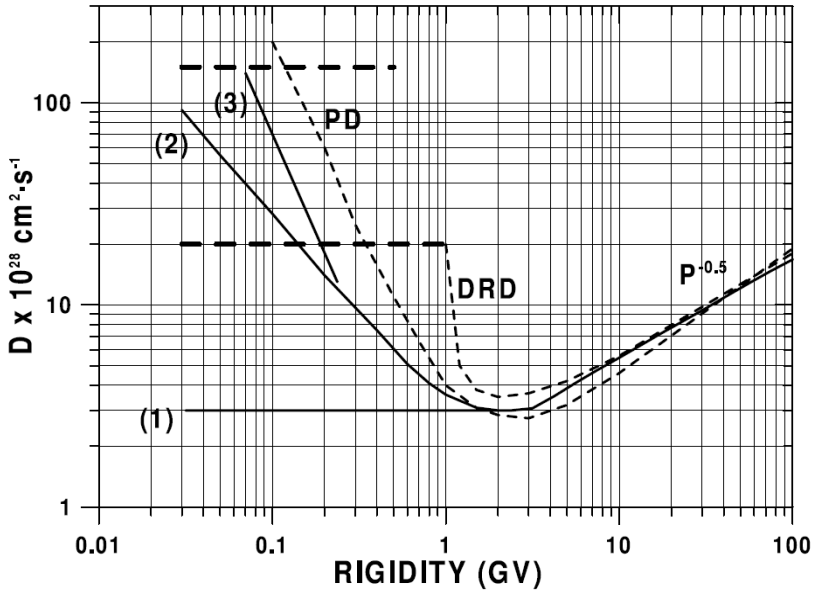

Figure 4.5: Computed rigidity dependence of the galactic diffusion coefficient used in various propagation models. (1) Shows the diffusion coefficient used to obtain the LIS electron spectra shown in Figure 4.4 top panel, (2) and (3) show the diffusion coefficient that are used to obtain the IS-7 electron spectrum and IS-11 spectrum in the bottom panel of Figure 4.4, respectively. PD and DRD are the ones used to obtain the PD and DRD spectra as shown in the bottom panel of Figure 4.4. From Webber and Higbie (2008).

Inspection of all these computed LIS, in comparison with electron observations, shows that some of them are unrealistic and can be eliminated as a meaningful LIS. The most obviously wrong one is the DRD spectrum because it touches the observations during 1998 at Earth at 700 MeV. This directly implies that there is no modulation of electrons in the heliosphere at this energy, which is impossible and thus illustrates a serious inconsistency with respect to

the near Earth observations. At different energies these spectra seem to do better. However, spectra IS-9 and IS-11 are also too low at energies between 50 to 100 MeV because the present Voyager 1 measurements are already higher. These spectral shapes can thus also be eliminated as plausible LIS's. Clearly, an effort has to be made to bring compatibility and consistency to these attempts in calculating appropriate LIS. This is partly the purpose of this study.

4.4. Mathematical description of different LIS's

This section gives the mathematical expressions for five electron LIS's published since the mid- 1990's e.g. by Strong et al. (1994, 2000), Langner et al. (2001) and from Webber and Higbie (2008). The spectra that will be used later are those from Langner et al. (2001) and Webber and Higbie (2008) in particular their IS-7. The equations are as follows:

From Strong et al. (1994, 2000)

LIS (19-004606) from Strong et al. (1994) is given by

$$j_{LIS} = 1.7 \exp\left(-2.83 - 5.37R + \frac{10^{-4} R}{P} \right), \tag{4.1}$$

with $R = \log(P)$.

The highest LIS (19-004526) of Strong et al. (2000) is given by

$$j_{LIS} = \frac{1.7\left(318.36 + 0.58P - 0.13P^2\right)}{\left(1.0 + 589.20P + 838.50P^2 + 1676.76P^3\right)}. \tag{4.2}$$

The lowest LIS (19-004508) from Strong et al. (2000) is given by

$$j_{LIS} = \frac{1.7\left(48.9 - 0.42P + 0.002P^2\right)}{\left(1.0 + 179.14P + 382.44P^2 + 175.59P^3\right)}. \tag{4.3}$$

From Langner et al. (2001)

If $P < 0.0026$ GV,

$$j_{LIS} = \frac{1.7\left(126.067 + 1.95\ln(P)\right)}{1 + 0.26\ln(P) + 0.02(\ln(P))^2},$$

if $0.026\ \text{GV} \le P < 0.1\ \text{GV}$,

$$j_{LIS} = 1.7\left(\frac{52.55 + 23.01P}{1.0 + 148.62P}\right)^2,$$

if $0.1\ \text{GV} \le P < 10\ \text{GV}$,

$$j_{LIS} = \frac{1.7\left(915.22 + 10.22P - 1.97\times10^{-3}P^2 + 3.023\times10^{-7}P^3\right)}{1 - 11.22P + 7532.93P^2 + 2405.01P^3 + 103.87P^4}, \tag{4.4}$$

if $P > 10\ \text{GV}$,

$$j_{LIS} = 1.5\exp\left(-0.89 - 3.22(\ln P)\right).$$

From Webber and Higbie (2008) IS-7

If $P < 0.0712\ \text{GV}$,

$$j_{LIS} = \frac{745.07 + 18975.36P - 25649.20P^2}{1 + 656.79P + 41019.96P^2},$$

if $0.0712\ \text{GV} \le P \le 1.0\ \text{GV}$,

$$j_{LIS} = \frac{53.86 - 973.69P + 258.87P^2}{1 + 87.52P - 1541.76P^2 - 3426.9890P^3},$$

if $1.0\ \text{GV} < P \le 10\ \text{GV}$,

$$j_{LIS} = \frac{0.13 - 6.6\times10^{-3}P + 5.49\times10^{-5}P^2}{1 - 1.32P + 1.08P^2 + 0.23P^3}, \tag{4.5}$$

if $P > 10\ \text{GV}$,

$$j_{LIS} = \exp\left(-0.89 - 3.22\ln(P)\right).$$

Here j_{LIS} is the differential intensity in units of particles $\text{m}^{-2}\ \text{s}^{-1}\ \text{sr}^{-1}\ \text{MeV}^{-1}$, and $P = pc/q$ is rigidity in units of GV, where p is the momentum of the particles with charge q, and c the speed of light.

4.5. Modulation implications of different electron LIS's

This section focuses on the Langner et al. (2001) electron LIS, hereafter referred to as the Langner LIS, and the Webber and Higbie (2008) IS-7 electron LIS, hereafter referred to as Webber IS-7. The two LIS's are used in the modulation model with diffusion coefficients as discussed in chapter 3, in order to illustrate and describe the corresponding modulation effects. These modulated spectra as computed will be compared, where possible, to observations as a test of how realistic the results are, as well as to illustrate the main features and characteristics of electron modulation in the heliosphere.

4.5.1. Modulation of different electron LIS's

The main features of the modulation of GCRs electrons in the heliosphere as described by a full 3D model are illustrated in this section. This is based on two selected LIS's as given

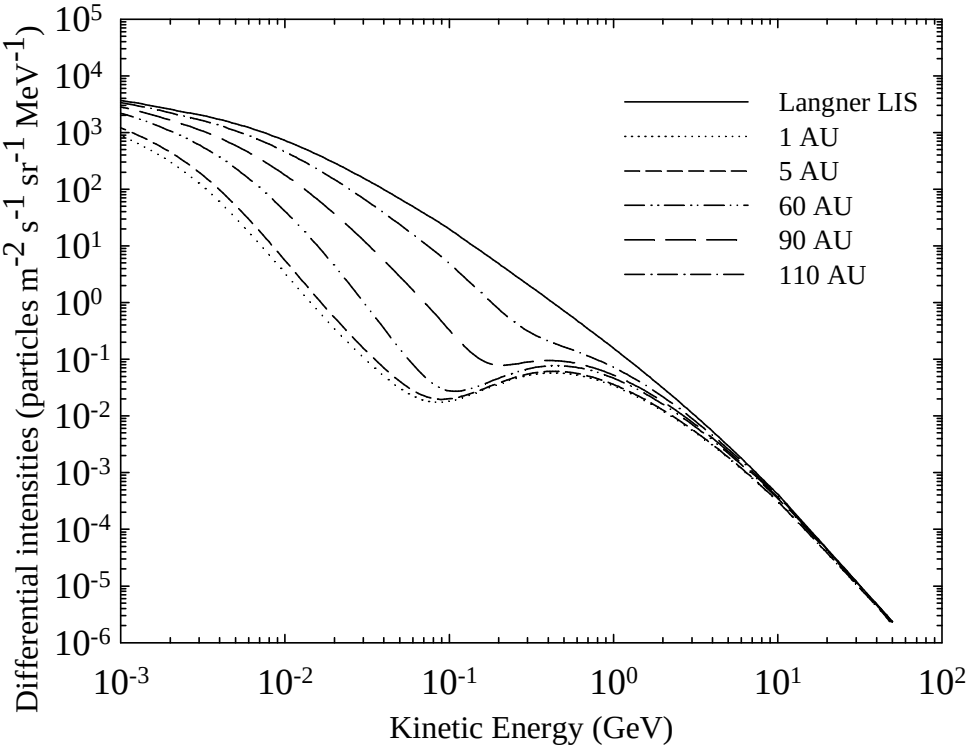

Figure 4.6: Computed electron spectra at radial distances of 1 AU, 5AU, 60 AU, 90 AU and 110 AU in the equatorial plane using Langer LIS.

above, the Langner LIS and Webber IS-7. The Langner LIS is used to obtain what can be called reference solutions for this study since it has been used successfully in the past (e.g. Ferreira 2002; Langner 2004; Moeketsi 2004 and Nkosi 2006). All the LIS used here are normalized at 50 GeV, the energy at and above which it is assumed that no modulation occurs.

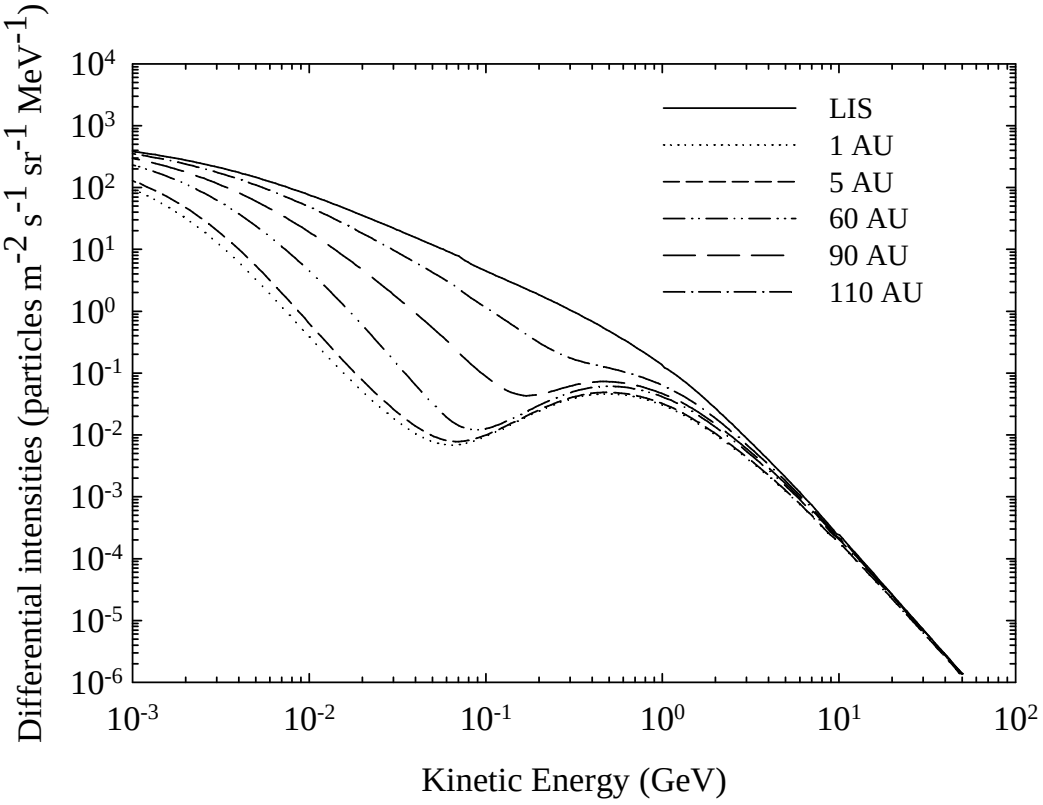

Figure 4.7: Computed electron spectra at 1AU, 5 AU, 60 AU, 90 AU and 110 AU in the equatorial plane with respect to the Webber IS-7 spectrum used as LIS.

In Figures 4.6 and 4.7 the computed modulated spectra, with respect to the two assumed LIS's, are shown at radial distances of 1 AU, 5 AU, 60 AU, 90 AU and 110 AU, respectively. The diffusion coefficients used in the model were discussed in chapter 3; see Figures 3.2 and 3.3. The Webber IS-7 LIS is almost the same as the Langner LIS down to 1 GeV. Below this energy, the Webber IS-7 is less than the Langner LIS, almost a factor of 10 at $E = 10^{-3}$ GeV. Comparing the modulated spectra in Figure 4.6 with those in Figure 4.7, the effects of using different LIS's are illustrated. Qualitatively, the results look similar, with basically the same features e.g. the modulated spectra reach a peak around 500 MeV, decreasing to around 50

MeV below which the intensity rises sharply to produce little modulation at 10^{-3} GeV. This is in sharp contrast to proton modulation (e.g. Potgieter 1996, 2000). In both cases the 1 AU and 5 AU spectra are indistinguishable above 100 MeV. Below 100 MeV the two start to differ but not much, not even at low energies.

The decreasing modulation (difference between the modulated spectra and the LIS) with decreasing energy to eventually producing rather little modulation at very low energies in both cases is caused by the assumed rigidity dependence of the relevant diffusion coefficients; see top panels of Figure 3.2 and also Figure 3.3. It will be illustrated in later chapters how electron modulation changes when the rigidity dependence of the diffusion coefficients is changed as was discussed in detail in section 3.9. This will then be compared to Voyager 1 observations.

Figure 4.8 shows the computed ratio between the Langner and Webber LIS as a function of kinetic energy. The purpose of this graph is to illustrate how the two LIS's differ at different energies since this is not so obvious from Figures 4.6 and 4.7. It follows that this ratio as a function of kinetic energy is always larger than unity, with the smallest difference around 1 GeV, implying that the Langner LIS is higher than the Webber LIS at all relevant energies.

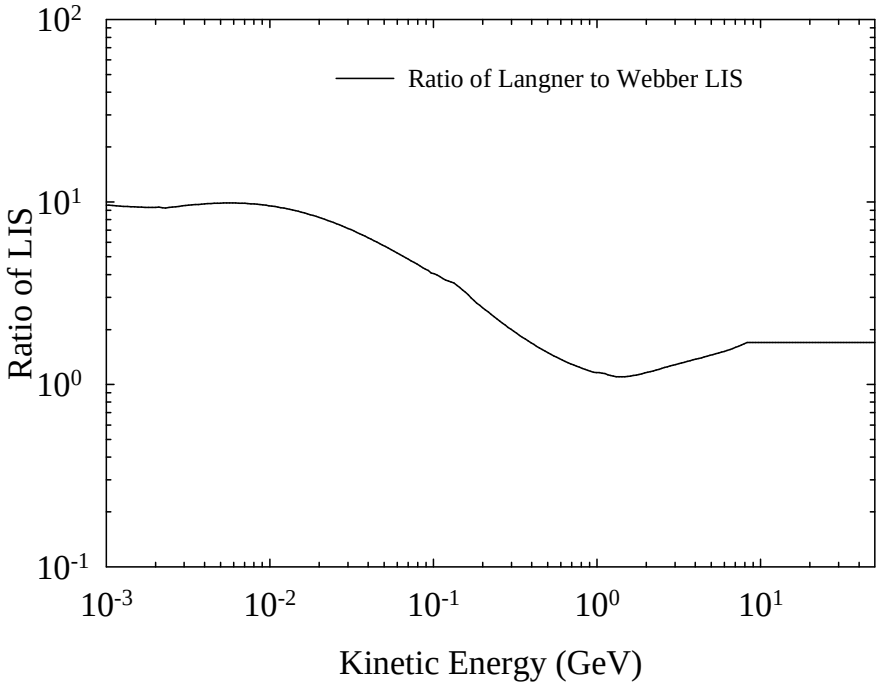

Figure 4.8: Computed ratio between the Langner LIS and the Webber IS-7 as a function of kinetic energy.

At low energies, the almost flat ratio at $E < 10$ MeV implies that the spectral slopes are the same but with the Langner LIS a factor of 10 higher. This is peculiar because both LIS's at these energies are based on radio observations. This illustrates that the computation of these LIS's is still very much biased and subjective. Although the Langner LIS is a factor of 10 higher at low energies, the two LIS's give the same amount of modulation, a consequence of the choice of the rigidity dependence of the heliospheric diffusion coefficients. This will be explored further in the next section.

4.5.2. Computation of modulated spectra in comparison with observations

In this study electron observations from Ulysses taken during 1997 (e.g. Potgieter et al. 1999) when positioned at $r \approx 5$ AU and $\theta \approx 80^{o}$, Evenson's balloon flight of 1983 (Evenson et al. 1983), PAMELA spectra from 2008 (Boezio – private communication; see also Boezio et al. 2011 and reference therein) and Voyager 1 spectra for 2010 (Webber – private communication) are compared to the computed spectra. The first three sets are representative of observations in the inner heliosphere and that from Voyager 1 of the outer heliosphere, when the spacecraft was at ~112 AU. The diffusion coefficients used here are those discussed in section 3.4.

In the top panel of Figure 4.9 the modulated spectra based on the Webber LIS are shown at 1 AU, 5 AU, 60 AU, 90 AU and 110 AU in the equatorial plane. These computed spectra are compared to the mentioned four set of observations as indicated in the figure caption. The bottom panel is similar except that the Langner LIS is used instead.

It should be noted that the Ulysses electron data displayed around ~10 MeV is largely of Jovian origin. Using a full 3D model, similar to the one described in this work, Ferreira (2002), Moeketsi (2004) and Nkosi (2006) illustrated that Jovian electrons completely dominate the electron spectrum in the inner heliosphere below 30 MeV, subsiding with increasing energy so that at 100 MeV an unknown fraction could be attributed to galactic electrons. It is therefore to be expected that the balloon data between 30-80 MeV should contain a Jovian contribution. These issues are one of the aspects studied for this work.

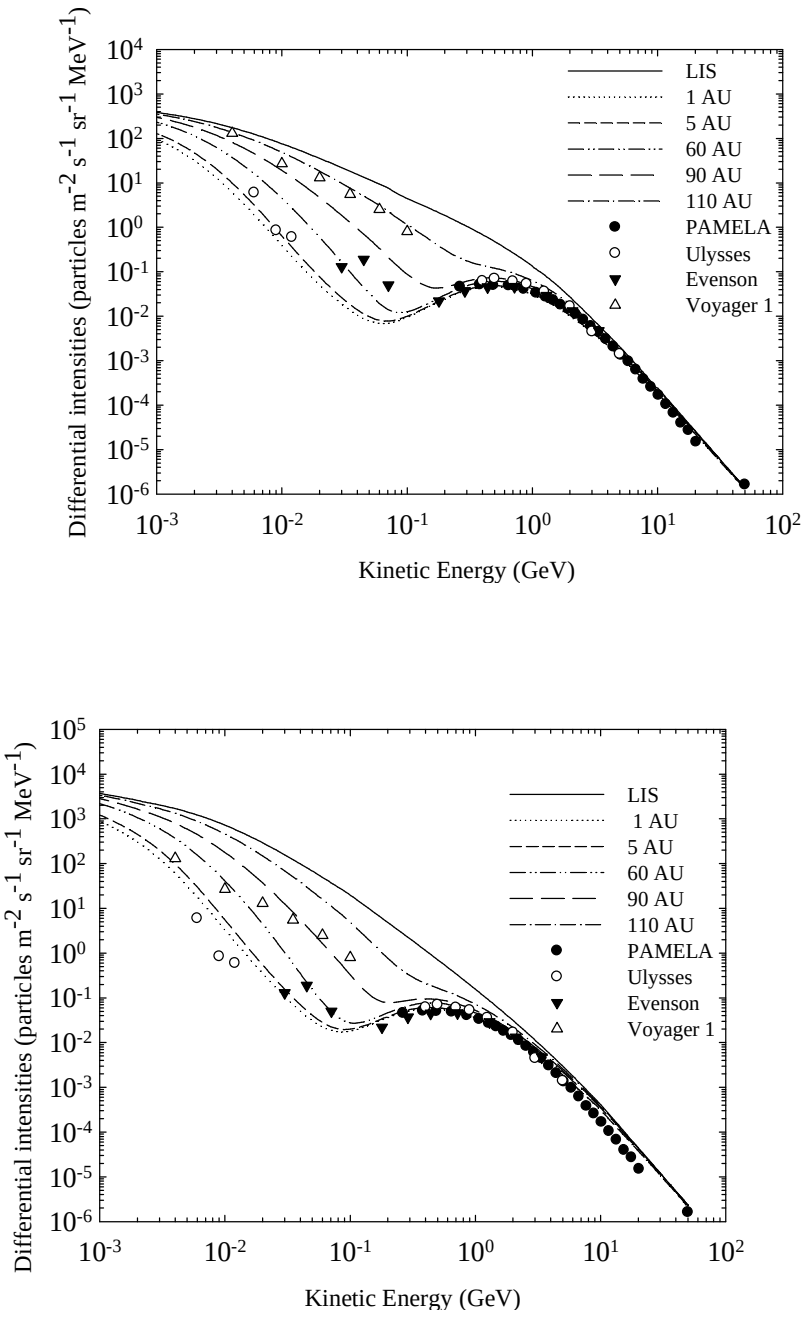

Figure 4.9: Computed spectra at radial distances of 1 AU, 5 AU, 60 AU, 90 AU and 110 AU in the equatorial plane compared with observations. Top panel shows the modulated spectra with the Webber LIS; bottom panel for the Langner LIS. Observations for 2008 (filled circles) are from PAMELA (Boezio, private communication; see also Boezio et al. 2011), for 1997 (open circles) from Ulysses (Potgieter et al. 1999) and for 1983 (filled triangles) from balloon flights by Evenson et al. (1983) and for 2010 (open triangles) from Voyager 1 at 112 AU (Webber, private communication; see also Caballero et al. 2010).

The purpose of Figure 4.9 is to illustrate that when different LIS's are assumed, the spectra above 200-300 MeV observed at and near Earth can easily be reproduced by adjusting the set of modulation parameters as given in chapter 3 in the 3D model.

Unfortunately, because the diffusion coefficients at these energies are not yet known exactly from diffusion theory, one cannot really choose between the two selected LIS's. It appears that the Langner LIS does not agree very well with observations above 10 GeV. In the following chapter, this issue will be addressed and the PAMELA observations will be used to fine-tune the spectral slope with $E > 10$ GeV. Since the model used here does not incorporate Jovian electrons, the compatibility at lower energies is getting poor, as expected.

With the basic applicability of the modeling approach established, the focus can be shifted to how good the compatibility is between the model and the Voyager 1 observations between 6 MeV and 100 MeV at 112 AU. Obviously, the Voyager 1 observations in the outer heliosphere are not contaminated by Jovian electrons.

It follows from the top panel of Figure 4.9, based on the Webber LIS, that the model can reproduce the Voyager 1 observations down to ~ 20-30 MeV but below this energy the Webber LIS seems to decrease too rapidly with decreasing energy, touching the observations below ~10 MeV. This implies that if this LIS was correct, no modulation occurred between 112 AU and the modulation boundary, assumed at 120 AU, which is most unlikely. This situation can be improved from a modeling point of view by either revising the slope and value of the LIS or adjusting the diffusion coefficients at these energies in the outer heliosphere or moving the HP outwards. The latter will cause increased modulation which is in the wrong direction. An additional complication that follows from these results is that the computed galactic electron spectrum at Earth goes through the observational points around 10 MeV which are interpreted as from a Jovian origin. Clearly, the selected diffusion coefficients in the model produce too little modulation near Earth at these energies; the computed spectrum for galactic electrons should be below the Jovian electron data.

In this chapter the focus is on the choice of the LIS, so the first option is to replace the Webber LIS with the higher Langner LIS in order to establish the modulation effects thereof before making significant adjustments to the heliospheric diffusion coefficients. The results are shown in the bottom panel of Figure 4.9. In this case, the model is producing far too little

modulation throughout the heliosphere at E < ~200 MeV, whereas above this energy the model reproduces the observed spectra reasonably.

The conclusions drawn from this modeling exercise are:

- The Webber LIS is too low at E < ~ 80-100 MeV. The Voyager 1 observations suggest that the LIS should be a simple power law at these energies, that is, not decreasing with decreasing energy as both the Webber and Langner LIS are displaying. Developing a new LIS that has the same slope as the Voyager 1 data in the outer heliosphere is the purpose of the work to follow.

- Increasing the Webber LIS at these energies will however produce too high galactic electron intensities in the inner heliosphere, particularly at Earth. This means the diffusion coefficients used so far will have to be adjusted in terms of both their spatial and energy (rigidity) dependence.

4.5.3. Selection of a reasonable electron LIS

As argued above a more appropriate electron LIS at energies below a few hundred MeV, even below 1 GeV, seems to be required. First, a recap of what has been considered so far. Motivated by Voyager 1 observations beyond the TS and some theoretical developments for galactic cosmic ray propagation (Ptuskin et al. 2006), Webber and Higbie (2008) computed at least three new electron LIS's that were different than what they and others used previously. They found without exception the new LIS's lower than anything used before, similar to what Ptuskin et al. (2006) also suggested based on their theoretical input for the GALPROP code. This was in contrast to the Langner et al. (2001) approach despite the fact that almost similar arguments had been used to derive these LIS's, illustrating the controversy around what the electron LIS really is at lower energies.

In Figure 4.10 the two Webber and Higbie (2008) LIS's are plotted, indicated as IS-2.3, IS-7. The IS-2.3 is almost the same as the Langner LIS so if used in the modulation model, it would give qualitatively similar results. In the previous section the Webber IS-7 spectrum was used and it was illustrated that there are unfortunately modifications necessary, as is the case for the Langner LIS which seems too high at these low energies.

Hence, for this study a new LIS is derived, indicated as the RRN LIS in Figure 4.10. This LIS consists of two power law spectra combined; at high energies (E > 10 GeV) where the modulation is supposedly little, the PAMELA electron observations were used to fine-tune the spectral index of the LIS. This part of the spectrum formed the first power law. The Voyager 1 spectrum below 120 MeV was then used to find the second power law. The combination was then matched to produce a reasonable LIS for the middle part of the electron spectrum.

The expression for this RRN LIS is as follows:

If $P <$ 1.0 GV,

$$j_{LIS} = \exp(-2.0 - 1.5110 \ln(T_K)),$$

Where $T_K = (P / P_0) / (1.0 - E_0)$ with E_0 the rest mass of the electron.

if 1.0 GV $\leq P \leq$ 10.0 GV,

$$j_{LIS} = \frac{0.1349 - 6.6\times10^{-3} P + 15.49\times10^{-5} P^2}{1 - 1.3187P + 1.0810P^2 + 0.2327P^3}, \quad (4.6)$$

and

if $P >$ 10.0 GV,

$$j_{LIS} = \exp\left(-0.89 - 3.262 \ln(P)\right).$$

Shown in Figure 4.11 is the computed ratio between the Langner and the RRN LIS together with the ratio between the Webber and the RRN LIS in order to emphasize the differences between them in terms of absolute value and spectral slopes. The computed ratio between the Webber and RRN LIS's becomes less than unity below 100 MeV, thus indicating that the RRN LIS is higher at these energies as seems to be required by the Voyager 1 observations as discussed above. As expected, the differences between the Langner and RRN LIS get large between 1 GeV and about 10 MeV, below which the ratio goes to unity and less as it should because the Langner LIS is too low at these energies.

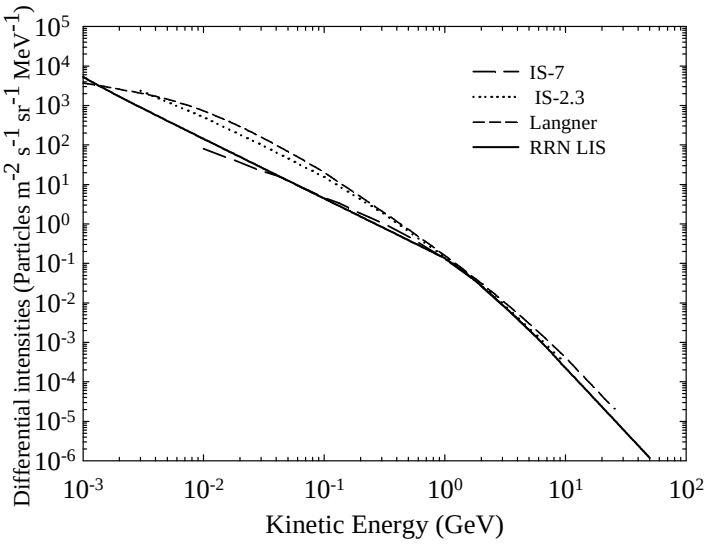

Figure 4.10: Previously computed LIS's compared to a newly derived electron LIS's are shown: long dashed line is for Webber IS-7, dotted line for Webber IS-2.3; short dashed line gives the Langner LIS and the solid line represent the new LIS (indicated as RRN - see Equation (4.6)), based on the research done for this work.

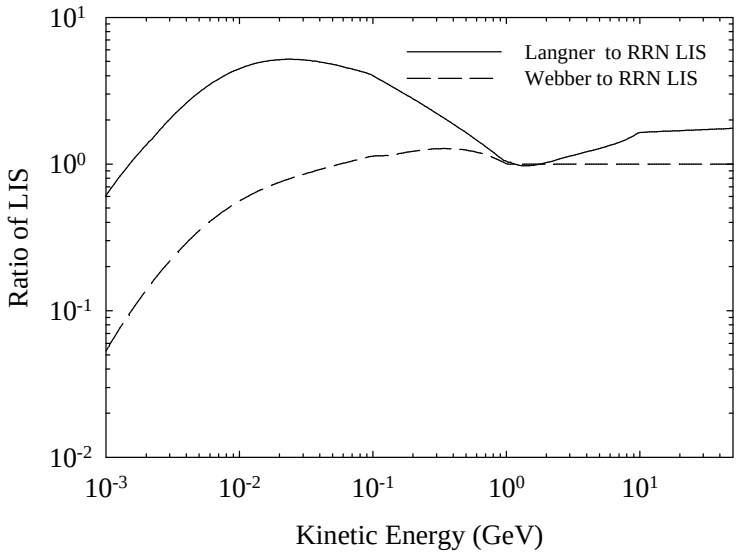

Figure 4.11: Computed ratio of the Langner to the RRN LIS, together with the ratio of the Webber to the RRN LIS as a function of kinetic energy with the solid line giving the Langner to RRN ratio and the dashed line is giving the Webber to RRN LIS ratio. For this calculation, the Webber LIS was extrapolated to 1 MeV.

4.6. Summary and conclusions

This chapter was devoted to finding a new LIS for galactic electrons, which is an important requirement for doing numerical modeling. The LIS has to be specified at the heliospheric modulation boundary as an input spectrum (as an initial condition) to be modulated inside the heliosphere.

First, the nomenclature used to describe galactic spectrum (GS) as a local interstellar spectrum (LIS) or as a very local interstellar spectrum (VLIS) or even as a HP spectrum was critically discussed. This is to make the point that in future cosmic ray modulation studies both experimental and modeling will have to deal with these issues. It is proposed that Voyager 1 is presently observing HP spectra which will later become VLIS once it enters the interstellar region, that is the region undisturbed by the moving heliosphere (perhaps 300-500 AU away from the Sun), not necessarily beyond the HP (see Scherer et al. 2011). The name GS should be reserved for computed GCRs spectra a parsec or so away whereas the LIS should be used for spectra a 1000 AU away. Unfortunately, at this stage the (bad) habit of making no distinction between these names, has to be continued also in this work.

Figure 4.1 showed examples of computed galactic spectra for different cosmic ray species, obtained using the GALPROP model. The focus on this study is on galactic electrons so only galactic electrons were further discussed. Over the years, efforts have been made to determine the GS for electrons using different galactic propagation models. The first calculation was done by Strong et al. (1994), producing the highest GS for electron. This high GS was used as a LIS in earlier studies of galactic electron modulation (e.g. Potgieter 1996). Later, in 2000, Strong argued that this LIS was too high and had to be changed so he computed a much lower spectrum, see Figure 4.2. Also shown was the LIS from Langner et al. (2001) which is between the highest and the middle Strong LIS's. This Langner LIS has been used since its development and is still popular (Ferreira 2002; Moeketsi 2004 and Nkosi 2006).

Over the last decade, significant theoretical modifications were made and a more sophisticated GALPROP model was developed (Ptuskin et al. 2006). They took into consideration additional physical processes in galactic space concerning the diffusion coefficient in the Galaxy, especially its rigidity dependence. After re-examining this they

calculated the primary and secondary GS for different cosmic ray species. Figure 4.3 showed computed electron GS from the GALPROP model for which three different approaches were used, the PD, the DR and the DRD models. The PD and the DR models give too high intensities at low energies, while the DRD model produces a completely different GS with low intensities. The results are the consequence of the choice of the diffusion coefficient utilized in computing GS. Compared to observations the three do reasonably well above 1 GeV. To get the modulated spectra at Earth they used the Force Field modulation model which unfortunately is not valid for electrons at energies below about 1GeV.

Two years later Webber and Higbie (2008), motivated by the new experimental and theoretical developments of Ptuskin et al. (2006) related to both electron propagation in the Galaxy and to the electron spectrum observed in the outer heliosphere by the Voyager spacecraft, calculated new GS below 1-2 GeV for electrons. They used a Monte Carlo Diffusion model for electron propagation in the galaxy and put these GS equal to interstellar spectra. They argued that their calculations were necessary because the GS from Ptuskin et al. (2006) were too high at low energies. This was shown in Figure 4.4. Obviously, there is still a lot of work to be done regarding the galactic diffusion coefficient especially its rigidity dependence.

After showing different computed electron GS as found in the literature, two were selected to compute the modulation of galactic electrons, called the Langner LIS and the Webber IS-7. The results were compared with observations. The effects on electron modulation of using different LIS's with the same set of diffusion coefficients were studied. It is found that the global (qualitative) picture was the same. The tendency of giving too little modulation at low energies in the outer heliosphere was found to be caused by the rigidity dependence of the heliospheric diffusion coefficients that were used.

The comparison with observations was done to establish which LIS would give good compatibility with observations at Earth and in the outer heliosphere, shown in Figure 4.9. Since the 3D model used here does not incorporate the Jovian electrons the compatibility at low energy was expected to be poor. It was also found that the Webber IS-7 had a good agreement with the observations at Earth above 10 GeV, and also agreed very well with the Voyager 1 observations down to ~20-30 MeV. The Langner LIS did not agree very well with the observations above 5 GeV, and also with the Voyager 1 observations in the outer heliosphere.

It was concluded that there was a need to compute a new LIS that would give compatibility to the observations above a few GeV at Earth and at the same time giving compatibility with the Voyager 1 observations at low energies in the outer heliosphere. This LIS was developed together with a set of diffusion coefficient that was different from those used with the Langner LIS and the Webber IS-7 LIS.

The next chapter is devoted to the electron modulation in the heliosheath, utilizing this newly developed LIS and set of diffusion coefficients.

Chapter 5

Modulation of galactic electrons in the heliosheath

5.1. Introduction

Voyager 1 crossed the TS in 2004 and it has been exploring the inner heliosheath since then, with evidence that it might be approaching the heliopause zone, or more controversial, that it has already entered this zone (Krimigis et al. 2011). This is based on the interpretation of the flow speed of very low energy particles at Voyager 1 because the solar wind speed detector has not been working for a long time. This interpretation suggests that the solar wind speed in the radial direction is decreasing relatively fast, implying that the other components are increasing so that Voyager 1 may be close to the region or zone where the solar wind plasma meets the interstellar plasma, the HP. This has not been confirmed, however.

In this chapter the focus is on the modulation of galactic electrons in the inner heliosheath. First, for modeling purposes, the modified expression for the solar wind speed in the inner heliosheath is revisited as well as the corresponding HMF magnitude. The modulated electron spectra and the corresponding radial and polar intensity-profiles are computed. The results obtained are then compared to recent electron observations made by Voyager 1. Lastly, the new HP spectrum for galactic electrons is briefly discussed.

5.2. Solar wind speed and magnetic field profiles in the heliosheath

The approach in finding an expression for the solar wind speed in the inner heliosheath is similar to what Nkosi et al. (2011) used, except here only a stationary TS position is considered. The solar wind speed profile is plotted only along the Voyager 1 trajectory because in this case only these observations are considered. For a review on how the solar

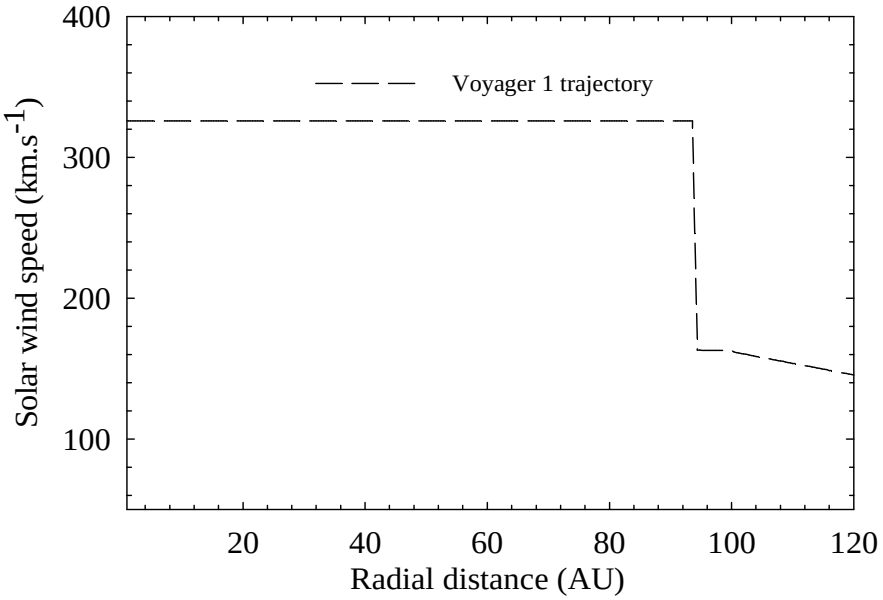

Figure 5.1: Computed solar wind speed as a function of radial distance with the TS located at 94 AU, the position where Voyager 1 crossed it.

wind profile may vary in the heliosheath, see Langner et al. (2006) and Strauss and Potgieter (2010), although the latter focused more on the ACR component.

The radial dependence of the magnitude of the solar wind velocity, from in front of the TS positioned at r_s up to a radial distance of r_{sh} beyond the TS is given by

$$V_r = \frac{V_0(s+1)}{2s} - \frac{V_0(s-1)}{2s}\tanh\left(k\frac{r-r_s}{L}\right), \tag{5.1}$$

where the average value in front of the shock is V_0 = 400 km.s^{-1}. Although the model does not include the process of shock acceleration, a compression ratio of s = 2.5 is included for consistency and in order to describe the transition that is happening across the TS into the heliosheath. Here, L = 1.2 AU, the scale length of the transition. Beyond r_{sh}, V_r is assumed to decrease with distance according to

$$V_r = V_{rh}\left[\frac{r}{r_{sh}}\right]^{a(r)} \tag{5.2}$$

where V_{rh} is the solar wind speed closely upstream $r_{sh} > r > r_s$ of the TS, and $a(r)$ a function determining the profile of V_r further into the heliosheath. For simplicity it is assumed that $a(r) = -2.0$ with the constraint that the divergence of the solar wind velocity is zero inside the inner heliosheath; which gives $(\nabla.\mathbf{V}) = 0$ in Equation (3.1). This means that adiabatic energy changes cannot occur for low energy galactic electrons in the heliosheath beyond a few AU from the TS. See Ngobeni and Potgieter (2010) and also Langner et al. (2006) for a different approach.

Figure 5.1 show how V_r changes as a function of radial distances, computed at $\theta = 60^o$, with the TS located at 94 AU. This is obtained using Equation (5.1) in the modulation model

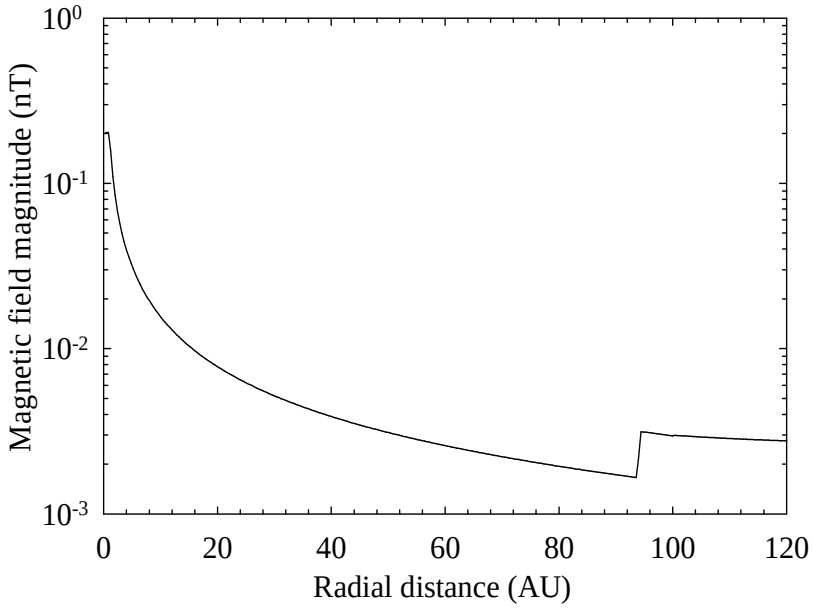

Figure 5.2: The Parker HMF magnitude calculated for the solar wind speed profile in Figure 5.1, shown as a function of radial distance at $\theta = 60°$.

instead of using Equation (2.2) throughout the heliosphere. The figure illustrates how the assumed V_r is changing into the heliosheath, after crossing the TS. Of particular interest is just a few AU beyond the TS where this V_r is decreasing like r^{-2}. Figure 5.2 shows the Parker HMF magnitude as a function of radial distance corresponding to the solar wind speed profile shown in Figure 5.1. Correspondingly, the HMF magnitude decreases as $B \sim (rV)^{-1}$ into the heliosheath.

5.3. Modeling results

5.3.1. Electron spectra

Shown in Figures 5.3 and 5.4 are electron spectra at 90 AU and 110 AU computed with θ = 10°, θ = 60° and θ = 90°, respectively, for the A < 0 magnetic polarity epoch with a tilt angle α = 5° assuming full drifts. The solar cycle related changes due to drifts are not further explored because the focus is on the low energy (6-100 MeV) galactic electrons where drifts are insignificant as shown in chapter 3. At higher energies, drifts cannot be neglected (see also Potgieter 1996).

The interesting fact about studying the low energy electrons is that they respond directly to the energy dependence of the diffusion coefficients as oppose to protons which experience large adiabatic energy losses at low energies (Potgieter 1996, 2000). The diffusion coefficients used for these computations are those discussed in section 3.9. Only the 90 AU and the 110 AU modulated spectra are shown because the emphasis is on electron modulation

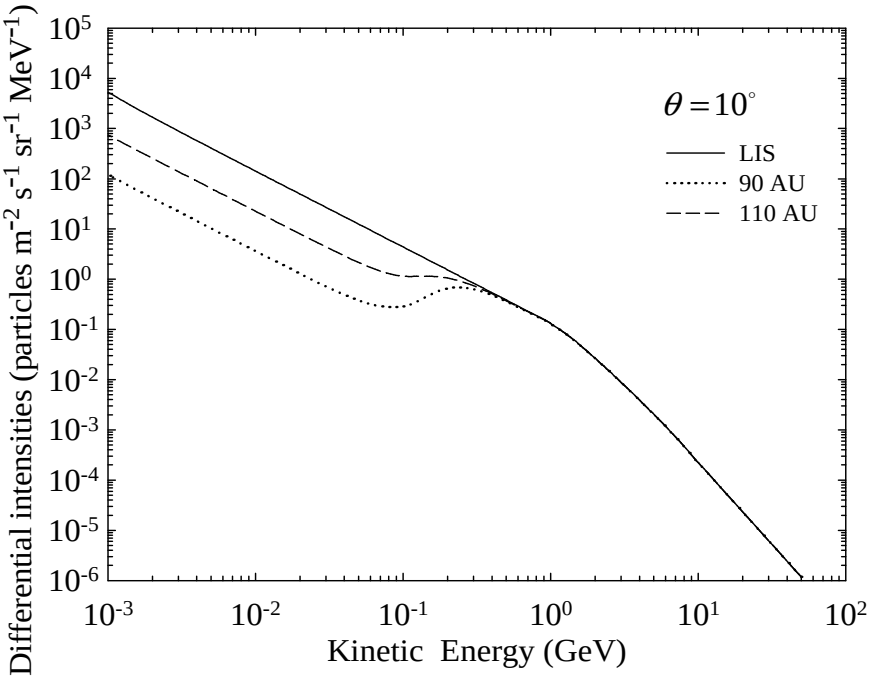

Figure 5.3: Computed electron spectra at θ = 10° and at 90 AU and 110 AU in the heliosheath, with respect to the LIS at 120 AU, as a function of kinetic energy for the A < 0 HMF polarity epoch.

in the heliosheath. The computations are shown at different polar angles to illustrate the differences in modulation, especially below 100 MeV, from the heliospheric equatorial plane ($\theta = 90^o$) to the poles.

Figure 5.3 shows computed electron spectra at 90 AU and 110 AU with $\theta = 10°$ (close to the heliospheric pole) and with respect to the RRN LIS discussed in the previous chapter. Above 300 MeV the spectra are indistinguishable from the LIS showing that there is little modulation above these energies in the polar regions of the heliosheath. This changes rapidly below 300 MeV but below 50 MeV the amount of modulation (difference between the LIS and the modulated spectra) becomes constant with the modulated spectra having the same slope (spectral index) as the LIS down to 1 MeV.

This steady modulation is the consequence of the rigidity dependence of the diffusion coefficients that is constant below $P \leq 0.4$ GV, but increases above $P > 0.4$ GV. This rigidity dependence was shown and discussed in section 3.9. As explained in this section, the choice of using this rigidity dependence of the diffusion coefficients is based on turbulence theory as developed for the inner heliosphere, assuming to be applicable also to the outer heliosphere. This will be tested further below.

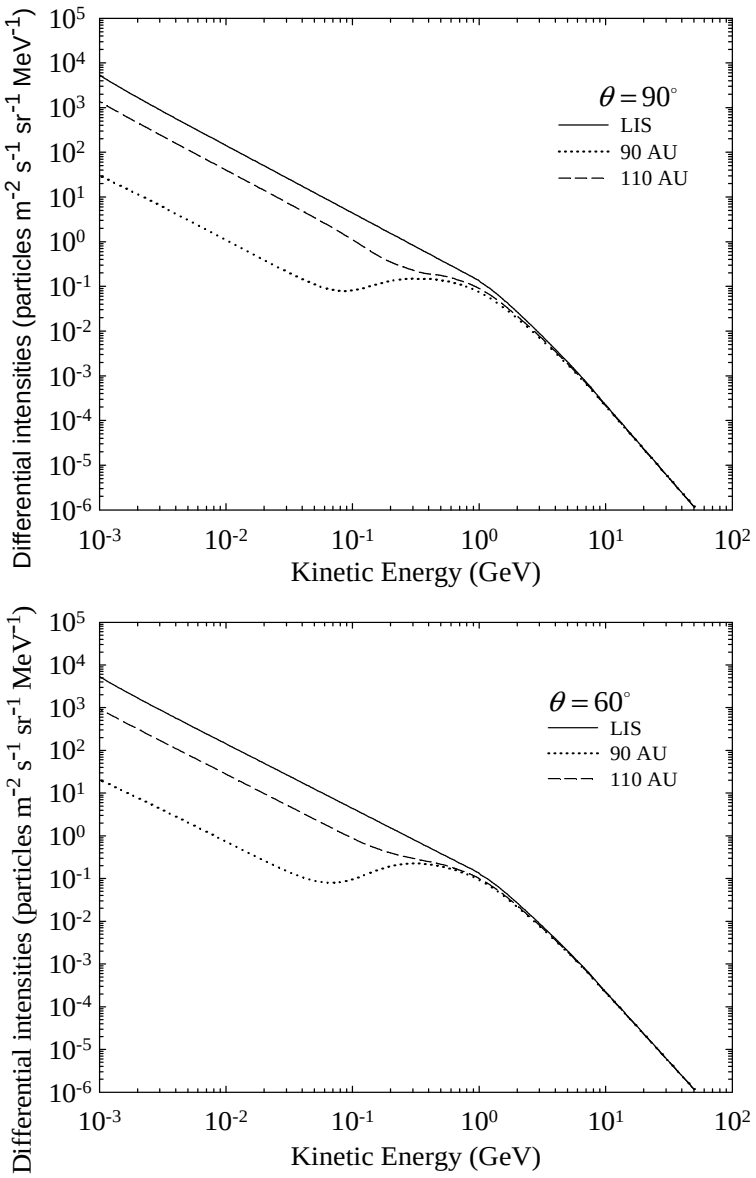

Figure 5.4: Computed electron spectra for 90 AU and 110 AU for the A < 0 HMF polarity epoch computed at θ = 90° (top panel) and θ = 60° (bottom panel) with respect to the LIS at 120 AU as a function of kinetic energy.

The bottom panel of Figure 5.4 shows the computed spectra at 90 AU and 110 AU, now at θ = 60°. This case is of special interest because this is the approximated heliolatitude of the Voyager 1 trajectory. Evidently, the modulation now starts at a higher rigidity, at ~2 GeV, but with little difference between the 90 AU and 110 AU modulated spectra from 2 GeV to 500 MeV. The top panel of Figure 5.4 shows the situation at θ = 90°, the equatorial plane. The 110 AU spectrum at 1 MeV gives somewhat less modulation than at θ =10°. The

intensities at 1 MeV is just above 10^3 particles m^2 s^{-1} sr^{-1} MeV^{-1}, whereas for θ = 60° and θ =10° the intensities are ~930 particles m^{-2} $s^{-1}sr^{-1}MeV^{-1}$ and 800 particles m^{-2} s^{-1} sr^{-1} MeV^{-1} respectively. The situation at 90 AU is different, for the computed spectra $\theta = 10^o$ shows the least modulation with respect to the LIS, followed by the $\theta = 90^o$ and then $\theta = 60^o$. This implies that the latitudinal intensity gradient is quite unusual between these latitudes and is therefore discussed further below.

5.3.2. Polar dependence of 12 MeV electron intensities

Shown in top panel of Figure 5.5 is the polar dependence of 12 MeV electron intensities computed at 90 AU. The shape that is depicted in the figure illustrates the unusual latitudinal dependence of electrons at this energy deep into the heliosheath. Maximum intensities are obtained at the poles, with minimum intensities obtained near θ ~ 50° and θ ~ 130° respectively. The polar intensity gradients therefore become zero at these polar angles. This also happens in the equatorial plane but here simply because of the assumed boundary condition in the model. In contrast, quite a large polar dependence is found near the poles of the heliosphere, with large polar intensity gradients.

The bottom panel is similar but now results are shown at 110 AU. Again an unusual shape is found, but now the highest intensities at the poles are almost matched at the equatorial plane. The maximum intensity is ~ 31 particles m^{-2} s^{-1} sr^{-1} MeV^{-1} at 0° and at 180° and the minimum is ~ 12 particles m^{-2} s^{-1} sr^{-1} MeV^{-1} intensity at θ ~ 30° and θ ~ 130°. The minimum intensities at this distance are the maximum for 90 AU.

The global picture shown here is that inside the heliosheath, a large latitudinal dependence is found for 12 MeV electron intensities.

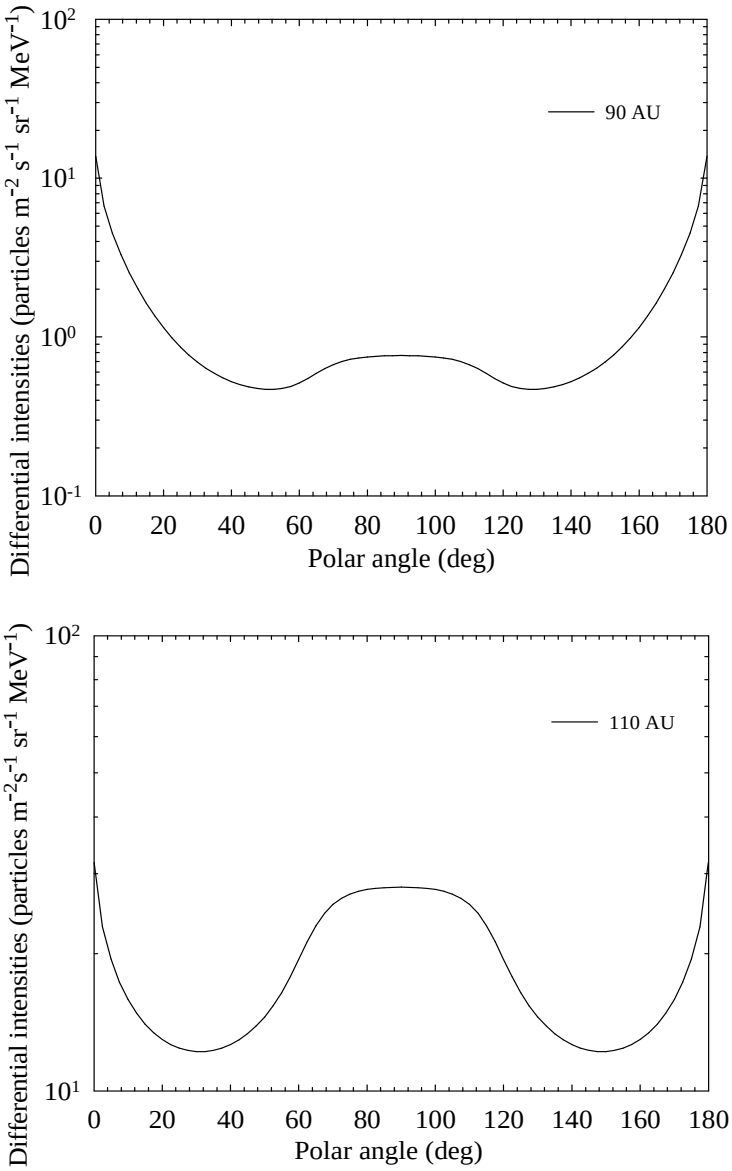

Figure 5.5: Computed 12 MeV electron differential intensities as a function of polar angle at radial distance of 90 AU and 110 AU respectively. Note the different scales for the intensities.

5.3.3. Radial dependence of 12 MeV electron intensities

Figure 5.6 shows computed differential intensities for 12 MeV electrons as a function of radial distance between 70 AU to 120 AU, with θ = 10°, θ = 60° and θ = 90° respectively. These computations are based on the modeling as reported by Ferreira (2002), Moeketsi (2004) and Nkosi (2006) using the Langner LIS.

The diffusion coefficients used for these computations are given by Equations (3.30), (3.31) and (3.33). Evidently, the intensities at the three polar angles differ insignificantly. But, it follows that a strong radial dependence is found for this outer part of the heliosphere up to the heliospheric boundary (HP). However, this steady radial dependence, with relatively high intensities, cannot reproduce the 6-14 MeV electron intensities as observed in the heliosheath by Voyager 1. The computation is therefore repeated using the RRN LIS, shown in Figure 5.7. The other modulation parameters and diffusion coefficients used for this figure were given in section 3.9. In this case, the radial dependence is clearly different from the previous figure. The tendency is to give a flatter radial dependence between 70 AU and 90 AU, different for the three polar angles. Beyond 110 AU, the difference in intensities between the three polar angles subsides.

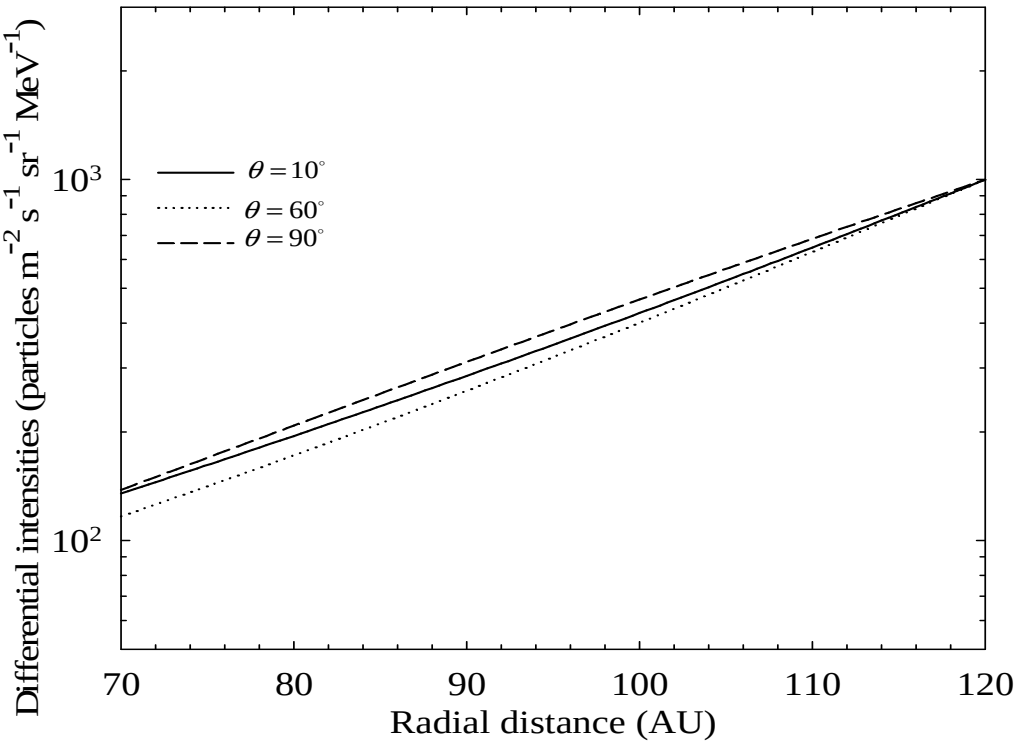

Figure 5.6: Radial dependence of 12 MeV electron intensities computed at three different polar angles: θ = 10° (the solid line), θ = 60° (dotted line) and θ = 90° (dashed line) based on the modeling done by Moeketsi (2004) and Nkosi (2006).

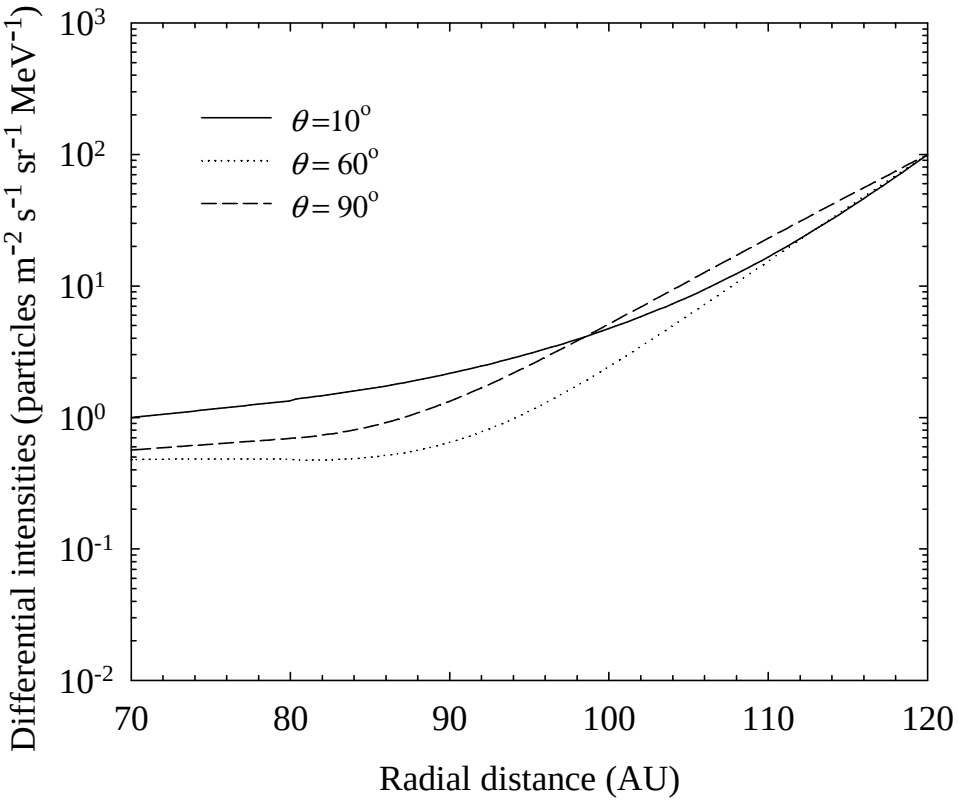

Figure 5.7: Similar to Figure 5.6 but based on the RRN LIS. In this case the diffusion coefficients discussed in section 3.9 were used.

Figure 5.8 shows two radial intensity profiles for 12 MeV electrons with θ = 60°. The first case is with V_r constant (independent of radial distance) and the second with V_r not constant (dependent on radial distance). In particular, the solid line is computed with the solar wind expression given by Equation (2.2) and the dotted line with Equation (5.1) in the 3D model.

The reason for using the different solar wind expressions was to establish what happens in the heliosheath if the solar wind velocity is divergence free so that no adiabatic energy changes occur in the heliosheath. From the figure follows that the global picture is similar, only relatively small quantitative changes occur: between 70 AU and 80 AU the two profiles are identical but between 80 AU and ~ 94 AU the non-constant V_r profile shows a weaker radial dependence than with a constant V_r. Beyond 94 AU the non-constant V_r is showing a somewhat stronger radial dependence. The overall conclusion that can be made from Figure 5.8 is that changing the solar wind expression inside the heliosheath only changes the modeling results quantitatively but not qualitatively.

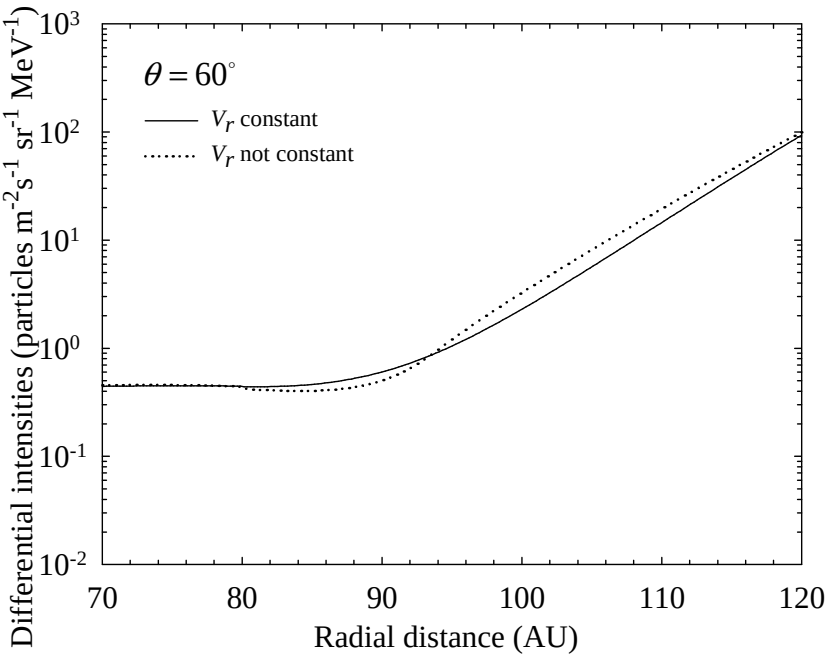

Figure 5.8: Computed 12 MeV electron differential intensities as a function of radial distance at θ = 60°. The solid line is the computation with the solar wind speed given by Equation (2.2) whereas the dotted line is given by Equation (5.1).

5.3.4 Comparison with Voyager 1 electron observations

Computed spectra at 90 AU and 110 AU together with the RRN LIS are shown in Figure 5.9. These spectra are compared with Voyager 1 observations when it was at 112 AU (Webber, private communication, see also Caballero et al. 2010). This shows that the new LIS, used together with appropriate diffusion coefficients, does in fact produce a modulated spectrum that compares well with observations. This is an improvement compared to what was shown in chapter 4 using the Langner LIS and Webber IS-7.

Figure 5.10 shows the computed radial dependence of 12 MeV electron intensities compared to the 6-14 MeV electron intensities as observed by Voyager 1 (Webber, private communication) between 70 AU up to 112 AU. The two computed profiles are from Figure 5.8. The compatibility between the two computed profiles and the observations are good, except that beyond 100 AU the V_r not-constant-approach seems too high.

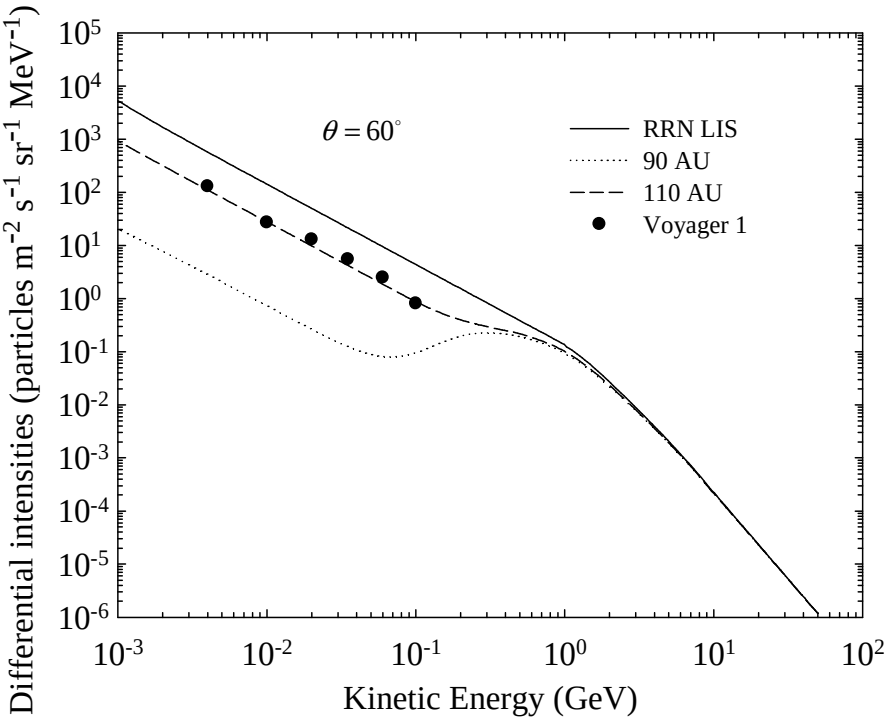

Figure 5.9: Computed electron spectra at 90 AU and 110 AU, obtained by using the RRN LIS at 120 AU, compared with Voyager 1 observations at 112 AU in 2010 (Webber, private communication). The spectra are computed with θ = 60°, resembling the Voyager 1 trajectory.

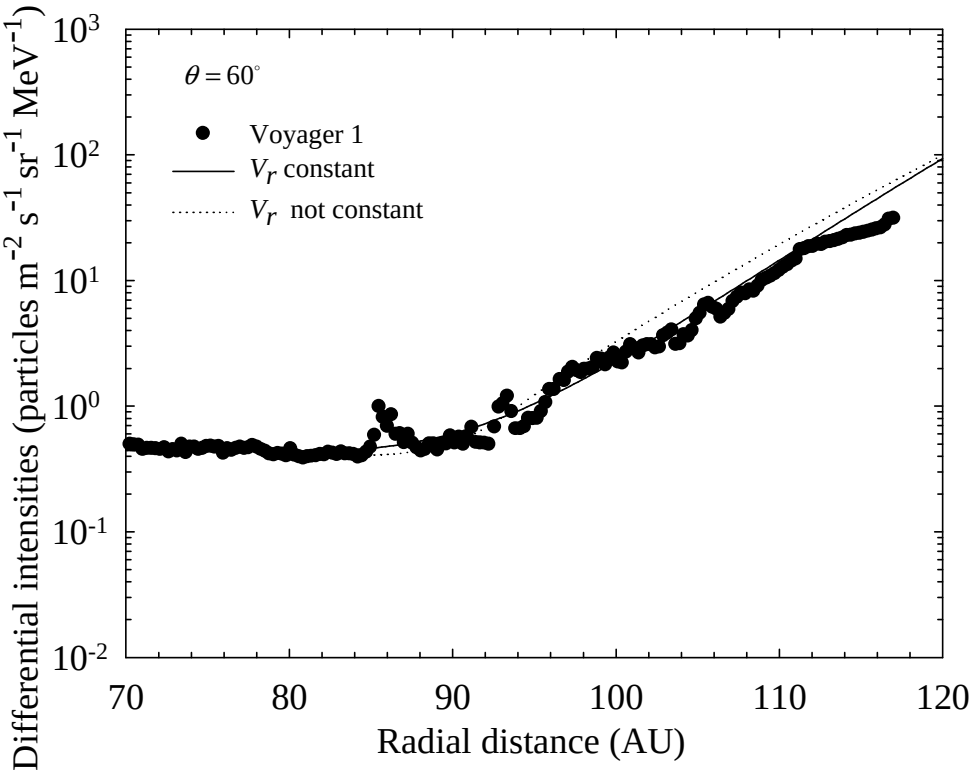

Figure 5.10: Computed intensities for 12 MeV electrons as a function of radial distance compared to Voyager 1 electron observations at 6-14 MeV (Webber, private communication)**.**

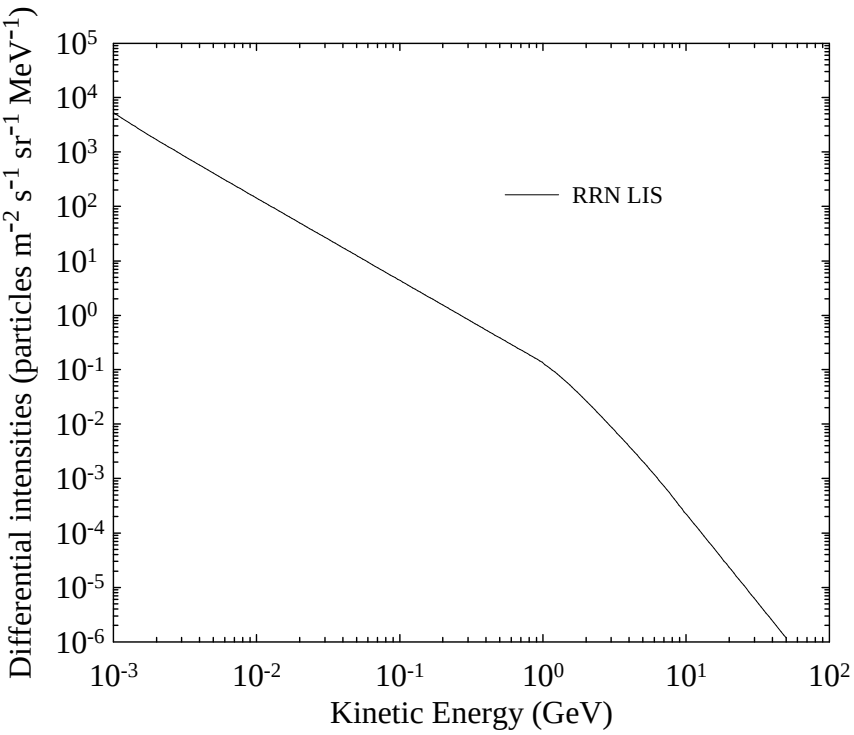

Figure 5.11: Newly computed RRN LIS for galactic electrons.

The Voyager 1 observations shown in Figures 5.9 and 5.10 are up to 112 AU which means that it is probably close to the HP zone. The electron spectrum observed by Voyager 1 can thus be called the HP spectrum for galactic electrons. A result of this work is that the RRN LIS (Equation 4.6) is presented as the VLIS, somewhat higher than the HP spectrum. To recap, this spectrum is shown again in Figure 5.11, clearly illustrating that it consists of two power laws, with a break around 1 GeV. For higher rigidities, PAMELA electron observations were used to adjust the spectral slope whereas for the lower part the Voyager 1 observations were used when it was at 112 AU. The combination was smoothed to produce what seems also a reasonable LIS for the middle part of the electron spectrum.

5.4. Summary and conclusions

This chapter focused on the modeling of 12 MeV galactic electrons in the heliosheath, making use of a new LIS and a set of appropriate diffusion coefficients. The spectra were computed at 90 AU and 110 AU for polar angles of θ =10°, θ = 60°, and θ = 90° to establish how different the modulation could be; shown in Figures 5.3 and 5.4.

The polar dependence of the electron intensities was also computed for 90 AU and 110 AU and a strong latitudinal dependence was found, probably applicable to the whole heliosheath.

The radial dependence of the electron intensities was then computed, again at θ = 10°, θ = 60°, and θ = 90°. This was compared to computations done previously by the local research group e.g. Ferreira (2002), Moeketsi (2004) and Nkosi (2006). It was found that these attempts did not resemble the recent Voyager 1 observations well and was therefore modified, using a new LIS and a new set of diffusion coefficients, fine-tuned for the heliosheath. The results were shown in Figure 5.9 and 5.10. A complete radial profile from 1 AU up to the HP will be shown in the next chapter.

It was thus necessary to use a new LIS that preserves the spectral slope of $E^{-1.5}$ what the electron observations inside the heliosheath have suggested, since it crossed the TS. This LIS is seen as an improvement of the Webber IS-7 and the Langner LIS.

Chapter 6

Modulation of galactic electrons from the inner to the outer heliosphere

6.1. Introduction

In this chapter the modulation of galactic electrons from the inner to the outer heliosphere is investigated. This includes modulation aspects ranging from the computed spectra at Earth and at different radial distances to intensity gradients, both radial and polar, focusing on low energy galactic electrons. This is done using the new LIS developed for this study and in comparison with observations from Voyager 1. As an outcome of this computational study, predictions are made about the intensity that galactic electrons could have in the inner heliosphere, up to Earth.

6.2. Radial and latitudinal cosmic ray gradients

The study of GCRs intensity gradients has always been a topic of interest, now even more with Voyager 1 far out in the heliosheath and approaching the outer modulation boundary of the heliosphere. The gradients that Voyager 1 has observed in the heliosheath are most relevant and can be used to predict the value of the LIS, especially at energies $E < 100$ MeV that is difficult to obtain from galactic propagation models (Moskalenko et al. 2006). Webber and Higbie (2008) reported that large radial gradients, in a range between 10-20 % AU^{-1} could be expected to be measured by Voyager 1. This aspect is studied further. Concerning cosmic ray latitudinal gradients, Ulysses observed very small gradients, less than 1% per deg in the inner heliosphere, see Heber and Potgieter (2006) for a review.

In this study the radial and polar gradients are computed for different energy bins, as a function of radial distance and polar angles. This is done along the Voyager 1 trajectory as the main interest.

Electron intensities as a function of radial distance are computed to determine by what percentage low-energy intensities have increased in the outer heliosphere as compared to the inner heliosphere. It should be noted that calculations of these gradients based on observed intensities, are called non-local gradients, in contrast to local gradients that are calculated directly from computed spectra at different radial distances and polar angles. In this study only local gradients are computed. (See also the discussion on gradients by Nkosi et al. 2008 and Ngobeni and Potgieter 2010).

The cosmic ray intensity gradients in the heliosphere are the consequence of the combination of all four modulation processes. The modulation model generates an omni-directional distribution function, *f*, throughout the heliosphere, that is, as a function of three spatial coordinates and rigidity (or energy). To obtain quantities that are equivalent to those measured by cosmic rays detectors, the distribution function is expressed as a function of differential intensity

$$j \propto P^2 f, \tag{6.1}$$

The total local vector gradient in the heliosphere in three dimensions is mathematically defined in heliocentric spherical coordinates as

$$\mathbf{g} = \frac{1}{f}\frac{\partial f}{\partial r}\mathbf{e}_r + \frac{1}{rf}\frac{\partial f}{\partial \theta}\mathbf{e}_\theta + \frac{1}{r\sin\theta f}\frac{\partial f}{\partial \phi}\mathbf{e}_\phi = \frac{1}{j}\frac{\partial j}{\partial r}\mathbf{e}_r + \frac{1}{rj}\frac{\partial j}{\partial \theta}\mathbf{e}_\theta + \frac{1}{r\sin\theta j}\frac{\partial j}{\partial \phi}\mathbf{e}_\phi, \tag{6.2}$$

with the local radial gradient

$$g_r = \frac{1}{f}\frac{\partial f}{\partial r} = \frac{\partial \ln f}{\partial r} = \frac{\partial \ln j}{\partial r}, \tag{6.3}$$

and the local polar gradient

$$g_\theta = \frac{1}{rf}\frac{\partial f}{\partial \theta} = \frac{1}{rj}\frac{\partial j}{\partial \theta}. \tag{6.4}$$

The units in this case are expressed in % $AU^{-1}deg^{-1}$. The latitudinal gradient g_λ is related to the polar gradient g_θ as follows

$$g_\lambda = r g_\theta = \frac{1}{f}\frac{\partial f}{\partial \theta} = \frac{\partial \ln f}{\partial \theta}. \tag{6.5}$$

The units are then simply in % deg^{-1}. Next only radial and polar gradients are computed.

6.2.1. Electron radial gradients

The local radial gradient, in terms of a computational model, is determined by the size of the spatial (numerical) grid. In correspondence with Equation (6.3), it is then computed as the variation of the differential intensity, with $J = j$ with a variation in radial distance Δr. The equation for the computed local radial gradient is then given by

$$G_r = \frac{1}{J}\frac{\Delta J}{\Delta r}, \tag{6.6}$$

and is expressed in % AU^{-1}. It can be computed with a numerical model throughout the heliosphere at different energies, with the precision and accuracy determined by the spatial grid size used in the numerical model $(\Delta r \to 0 \Rightarrow G_r \to g_r)$.

From observations far apart in the heliosphere only a non-local gradient can be calculated for a particular energy; with $r_2 \gg r_1$ and with the corresponding intensities J_2 and J_1, the non-local radial gradient is

$$G_r^* = \frac{\Delta \ln J}{\Delta r} = \frac{\ln\left(J_2 / J_1\right)}{r_2 - r_1} = \frac{\ln\left(f_2 / f_1\right)}{r_2 - r_1}. \tag{6.7}$$

For further information on these gradients, see Potgieter et al. (1989), Nkosi (2006) and Ngobeni and Potgieter (2010). For reports on observational radial gradients from IMP8, Voyager 1 and 2 and Ulysses, see e.g. Heber et al. (1993), Fujii and McDonald (1999, 2001), Webber and Lockwood (2004) and Heber and Potgieter (2006).

6.2.1.1. Energy dependence

Shown in Figure 6.1 is G_r, computed as a function of kinetic energy at 1 AU, 5 AU, 60 AU, 90 AU and 110 AU, with θ = 10°and θ = 60° respectively.

The top panel shows G_r with θ = 10°. For all radial distances, it is increasing with decreasing energy. A larger G_r is thus always obtained at lower energies. At 1 AU, the highest value is: G_r ~ 18.2 % AU^{-1} at 1 MeV, then decreasing sharply between 20 MeV and 100 MeV, makes a turnaround at 100 MeV to increase between 100 MeV and 1 GeV, then decreases sharply to remain unchanged above 1 GeV. At 1 AU, and below 200 MeV, G_r also has the largest value compared to other radial distances. At 5 AU, G_r is mostly larger than at 60 AU and 90 AU. At 60 AU, G_r is the smallest and remains constant below 100 MeV, then decreases and approaches zero above 10 GeV. At 90 AU, G_r remains constant below 100 MeV and decreases sharply between 100 MeV and 1 GeV and approaches zero above 1 GeV. At 110 AU, G_r is the second largest giving ~ 15.9 % AU^{-1}, at 1 MeV and maintains that value until it reaches 60 MeV where it decreases sharply to approach zero already at 1 GeV indicating that G_r becomes independent of energy in the polar regions of the heliosheath at lower energies than in the rest of the heliosphere.

The bottom panel shows G_r with θ = 60°. Here, unlike at θ = 10°, G_r ~ 18.3 % AU^{-1} is the highest at 1 MeV at 110 AU. It maintains constant at ~17.5 % AU^{-1} below 100 MeV then decreases sharply to flatten off to zero above 10 GeV. At 90 AU, G_r is larger than at 1 AU and 5 AU below ~100 MeV, and larger than at 60 AU below 200 MeV; it approaches zero above 200 MeV. At 60 AU, G_r ~ 1 % AU^{-1} is the smallest for almost all energies and go to zero above 5 GeV. At 1 AU, G_r is almost the same as for 90 AU below 10 MeV to become the largest value above 500 MeV.

It follows from computing G_r at these different polar angles and radial distances how its energy dependence changes (sometimes quite peculiar) from the inner to the outer heliosphere. The computed values in Figure 6.1 show that G_r could range from as large as 20% AU^{-1} to almost zero with increasing energy. Of course, at energies above 10 GeV, the gradients will approach zero as the modulation subsides. For this model it is assumed that modulation does not occur above 30 GeV.

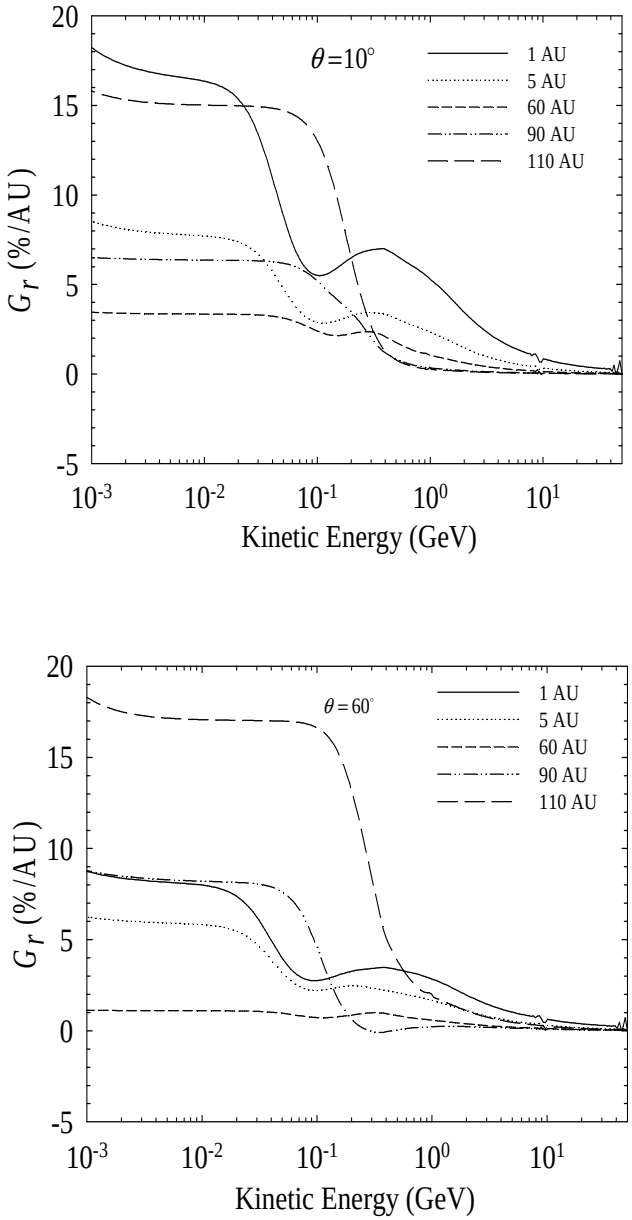

Figure 6.1: Computed radial gradient G_r at 1 AU, 5 AU, 60 AU, 90 AU and 110 AU as a function of kinetic energy shown at θ = 10° (top panel), θ = 60° (bottom panel) for an A < 0 solar magnetic polarity epoch.

Also not explored for this work is how the gradients change with the solar cycle and when the polarity of the HMF is switched because this is relatively well-known - see Potgieter (1996), Ferreira et al. (2003), Moeketsi (2004), Ngobeni and Potgieter (2010).

6.2.1.2. Radial dependence

The radial dependence of G_r for 12 MeV galactic electrons are computed with θ = 10°, θ = 60° and θ = 90° respectively. The top panel of Figure 6.2 shows this radial dependence with θ = 10°, producing at r ~ 1 AU quite a large value, G_r ~ 15 % AU^{-1}, decreasing sharply over the first ~10 AU to remain small and almost constant up to the heliosheath. Beyond 80 AU, G_r increases significantly to its maximum value of ~23 % AU^{-1} at 120 AU.

The middle panel is similar but with θ = 60°. At r ~ 1 AU, G_r is now almost a factor of 2 smaller than obtained with θ = 10°, yielding an increase up to r ~ 5 AU, but then decreases until r = 80 AU. Beyond 80 AU it increases sharply with a maximum of G_r ~ 24 % AU^{-1} at 120 AU. At these polar angles, the overall tendency is that G_r is relatively small in most of the inner to middle heliosphere with a relatively weak radial dependence but the outer heliosphere shows larger radial gradients with a strong radial dependence. This is of course expected because the diffusion coefficients are significantly reduced in this region; see Figure (3.16).

The bottom panel is similar but with θ = 90°. The tendencies discussed above are now more enhanced. With r < ~4 AU, a relatively large G_r is produced with a stronger radial dependence, decreasing sharply from G_r ~ 20 % AU^{-1} at ~1 AU to G_r ~ 5 % AU^{-1} at ~4 AU where it turns to decrease rapidly for the rest of the inner heliosphere giving G_r < 5 % AU^{-1} between 20 AU and 60 AU to become even smaller between 60 AU and 80 AU with G_r < 1 % AU^{-1}. However, beyond r ~ 80 AU, G_r increases sharply to reach a maximum around 100 AU to then decrease moderately up to 120 AU. A much stronger radial dependence is thus obtained in the outer heliosphere, as is required to reproduce the Voyager 1 observations.

Although the computations differ quantitatively at different polar angles, the global (qualitative) picture is not that much different. It depicts large changes in the innermost heliosphere with a relatively small radial dependence from the inner to the middle heliosphere to become significantly larger in the outer heliosphere, reaching a maximum close to the HP as modulation boundary.

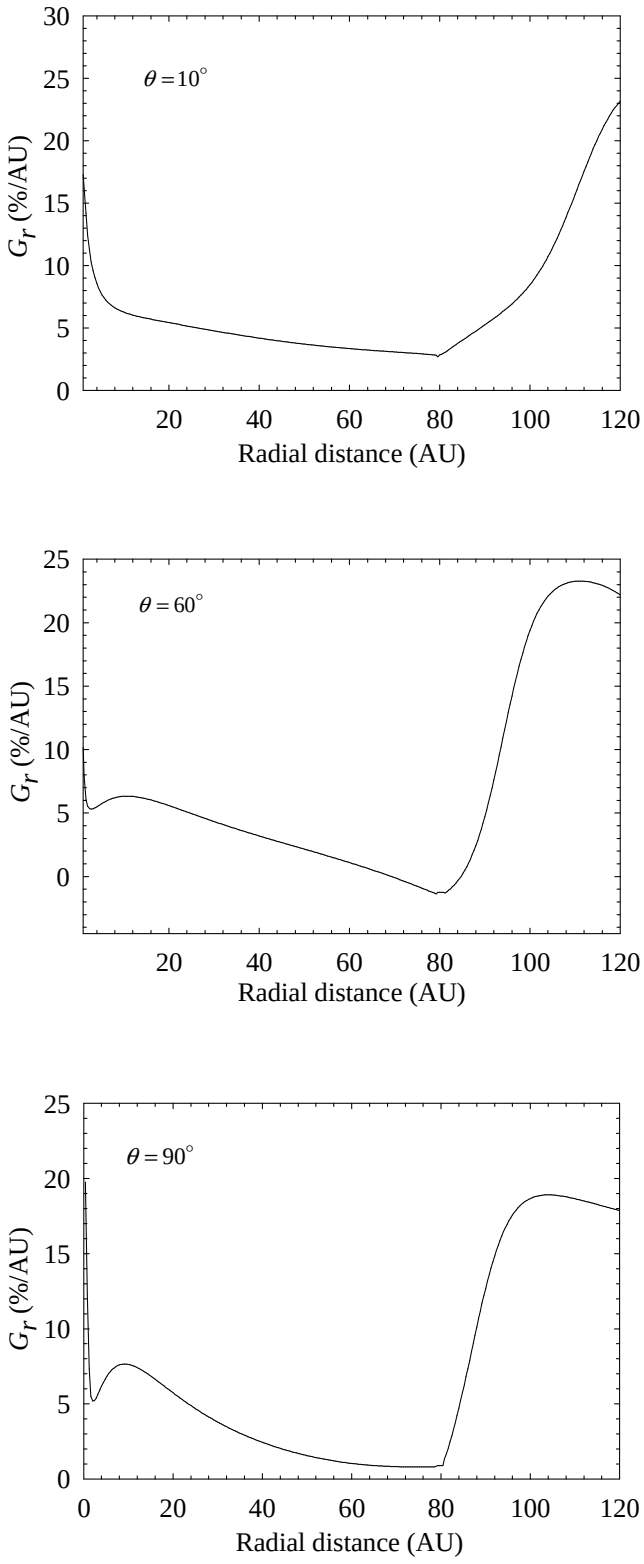

Figure 6.2: Computed radial dependence of G_r shown at θ = 10° (top panel), θ = 60° (middle panel) and θ = 90° (bottom panel).

6.2.2. Electron polar gradients

The polar gradients are also expressed as local or non-local gradients. Similar to the radial gradients, the local polar gradient G_θ at a given radial distance r is given by

$$G_\theta = \frac{1}{rJ}\frac{\Delta J}{\Delta \theta}, \tag{6.8}$$

and is expressed in units of % $AU^{-1}deg^{-1}$.

The non-local polar gradient at a given radial distance between polar angles $\theta_2 > \theta_1$ is given by

$$G_\theta^* = \frac{1}{r}\frac{\Delta \ln J}{\theta} = \frac{1}{r}\frac{\ln\left(J_2 / J_1\right)}{\theta_2 - \theta_1}. \tag{6.9}$$

Usually the calculated latitudinal gradient G_λ based on observations is given in terms of heliolatitude (not polar angle) and is related to G_θ by

$$G_\lambda = rG_\theta. \tag{6.10}$$

and is expressed in units of % deg^{-1}.

It is known that the HMF has two different polarity cycles called the A > 0 and the A < 0 where negatively charged particles drift differently depending on which cycle it is. During A < 0 polarity cycle negatively charged particles drift from the poles inward and outward along the HCS. Their intensities are higher at the poles than in the equatorial plane, causing a negative G_θ as a function of polar angle.

6.2.2.1. Energy dependence

Figure 6.3 displays the computed G_θ for galactic electrons at 1 AU as a function of kinetic energy with θ =10°. Evidently, it has small absolute values with a peculiar energy dependence around 100 MeV. Figure 6.4 shows the computed G_θ at 1 AU as a function of kinetic energy with θ = 60°. The absolute values are larger than at θ =10°.

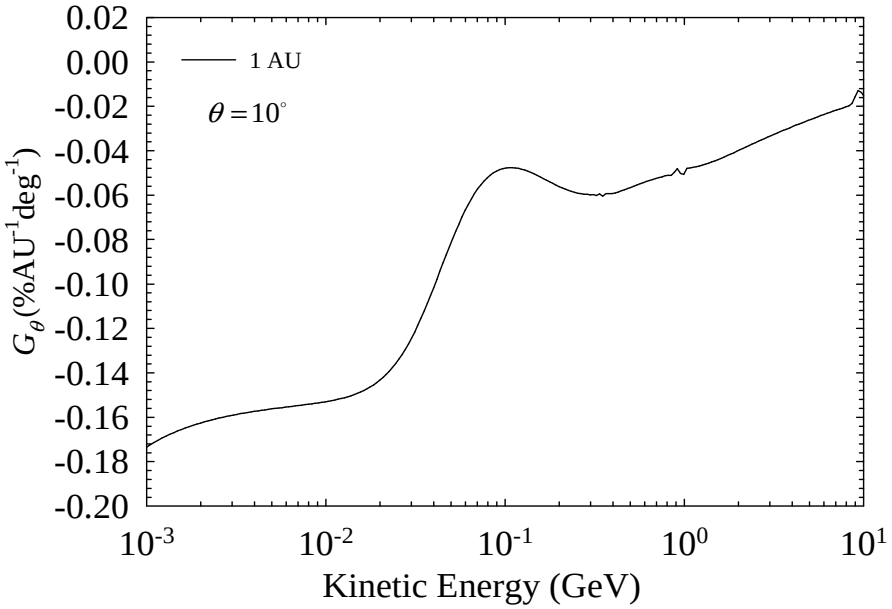

Figure 6.3: Computed G_θ as a function of kinetic energy at 1 AU with θ = 10° for the A < 0 magnetic polarity epoch.

Comparing Figures 6.3 and 6.4 shows that energy dependence is the same, caused by the fact that $K_{\perp\theta}$ has the same rigidity dependence as $K_{||}$ from Equation (3.33). It turns out that these polar gradients are quite small, less than 1% even at Earth. The gradients at other radial distances are not shown because they are even smaller than the ones shown here. This is caused by enhancing $K_{\perp\theta}$ with polar angle (see Equation 3.46) which in the outer heliosphere is quite large. Its modulation effect is to suppress drifts, hence giving small latitudinal gradients throughout the heliosphere. See also Potgieter (1996).

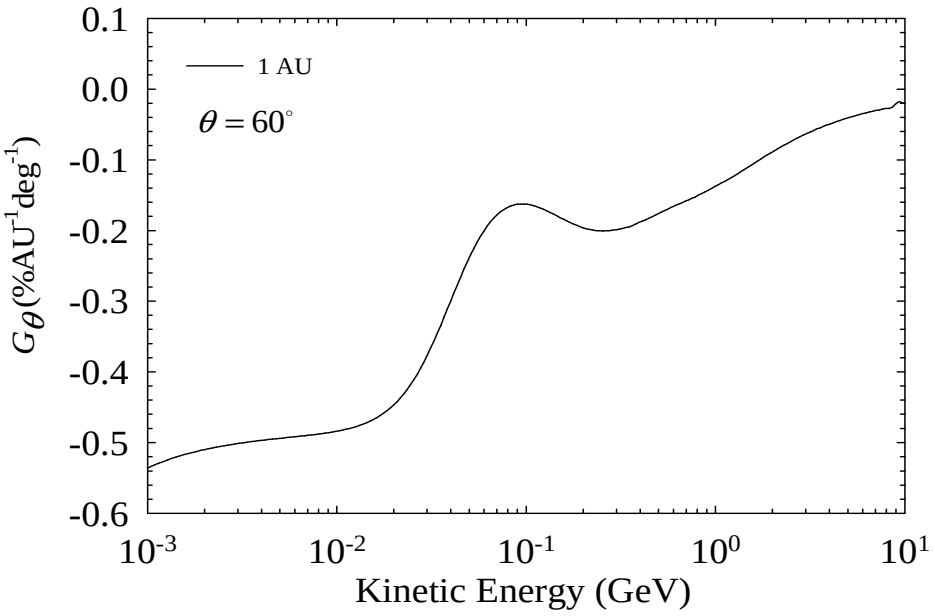

Figure 6.4: Computed G_θ as a function of kinetic energy for electrons at 1 AU with θ = 60° for the A < 0 magnetic polarity epoch.

6.2.2.2. Polar dependence

Shown in Figure 6.5 are the computed G_θ for 12 MeV galactic electrons as a function of polar angle computed at 1 AU and 5 AU. Top panel of Figure 6.5 shows the polar dependence of this gradient at 1 AU; below 90° it is negative but positive above 90°. It peaks around ~ 110° (~70°) with 0.78 % deg^{-1}. It appraches zero at the poles and at the equatorial plane as required by the boundary conditions specified in the model. The bottom panel shows it at 5 AU. The same tendencies are evident but the absolute values are much smaller. The gradients at other radial distances are not shown since they are much smaller than shown here.

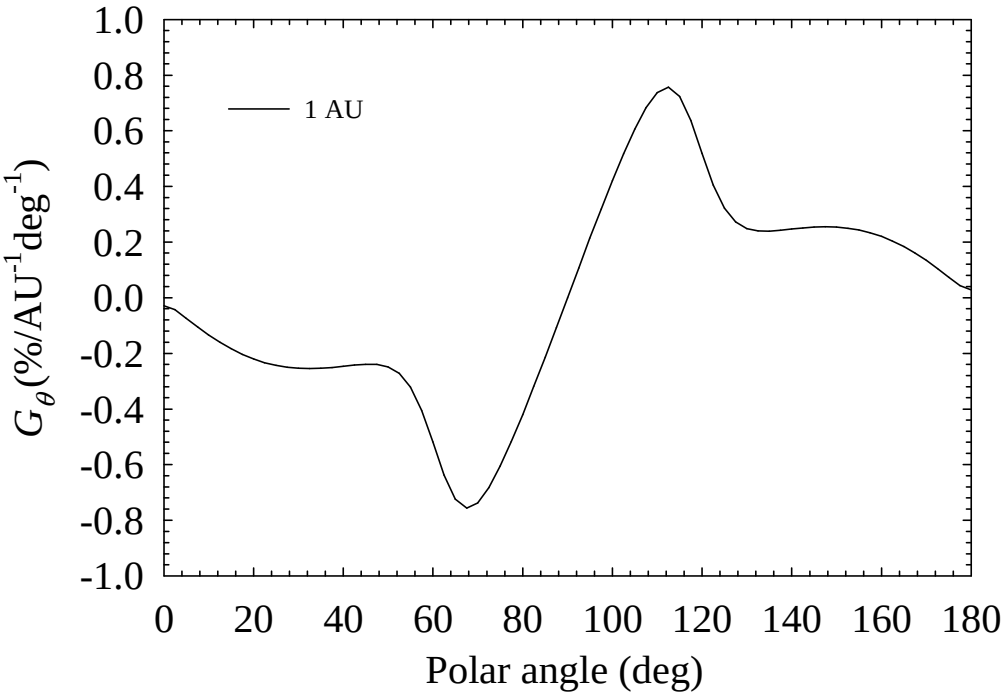

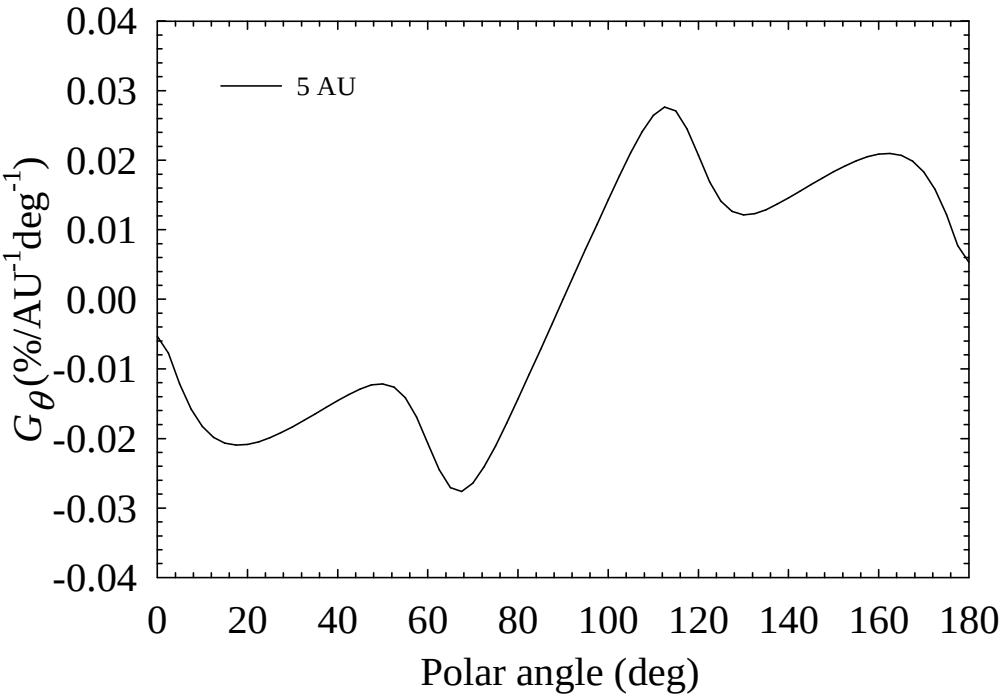

Figure 6.5: Computed polar dependence of G_θ for 1 AU and 5 AU respectively.

6.3. Electron spectra

Figure 6.6 shows the computed energy spectra for galactic electrons at 1 AU, 5 AU, 60 AU, 90 AU and 110 AU with θ = 10° and θ = 60° respectively for the A < 0 magnetic polarity epoch with tilt angle α = 5° for solar minimum conditions with full drifts as discussed in chapter 5. The diffusion coefficients used for these computations are those discussed in section 3.9. The spectra are shown from 1 AU to 110 AU and at different polar angles to illustrate how the modulation, especially below 100 MeV, changes from the inner heliosphere to the outer heliosphere.

The top panel of Figure 6.6 shows the spectra computed with θ =10°. The 1 AU and the 5 AU spectra show significant modulation already at ~5 GeV as compared to the spectra discussed in the previous chapter. With E > 100 MeV, the 1 AU and the 5 AU spectra are indistinguishable giving the same amount of modulation. The 1 AU spectrum shows the most modulation with the lowest intensities. The 60 AU spectrum shows already significant modulation from ~2 GeV and below.

The features of the 90 AU and 110 AU spectra have already been discussed in Chapter 5. An overall feature is that at 1 MeV maximum intensities are obtained, in contrast to GCRs protons where the modulation is always a minimum at lower energies. Another important feature of electron modulation is that with E < 50 MeV the modulation becomes constant with decreasing E, with the modulated spectra having the same slope (spectral index) as the LIS, down to 1 MeV. This is the consequence of the rigidity dependence of the diffusion coefficients being constant below $P \leq$ 0.4 GV, as discussed and motivated in section 3.9.

The bottom panel of Figure 6.6 shows the computed spectra at θ = 60°. This case is of special interest because it is the approximated heliolatitude of the Voyager 1 trajectory. The 1 AU and the 5 AU spectra show modulation already from ~ 10 GeV, meaningful higher than at θ =10°. With E > 100 MeV, the 1 AU and the 5 AU spectra are indistinguishable. The 60 AU, 90 AU and 110 AU spectra are almost the same above a few GeV and only start to deviate from the LIS at ~2 GeV. The 60 AU and the 90 AU spectra separate from each other at ~ 1 GeV, but remain very close, thus confirming the trends in the intensity gradients discussed above. The 110 AU spectrum, compared to the rest of the computed spectra, gives smaller but still significant modulation. Also in this case, all the modulated spectra below 50 MeV maintain the same slope as the LIS.

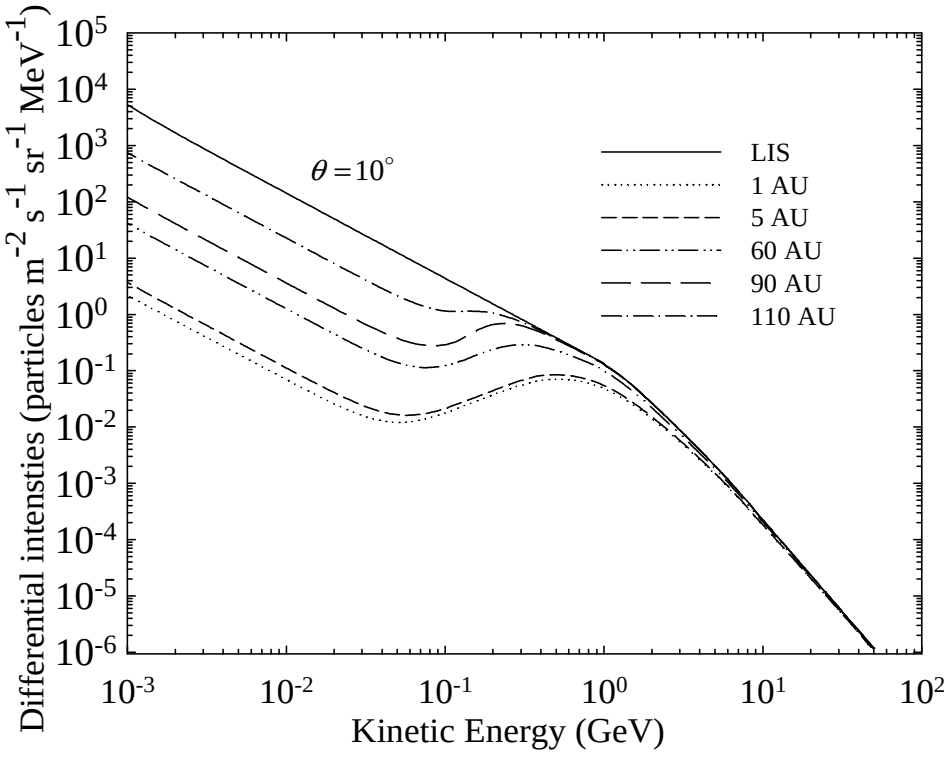

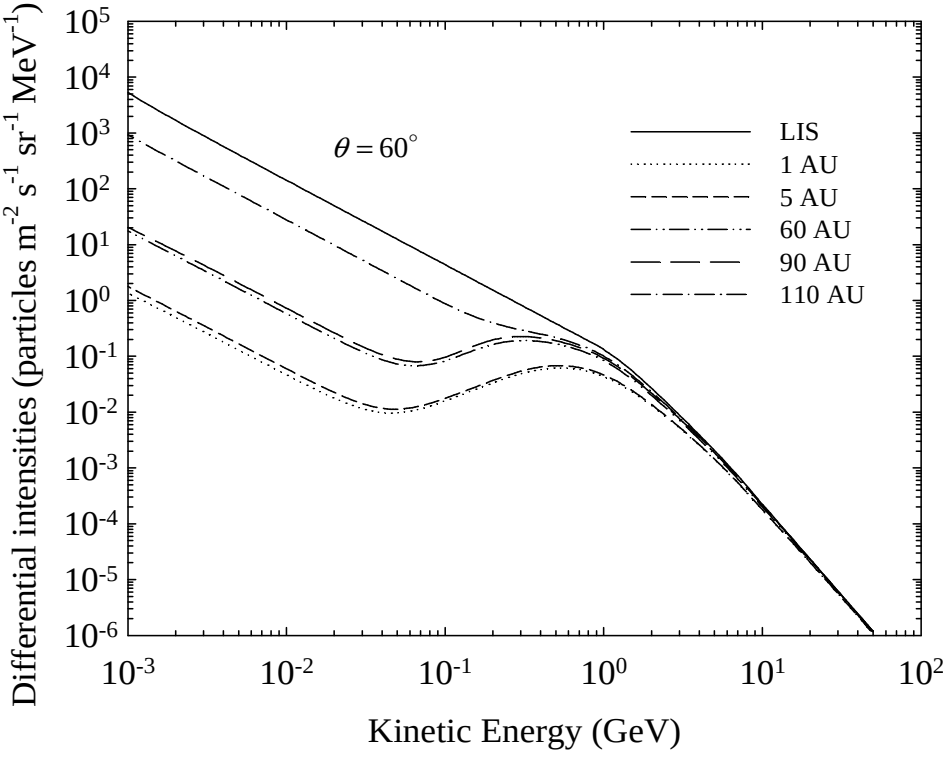

Figure 6.6: Computed electron spectra as a function of kinetic energy from the inner to the outer heliosphere. Spectra are shown at 1 AU, 5 AU, 60 AU, 90 AU and 110 AU, with θ = 10° (near the poles) and θ = 60° (Voyager 1 trajectory), respectively.

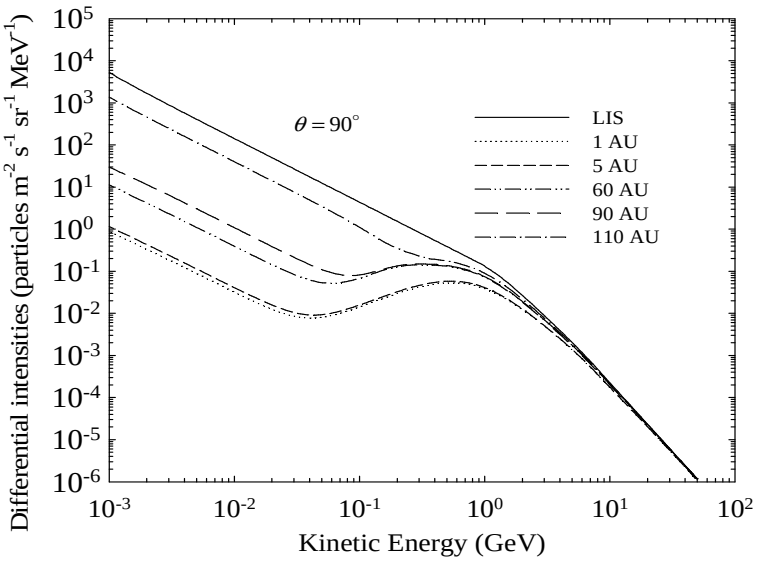

Figure 6.7: Similar to Figure 6.6 but with $\theta = 90^{o}$.

Figure 6.7 shows the computed spectra at 1 AU, 5 AU, 60 AU, 90 AU and 110 AU now at $\theta = 90^{o}$. The same features as mentioned above are evident here, although some trends are somewhat enhanced.

6.4. Polar dependence of electron intensities

Figure 6.8 shows the polar dependence of 12 MeV electrons computed at 1 AU (top panel), 5AU (middle panel) and 60 AU (bottom panel). At 1 AU a small polar dependence is evident with the minimum intensity obtained in the equatorial plane with $\theta = 90°$ and the maximum are obtained at the poles. At 5 AU and 60 AU this trend is enhanced.

As discussed above this trend gives in heliocentric spherical coordinates per definition a negative polar gradient from $\theta = 0°$ to $\theta = 90°$ but a positive polar gradient from $\theta = 90°$ to $\theta = 180°$. Observational reports usually do this the other way around, using heliolatitude where the equatorial plane is specified as 0° (similar to geographic latitude).

A more pronounced change is seen at 90 AU as shown in the top panel of Figure 6.9 where the intensities are becoming high at the poles with a modest G_{θ} between e.g. $\theta = 50°$ to $\theta = 90°$ but with very large polar gradients between $\theta = 0°$ to $\theta = 50°$. The trend of having the same sign for G_{θ} between e.g. $\theta = 0°$ and $\theta = 90°$ is now changing, the sign is switching around $\theta = 50°$ (130°). At 110 AU, as shown in the bottom panel of Figure 6.9, this feature is

pronounced. The Voyager 1 and 2 trajectories are unfortunately just outside this region of large polar gradients.

6.5. Radial dependence of electron intensities

Figure 6.10 shows the computed differential intensities for 12 MeV electrons as a function of radial distance between 1 AU and 120 AU, with θ = 10°, θ = 60° and θ = 90°. These computations are based on the modeling reported by Moeketsi (2004) and Nkosi (2006). A similar figure was shown in the previous chapter but only for the outer heliosphere (70 AU to 120 AU). As pointed out in the previous chapter, this steady radial dependence cannot reproduce the 6-14 MeV electron intensities as observed by Voyager 1 in the heliosheath despite that a strong radial dependence is depicted for the inner heliosphere, within the first 20 AU. This illustrates an important constraint when numerical models are compared to only one observational point, say the Earth, as many researchers do. In this case the electron spectrum at Earth may have been reproduced adequately by the mentioned approach, but now that the Voyager observations are additionally considered, the insight and conclusions change, causing in the process quite a challenge. This is discussed further below.

Figure 6.11 shows the computed radial dependence of 12 MeV electrons as a function of radial distances, from the inner heliosphere to the outer heliosphere, for three different scenarios described in the figure caption. The three scenarios are qualitatively similar in the outer heliosphere (r > 80 AU) and heliosheath, although subtle quantitative differences are evident. In the inner heliosphere the scenario with the diffusion coefficients independent of r gives very small radial gradient, with the level of modulation at this energy almost the same from Earth to 80 AU. In contrast, the other two scenarios give a significant radial gradient with the intensity decreasing by a factor of 8 between 1 AU and 60 AU. This has consequences for the intensity of low energy galactic electrons at Earth and will be discussed further below.

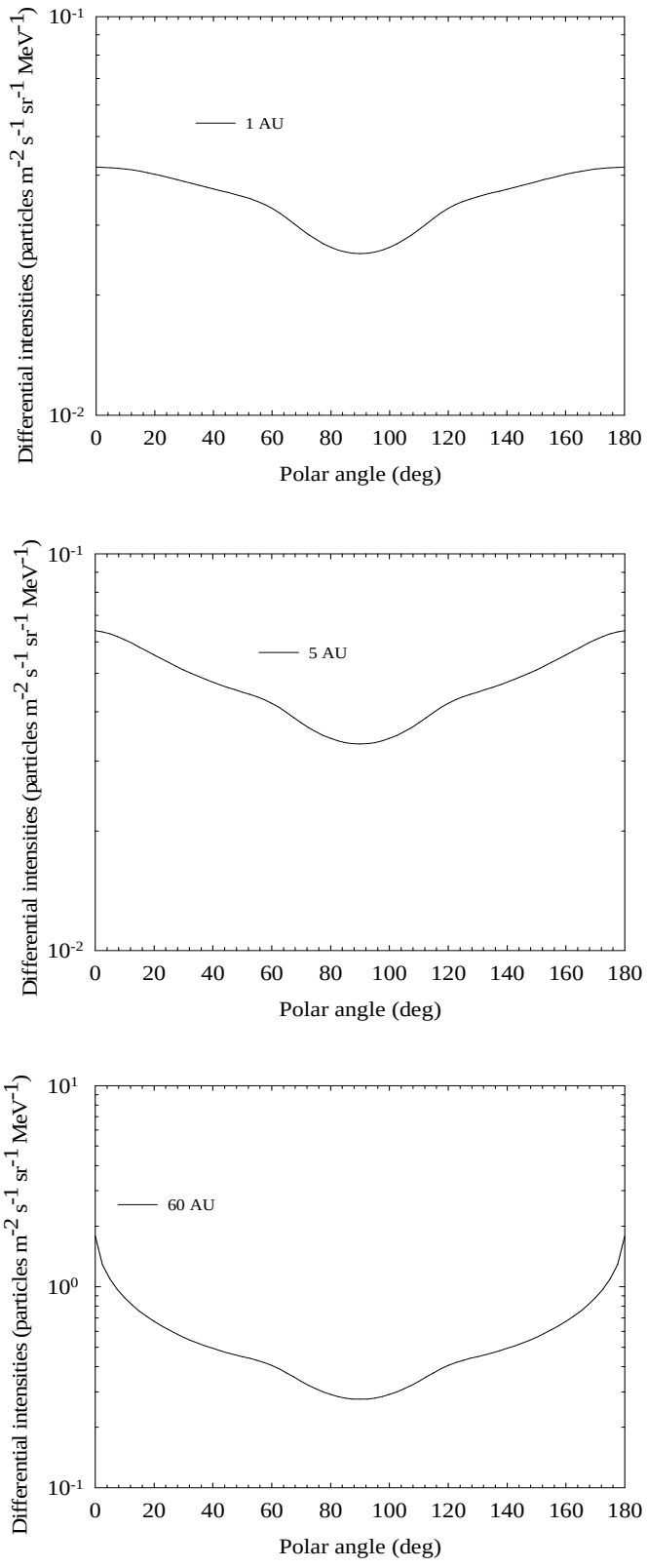

Figure 6.8: Computed 12 MeV galactic electron intensities as a function of polar angle at 1 AU, 5 AU and 60 AU, respectively. The equatorial plane is at $\theta = 90°$.

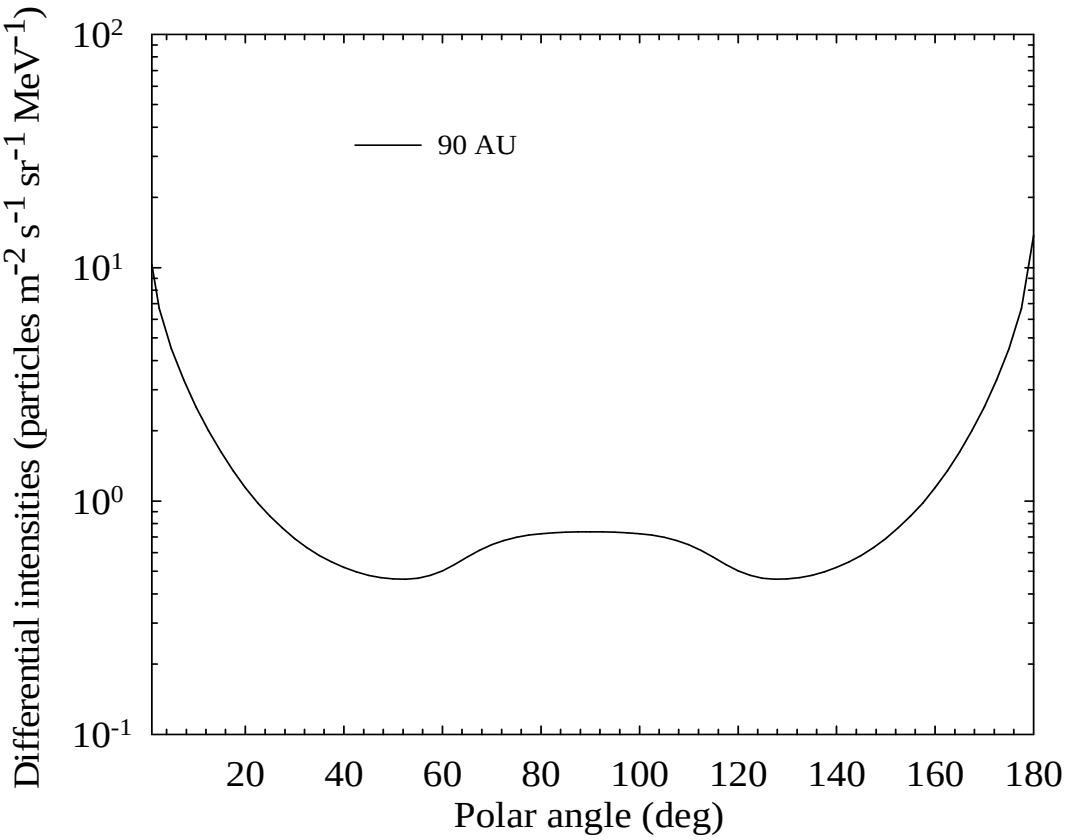

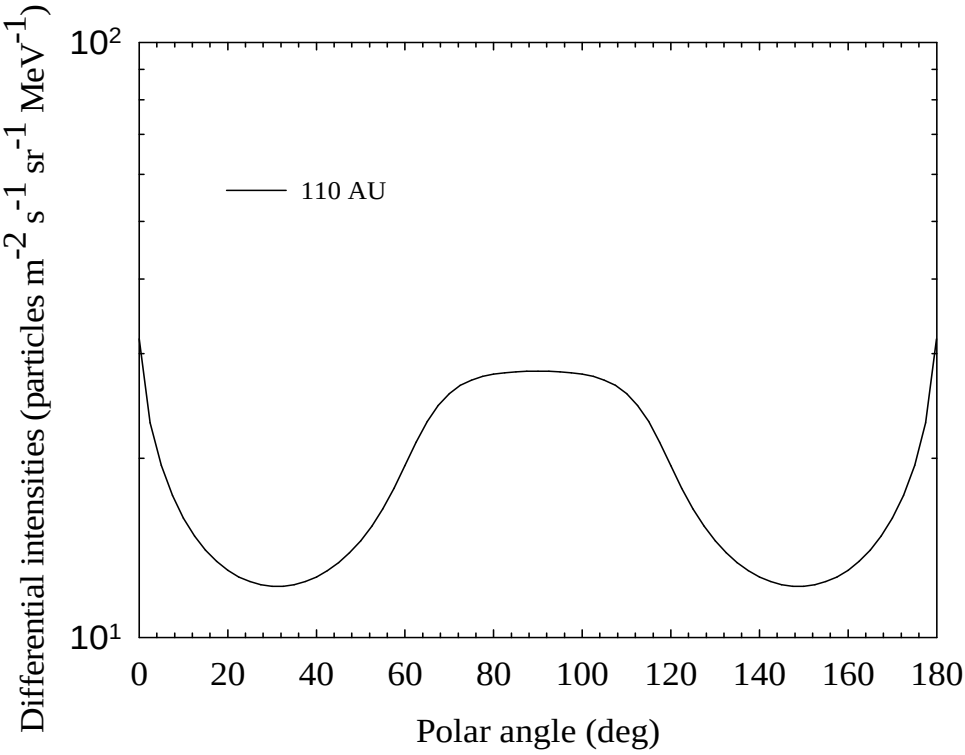

Figure 6.9: Computed 12 MeV galactic electron intensities at 90 AU and 110 AU as a function of polar angle. Note the trend in the polar gradients as follows from these panels and those in Figure 6.8.

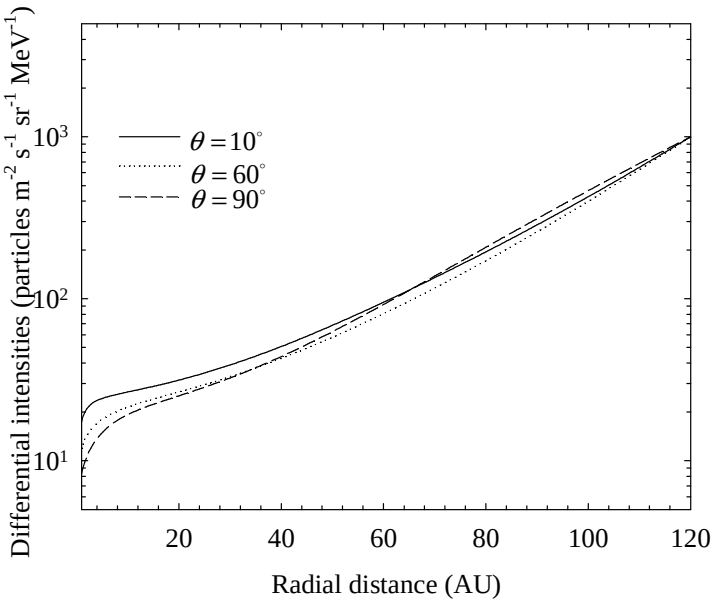

Figure 6.10: Radial dependence of 12 MeV electrons computed at three different polar angles θ =10°, θ = 60° and θ = 90° based on the modeling done by Moeketsi (2004) and Nkosi (2006).

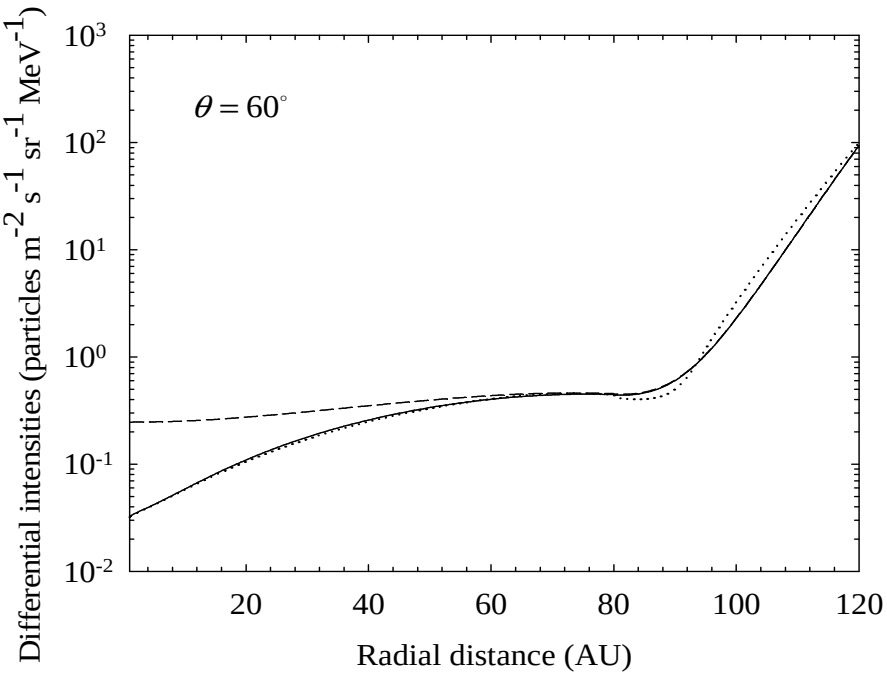

Figure 6.11: Computed radial dependence of 12 MeV electron intensity shown for three different profiles. Solid line is for V_r constant throughout the heliosphere with the radial dependence of the DCs proportional to $r^{1.2}$; dotted line shows V_r not-constant inside the TS and changing with radial distance in the heliosheath and with the radial dependence of the DCs proportional to $r^{1.2}$; the dashed line gives V_r constant throughout the heliosphere and with the DCs independent of r in the inner heliosphere as discussed in section 3.9; see Equations (3.38) and (3.40).

6.6. Comparison with observations

Figure 6.12 shows the computed spectra from the inner to the outer heliosphere (1 AU, 5 AU, 60 AU, 90 AU and 110 AU, with θ = 60°) together with observations at Earth and also for the outer heliosphere. Earth observations are from the PAMELA mission (Boezio, private communication, see also Boezio et al. 2011), the 1997 Ulysses observations (Potgieter et al. 1999) and the Evenson balloon flight data (Evenson et al. 1983), whereas the outer heliosphere observations are from Voyager 1 when it was at 112 AU (Webber, private communication, see also Caballero et al. 2010). The PAMELA data cover the energy range from 50 GeV (even higher if required) to 200 MeV, unfortunately not to any lower energy. The balloon flight data go to lower energies but then with severe systematic uncertainties because these short-term experiments are done inside the Earth's magnetosphere with ionospheric and atmospheric influences. The Ulysses data were obtained not at Earth but along its trajectory. At least down to 200 MeV, the Ulysses and balloon data are consistent with the much more accurate PAMELA data. Unfortunately, balloon data between 20 MeV and 80 MeV are considered less reliable while the Ulysses data around 10 MeV are certainly dominated by Jovian electrons. Voyager 1 and 2 electron data are available only between 4 MeV and 120 MeV.

One of the frustrations about electron observations is that below 100 MeV no space experiments are done at or close to Earth. This crucial part of the predicted (modeled) electron spectrum, where drifts are starting to play an increasing important role (e.g. Potgieter 1996); can therefore not be tested rigorously.

A purpose of this study is to establish when using the RRN LIS, if the model was able to produce good compatibility with Voyager 1 observations in the first place, with the energy range just perfect, while attempting to predict the galactic electron intensities at Earth. In this case compatibility with observations at Earth (if available) is expected to be poor because Jovian electrons are not included in the model. This was done in detail by Ferreira et al. (2001a,b,c). However, above ~200 MeV, where the observations are plentiful, the model seems to give good compatibility with the PAMELA, Ulysses and the Evenson observations despite that the modeling solutions are shown at θ = 60°. The polar intensity gradients are small as reported above making this comparison reasonable.

The balloon flight data below ~100 MeV (three points) should not be interpreted as a good observation of galactic electrons at Earth. In fact, the modeled spectrum at 60 AU seems more consistent with these data points clearly pointing to the fact that they cannot be seen as galactic electrons. The same applies to the three Ulysses data points around 10 MeV which are published (confirmed) as Jovian electrons.

The RRN LIS also displays the spectral slope of the PAMELA observations above 10 GeV. This LIS is normalized to PAMELA observations at 50 GeV as shown in the graph.

A conclusion is that the modeled spectrum at 1 AU is compatible to the accurate PAMELA electron data down to 200 MeV. Clearly, the model reproduces the Voyager 1 observed spectrum (available only between ~6 MeV and ~120 MeV) at 112 AU in all detail. The computed spectra at 1 AU and 5 AU are presented here as plausible galactic electron spectra from 1 MeV to 200 MeV. This will be discussed further below.

Figure 6.13 shows the radial dependence for the three computed profiles from Figure 6.11 compared to the observed radial profile for 6-14 MeV electrons. The peak shown at 5 AU was when Voyager 1 encountered the Jovian magnetosphere so that this radial profile is dominated by Jovian electrons up to ~20 AU (see also Ferreira et al. 2001a, b, c) whereas galactic electrons clearly dominate from $r > 80$ AU. The observations in the middle heliosphere, between 20 AU and 80 AU are controversial because the intensity level is close to the threshold energy of the detector which was designed to handle the high Jovian electron intensities. Now, for the first time, the Voyager 1 electron intensity at these low energies is exceeding the Jovian electron intensity observed during the Jupiter encounter. It is known that GCRs protons interacting with the spacecraft's frame produce secondary electrons which may enlarge the counting rate of electrons (to become background counts) so that it may be incorrect to interpret the intensity from 20 AU to 80 AU as galactic electrons. If this interpretation is correct, it remains controversial why there are several temporal changes in the electron profile not correlated to proton events. Unfortunately, only the researchers working with this detector can resolve this issue and they disagree (private conversations with Webber, McDonald and Stone; see also McDonald et al. 2006).

The only certainty is that with $r < 20$ AU, the Jovian electrons dominate. This means that it is unknown what the galactic electron intensity is at Earth at these low energies. With $E > 30$ MeV, the Jovian contribution subsides rapidly as illustrated by Ferreira et al. (2001a, b, c).

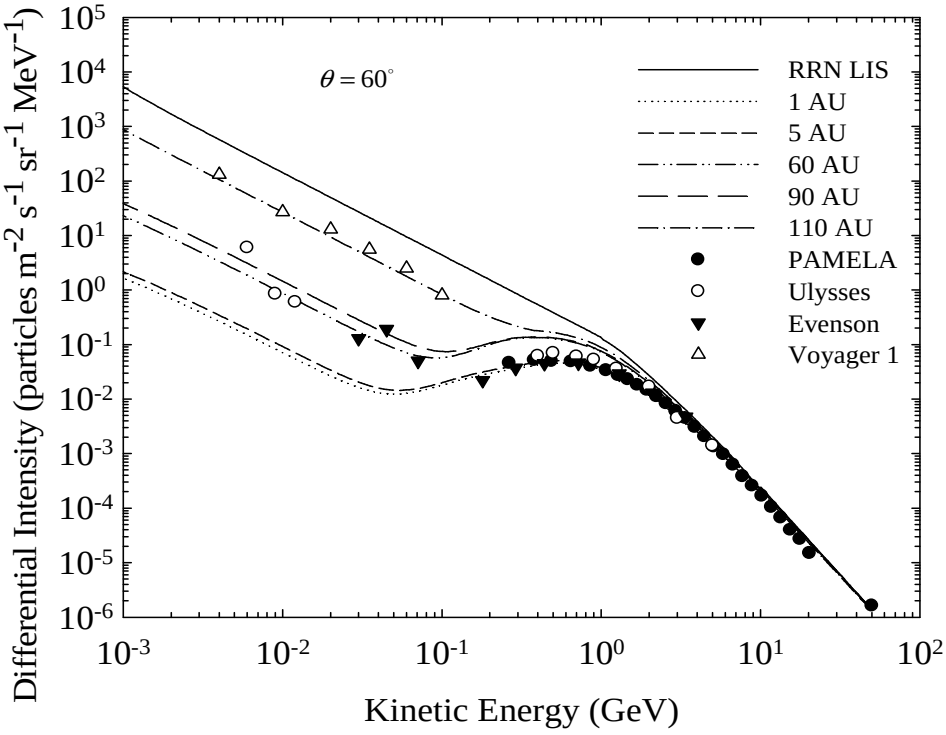

Figure 6.12: Computed electron spectra at 1 AU, 5 AU, 60 AU, 90 AU and 110 AU showing how the spectra are modulated from the inner to the outer heliosphere with $\theta = 60°$. These spectra are compared with observations from Voyager 1 (at 112 AU), PAMELA, Ulysses and balloon flights from Evenson, with references given in the text. The LIS is specified at 120 AU.

The modeling shown in Figure 6.13 is therefore an attempt to predict the galactic electron intensity at Earth at these low energies. Another aspect to consider here is that turbulence theory predicts that at these low energies, the electron diffusion coefficients should remain independent of rigidity (energy) meaning that modulation should remain the same with $E <$ 100 MeV at a given position, exactly as shown in Figure 6.12. If the DCs are indeed so large, the immediate implication is that not much modulation could occur at these energies as a function of radial distance, or in fact over a solar cycle, so that the flattish radial profile for the inner heliosphere in Figure 6.13 seems to be compatible with turbulence theory.

The predicted flat radial intensity in this figure (dashed line) is, from this point of view, thus a realistic scenario. The conclusion is therefore made that this predicted differential intensity (2.5×10^{-1} electrons m^{-2} sr^{-1} s^{-1} MeV^{-1}) at 12 MeV is the highest plausible intensity for galactic electrons at Earth. The other two scenarios, assuming a stronger radial dependence for the DCs are very close, and do give a much stronger radial intensity gradient towards the

inner heliosphere. They represent what is interpreted for this study as the lowest plausible galactic 12 MeV electron intensity at Earth (3 x 10^{-2} electrons m^{-2} sr^{-1} s^{-1} MeV^{-1}).

For the outer heliosphere, the controversy about background electron contributions is irrelevant so that the observations can be trusted as galactic electrons. But, there is another issue. The detectors on board the Voyagers cannot distinguish between electrons and positrons as the PAMELA detector does, so what is presented as observed galactic electrons are in fact the sum of galactic electrons and positrons. Fortunately, based on galactic propagation models (Moskalenko et al. 2002), the predicted positron contribution at 10 MeV is a factor of ~350 less than galactic electrons (see Figure 4.1).

As discussed in the previous chapter and emphasized here, is that the model does well in reproducing the galactic electron intensity at 12 MeV in the outer heliosphere. The conclusion is made that the relevant diffusion coefficients must be reduced abruptly once the TS is crossed and that they are significantly less inside the heliosheath than in the rest of the heliosphere. This conclusion should be taken into account when diffusion coefficients for the

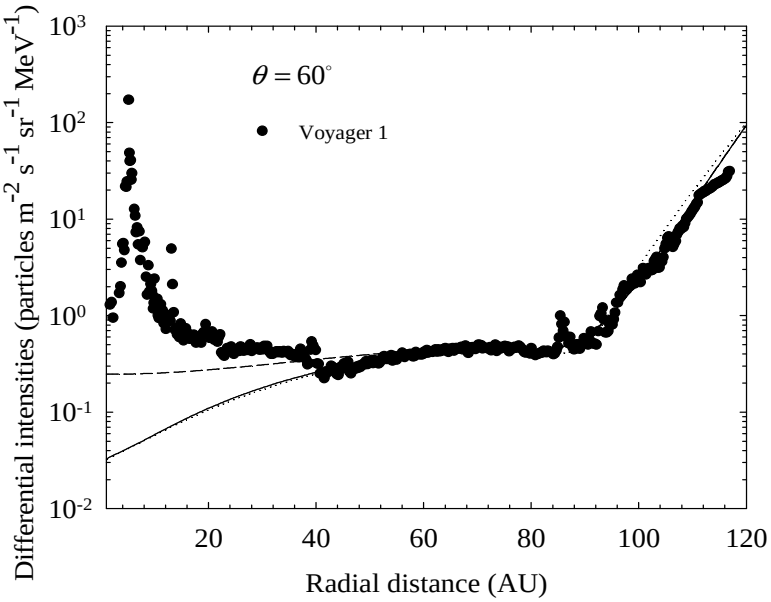

Figure 6.13: Radial dependence of 12 MeV electrons shown for the three computed profiles as in Figure 6.11, together with Voyager 1 observations between 6-14 MeV (Webber, private communications). The peak at 5 AU was when Voyager 1 encountered the Jovian magnetosphere. This profile is therefore dominated by Jovian electrons up to ~20 AU whereas galactic electrons dominate clearly from r > 80 AU.

heliosheath are calculated from fundamental diffusion and turbulence theory.

In addition it is claimed that the RNN LIS is probably the most realistic LIS so far. In order to test this rigorously additional electron spectra beyond 112 AU from Voyager 1 are required. This study should then be extended to include Voyager 2 observations to make it as comprehensive as possible.

6.7. Summary and conclusions

This final research chapter was focused on the modeling of 12 MeV galactic electrons from the inner to the outer heliosphere, making use of the new LIS (main result from chapter 5) and the appropriate diffusion coefficients, as discussed in chapter 3.

Radial and latitudinal gradients were computed as a function of kinetic energy and spatial position, with emphasis on polar angles of θ = 10°, θ = 60° and θ = 90°. Electron spectra, from 50 GeV down to 1 MeV were computed from the inner to the outer heliosphere to establish how electron modulation evolves over a distance of 120 AU from the Sun. They were compared to observations made near and at Earth, and at 112 AU in the outer heliosphere.

Concerning the radial gradients it was found that the computed values could range from as large as 25% AU^{-1} in the outer heliosphere at 1 MeV to almost zero at certain radial distances and with increasing energy.

Concerning the polar gradients it was found that they are overall quite small in the heliosphere, not even 1% deg^{-1} at 1 AU, with smaller numbers at larger radial distances. This was not surprising because drifts are generally suppressed in this 3D model by enhancing perpendicular diffusion in the polar direction as was introduced by Potgieter (1996). This is required in order to reproduce Ulysses observations of small latitudinal gradients. For a review, see Heber and Potgieter (2006). New observational results were published by De Simone et al. (2011) that seem compatible with computations.

The radial dependence of 12 MeV electrons was computed between 1 AU and 120 AU showing the full observed radial profile - see Figure 6.11. This profile was first computed using the model of Moeketsi (2004) and Nkosi (2006). It was found that previous attempts

could not resemble the latest Voyager 1 observations, so a new LIS was deduced, together with a set of diffusion coefficients fine-tuned for the whole heliosphere. This was then utilized to compute the radial gradients that resemble the Voyager 1 observations - see Figure 6.13.

Concerning the computed electron spectra it was found the RRN LIS displays the appropriate spectral slope, compatible with the PAMELA observations above 10 GeV, and seems the most appropriate electron LIS published so far.

The model reproduced the Voyager 1 observed spectrum at 112 AU in detail. Since the numerical 3D model did well in reproducing the galactic electron intensity at 12 MeV in the outer heliosphere, the conclusion was made that the relevant diffusion coefficients must be reduced abruptly once the TS is crossed and that they are significantly less inside the heliosheath than in the rest of the heliosphere. This conclusion should be taken into account when diffusion coefficients for the heliosheath are calculated from fundamental diffusion and turbulence theory.

It was concluded that the modeled spectrum at 1 AU is compatible to the accurate PAMELA electron data from 50 GeV down to 200 MeV. The new LIS is probably the most realistic LIS so far. In order to test this rigorously additional electron spectra beyond 112 AU from Voyager 1 are required. This study should then be extended to include Voyager 2 observations to make it as comprehensive as possible.

The conclusion was made that the predicted differential intensity (2.5×10^{-1} electron m^{-2} sr^{-1} s^{-1} meV^{-1}) at 12 MeV is the highest plausible intensity for galactic electrons at Earth. The other two studied scenarios, assuming a stronger radial dependence for the DCs were very close, and gave a much stronger radial intensity gradient towards the inner heliosphere. They represent what is interpreted for this study as the lowest plausible 12 MeV electron intensity at Earth (3×10^{-2} electron m^{-2} sr^{-1} s^{-1} meV^{-1}). The computed spectra at 1 AU and 5 AU are presented as plausible galactic electron spectra below 1 MeV to 200 MeV. See Figure 6.12.

Chapter 7

Summary and conclusions

Voyager 1 crossed the termination shock in 2004 at 94 AU and since then it has been exploring the inner heliosheath region. In 2010 it returned interesting observations regarding the galactic electron spectrum for energies below 100 MeV. These observations give an answer to a long-outstanding question about the shape of the LIS at these lower energies. In this study, utilizing these observations, a new LIS was developed and applied to study the modulation of 12 MeV galactic electrons in the heliosphere.

The background about cosmic ray modulation and the heliosphere was discussed, this include the solar wind, the HMF and the geometry of the heliosphere. Since the focus shifted to the outer heliosphere, the intensity profile that Voyager 1 observed was shown. It is evident that the spacecraft is approaching the HP zone. Unfortunately, the solar wind speed detector is not working on Voyager 1 so that it is not yet confirmed if it is inside the HP zone.

The mathematical and numerical model based on the heliospheric transport equation was discussed together with aspects of the diffusion tensor which had to be assumed in order to solve the transport equation. The focus was on the diffusion coefficients because gradient and curvature drifts for low energy electrons are negligible.

The rigidity and the spatial dependence of these diffusion coefficients are of special interest since it determines how the computed spectra get modulated throughout the heliosphere. The rigidity and the spatial dependent for $\lambda_{||}$ as given by the theoretical work of Teufel and Schlickeiser (2002) at Earth, and on which the rest are based, were followed. But, first the work done on these diffusion coefficients and implemented in the models by Ndiitwani (2005) and by Nkosi (2006) was illustrated and evaluated. It was found that the rigidity dependence that they used, had to be changed to find compatibility with recent Voyager 1 electron observations which form the most important part of this study. Different rigidity and spatial dependence for the diffusion coefficients were thus implemented in the 3D model.

A new local interstellar spectrum was found based on comparisons of the model and Voyager 1 observations. It was subsequently implemented to do computational modulation for the whole heliosphere.

The transition that the solar wind speed makes across the TS and into the heliosheath was discussed and implemented in the model. For the heliosheath it was assumed that no adiabatic energy losses occur so that the divergence of the solar wind velocity remained divergence free. Modulated electron spectra were subsequently computed and the results were compared to observations in the outer heliosphere and at the Earth.

Conclusions of this study are:

- Electron spectra, from 50 GeV down to 1 MeV, were computed from the inner to the outer heliosphere to establish how electron modulation evolves over a distance of 120 AU from the Sun. Comparison between these computed electron spectra for the outer heliosphere and corresponding Voyager 1 observations required the use of a modified set of diffusion coefficients in the 3D model. The rigidity dependence of previously used diffusion coefficients could be simplified while maintaining the basics of turbulence theory applied to heliospheric conditions.

- The model reproduced the Voyager 1 observed spectrum at 112 AU in detail. Since the numerical 3D model did well in reproducing the galactic electron intensity at 12 MeV in the outer heliosphere, the conclusion was made that the relevant diffusion coefficients must be reduced abruptly once the TS is crossed and that they are significantly less inside the heliosheath than in the rest of the heliosphere. This conclusion should be taken into account when diffusion coefficients for the heliosheath are calculated from fundamental diffusion and turbulence theory.

- Radial and polar gradients were computed as a function of kinetic energy and spatial position in the heliosphere. They were compared to observations made near and at Earth, and at 112 AU in the outer heliosphere. Concerning the radial gradients it was found that the computed values could range from as large as 25% AU^{-1} in the outer heliosphere at 1 MeV to almost zero at radial distances closer to the Sun, and with increasing energy.

- Concerning the polar gradients it was found that they are overall quite small in the heliosphere, not even 1% deg^{-1} at 1 AU, with smaller numbers at larger radial distances.

This was not surprising because drifts are generally suppressed in this 3D model in order to reproduce Ulysses observations of small latitudinal gradients.

- Apart from adjusting the diffusion coefficients, a new local interstellar spectrum for galactic electron was deduced.

- Using this new LIS, it was found that the computed electron spectrum at 1 AU and from 10 GeV down to 200 MeV is compatible to the accurate PAMELA electron data. It was found that this LIS displayed the correct spectral slope (index) and thus seems the most appropriate electron LIS published so far. The LIS from Langner et al. (2001) was found too high at low energy while the LIS from Webber and Higbie (2008) was too low at low energy. In order to test this rigorously additional electron spectra beyond 112 AU from Voyager 1 are required. This study should then be extended to include Voyager 2 observations to make it as comprehensive as possible.

- The galactic electron intensity below 50 MeV is not known at Earth because of the dominance of the Jovian electrons at these energies in the inner heliosphere. Using the compatibility obtained between computations and observations in the outer heliosphere, the model was used to make estimate of this intensity at Earth. The conclusion was made that the predicted differential intensity, 2.5×10^{-1} electrons m^{-2} sr^{-1} s^{-1} MeV^{-1}, at 12 MeV is the highest plausible intensity for galactic electrons at Earth. The lowest plausible 12 MeV electron intensity at Earth is 3×10^{-2} electrons m^{-2} s^{-1} sr^{-1} MeV^{-1}. The corresponding computed spectra at 1 AU and 5 AU are presented as plausible galactic electron spectra from 1 MeV to 200 MeV.

The following aspects of electron modulation, mostly considered to be beyond the scope of this present study, need further investigation:

- Applying the model for studying radial intensity profiles to higher energies for galactic electrons, up to 120 MeV, the highest energy available from Voyager 1.

- Extending the computational study to include new observational results from Voyager 2. A comparison of particle, solar wind and magnetic field observations and comprehensive modeling results between Voyager 1 and Voyager 2 seems most relevant.

- To study the solar wind profile in more detail in the heliosheath by utilizing Voyager 2 observations. These types of data are not available from Voyager 1.

- Extending the computational electron studies to periods of increased solar activity and then pursue the issue of computing the galactic electron intensity at Earth during this phase of the solar cycle. Recent electron observations of the PAMELA mission may be useful in this context.

- Investigate how the new LIS for galactic electrons based on the modulation studies presented for this work, could be match to the computations of a galactic electron spectrum based on the GALPROP galactic propagation code.

References

Adriani, O., Barbarino, G.C., Bazilevskaya, G.A., et al., New measurement of the antiproton-to-proton flux ratio up to 100GeV in the cosmic radiation, Phys. Rev. Lett., 102, 051101:1-5, 2009.

Adriani, O., Barbarino, G.C., Bazilevskaya, G.A., et al., The discovery of geomagnetically trapped cosmic ray antiprotons, Astrophys. J. Lett., 737, L29-L34, 2011.

Alcaraz, J., Alvisi, D., Alpat, B., et al., Protons in near Earth orbit, Phys. Lett., 472, 215-226, 2000.

Beatty, J.J., and Westerhoff, S., The highest energy cosmic rays, Annul. Rev. Nuc. Part. Sci., 59, 319-345, 2009.

Bieber, J.W., Matthaeus, W.H., Smith, C.W., et al., Proton and electron mean free paths: the Palmer consensus revisited, Astrophys. J., 420, 294-306, 1994.

Boezio, M., Carlson, P., Francke, T., et al., The cosmic ray electron and positron spectra measured at 1 AU during solar minimum activity, Astrophys. J., 532, 653-669, 2000.

Boezio, M., Pearce, M., Picozza, P., et al., PAMELA and indirect dark matter searches, New J. Physics, 11, 105023:1-25, 2009.

Boezio, M., Adriani, O., Barbarino, G.C., et al., The cosmic ray electron flux measured by the PAMELA experiment between 1 and 625 GeV, Phys. Rev. Lett., 106, 201101:1-5, 2011.

Burger, R.A., Potgieter, M.S., and Heber, B., Rigidity dependence of cosmic ray proton latitudinal gradients measured by Ulysses spacecraft: Implications for the diffusion tensor, J. Geophys. Res., 105, 27447-27455, 2000.

Burlaga, L.F., Ness, N.F., Acuna, M.H., et al., Observations of magnetic fields at the termination shock by Voyager 2, Nature, 454, 75-77, 2008.

Caballero-Lopez, R.A., Moraal, H., and McDonald, F.B., The modulation of galactic electrons in the heliosheath, Astrophys. J., 725, 121-127, 2010.

Cranmer, S.R., Coronal holes and the high-speed solar wind, Space Sci. Rev., 101, 229-294, 2002.

De Simone, N., Di Felice, V., Boezio, M., et al., Latitudinal gradients of galactic cosmic ray protons in the inner heliosphere-PAMELA and Ulysses observations, Astrophys. Space Sci. Trans., 7, 425-434, 2011.

Dröge, W., Particle scattering by magnetic fields, Space Sci. Rev., 93, 121-151, 2000.

Du Vernois, M.A., Barwick, S.W., Beatty, J.J., et al., Cosmic-ray electrons and positrons from 1 to 100GeV: Measurements with HEAT and their interpretation, Astrophys. J., 559, 296-303, 2001.

Earl, J.A., The diffusive idealization of charged particle transport in random magnetic fields, Astrophys. J., 193, 231-242, 1974.

Evenson, P., Garcia-Munoz, M., Meyer, P., et al., A quantitative test of solar modulation theory: proton, helium and electron spectra from 1965 through 1979, Astrophys. J., 275, L15-L18, 1983.

Ferreira, S.E.S, A study of the modulation of cosmic ray electrons in the heliosphere, M.Sc. dissertation, Potchefstroom University, South Africa, 1998.

Ferreira, S.E.S., The heliospheric transport of galactic cosmic ray and Jovian electrons, Ph.D. thesis, Potchefstroom University, South Africa, 2002.

Ferreira, S.E.S., and Potgieter, M.S., The modulation of 4-16 MeV electrons in the outer heliosphere: Implications of different local interstellar spectra, J. Geophys. Res., 107, SSH 12:1-10, 2002.

Ferreira, S.E.S., and Potgieter, M.S., Galactic cosmic rays in the heliosphere, Adv. Space Res., 34, 115-125, 2004.

Ferreira, S.E.S., and Scherer, K., Modulation of cosmic ray electrons in the outer heliosphere, Astrophys. J., 616, 1215-1232, 2004.

Ferreira, S.E.S, Potgieter, M.S., Burger, R.A., and Heber, B., Modulation effects of anisotropic perpendicular diffusion on cosmic ray electron intensities in the heliosphere, J. Geophys. Res., 105, 305-314, 2000.

Ferreira, S.E.S., Potgieter, M.S., Burger, R.A., et al., Modulation of Jovian and galactic electrons in the heliosphere 1. Latitudinal transport of few MeV electrons, J. Geophys. Res., 106, 979-987, 2001a.

Ferreira, S. E. S., Potgieter, M. S., Burger, R. A., et al., Modulation of Jovian and galactic electrons in the heliosphere: 2 Radial transport of a few MeV electrons, J. Geophys. Res., 106, 29, 313-321, 2001b.

Ferreira, S.E.S., Potgieter, M.S., Heber, H., et al., Latitudinal transport of 7 MeV Jovian and galactic electrons, Proc. 27th Inter. Cosmic Roy Conf, (Hamburg,) 8, 3702-3705, 2001c.

Ferreira, S.E.S., Potgieter, M.S., Heber, B., et al., Solar wind effects on the transport of 3-10 MeV cosmic ray electrons from solar minimum to solar maximum, Astrophys. J., 549, 552-560, 2003.

Fichtner, H., Anomalous cosmic rays: Messengers from the outer heliosphere, Space Sci. Rev., 95, 639-754, 2001.

Fichtner, H., Potgieter, M.S., Ferreira, S.E.S., and Burger, R.A., On the propagation of Jovian electrons in the heliosphere: transport modeling in 4-D phase space, Geophys. Res. Lett., 27, 1611-1614, 2000.

Fisk, L.A., Solar system plasma physics, North Holland Publ. Co., 1, 24-92, 1979.

Fisk, L.A., Koslovsky, B. and Ramaty, R., An interpretation of the observed Oxygen and Nitrogen enhancements in low energy cosmic rays, Astrophys. J., 190, L35-L37, 1974.

Forbush, E., Three unusual cosmic ray increase probably due to the charged particles from the Sun, Phys. Rev., 70, 771-772, 1946.

Fujii, Z., and McDonald, F.B., The radial intensity gradients of galactic and anomalous cosmic rays, Adv. Space Res., 23, 437-441, 1999.

Fujii, Z., and McDonald, F.B., Radial diffusion coefficients and the distance to the modulation boundary for galactic and anomalous cosmic rays, Adv. Space Res., 23, 559-564, 2001.

Garcia-Munoz, M., Mason, G.M., and Simpson J.A., The abundance of Galactic cosmic ray Carbon, Nitrogen and Oxygen and their astrophysical implications, Astrophys. J., 184, 967-994, 1973

Gil, A., and Alania, M.V., 27 day variations of cosmic rays for the minima epochs of solar activity: Experimental and 3-D drift modeling results, Proc. 27th Inter. Cosmic Rays Conf. (Hamburg), 9, 3725-3728, 2001.

Gleeson, L.J., and Axford, W.I., Cosmic rays in the interplanetary medium, Astrophys. J. Lett., 149, L115-L118, 1967.

Gleeson, L.J., and Axford, W.I., The Compton–Getting effect, Astrophys. Space Sci., 2, 431-440, 1968.

Grimani, C., Stephens, S.A., Cafagna, F.S., et al., Measurements of the absolute energy spectra of cosmic-ray positrons and electrons above 7 GeV, Astron. Astrophys., 392, 287-294, 2002.

Hasselmann, K., and Wibberenz, G., Scattering of charged particles by random electro-magnetic fields, Zeitschrift für Geophysik, 34, 353-388, 1968.

Hasselmann, K., and Wibberenz, G., A note on the parallel diffusion coefficient, Astrophys. J., 162, 1049-1051, 1970.

Hattingh, M., The modulation of galactic cosmic rays in three-dimensional heliosphere, Ph.D. thesis, Potchefstroom University, South Africa, 1998.

Heber, B., and Potgieter, M.S., Cosmic rays at high heliolatitudes, Space Sci. Rev., 127, 117-194, 2006.

Heber, B., and Potgieter, M.S., Galactic and anomalous cosmic rays through the solar cycle: New insights from Ulysses, in The heliosphere through the Solar Activity Cycle, edited by Balogh, A., Lanzerotti, L.J., and Suess, S.T., 195-249, 2007.

Heber, B., Raviart, A., Paizis, C., et al., Modulation of galactic cosmic ray particles observed onboard Ulysses spacecraft, Proc. 23rd Inter. Cosmic Ray Conf. (Calgary), 3, 461-464, 1993.

Hoeksema, J.T., Large scale structure of the heliospheric magnetic field: 1976-1991, Proc. Solar Wind Seven, 191-196, 1992.

Intriligator, D.S., and Webber, W.R., Voyagers 1 and 2 in a shrunken and squashed heliosphere, J. Geophys. Res., 116, 06105:1-8, 2011.

Jokipii, J.R., Cosmic ray propagation. I. Charged particles in a random magnetic field, Astrophys. J., 146, 480-487, 1966.

Jokipii, J.R., Propagation of cosmic rays in the solar wind, Rev. Geophys. Space Phys., 9, 27-87, 1971.

Jokipii, J.R., and Kóta, J., The polar heliospheric magnetic field, J. Geophys. Res., 16, 1-4, 1989.

Jokipii, J.R., and Parker E.N., On the convection, diffusion and adiabatic deceleration of cosmic rays in the solar wind, Astrophys. J., 160, 735-744, 1970.

Jokipii, J.R., and Thomas, B., Effects of drift on the transport of cosmic rays. IV. Modulation by a wavy interplanetary current sheet, Astrophys. J., 243, 1115-1122, 1981.

Jones, F.C., and Ellison, D.C., The plasma physics of shock acceleration, Space Sci. Rev., 58, 259-346, 1991.

Kobayashi, T., Nishimura, J., Komori, Y., et al., High energy cosmic ray electrons beyond 100 GeV, Proc. 26th Inter. Cosmic Ray Conf., 3, 61-64, 1999.

Kóta, J., and Jokipii, J. R., Effects of drift on the transport of cosmic rays. VI: A three dimensional model including diffusion, Astrophys. J., 265, 573-581, 1983.

Krimigis, K.S., Roelof, E.C., Decker, R.B., and Hill, M.E., Zero outward flow velocity for plasma in a heliosheath transition layer, Nature, 477, 359-361, 2011.

Langner, U.W., Effects of different local interstellar spectra on the heliospheric modulation of cosmic rays, M.Sc. dissertation, Potchefstroom University, South Africa, 2000.

Langner, U.W., The effects of termination shock acceleration on cosmic rays in the heliosphere, Ph.D. thesis, Potchefstroom University, South Africa, 2004.

Langner, U.W., and Potgieter, M.S., Heliospheric Modulation of cosmic ray positrons and electrons: Effects of the heliosheath and the solar wind termination shock, Astrophys. J., 602, 993-1001, 2004a.

Langner, U.W., and Potgieter, M.S., Effects of the solar wind termination shock on charge-sign dependent cosmic ray modulation, Adv. Space Res., 34, 144-149, 2004b.

Langner, U.W., de Jager, O.C., and Potgieter M.S., On the local interstellar spectrum for cosmic ray electrons, Adv. Space Res., 27, 517-522, 2001.

Langner, U.W., Potgieter, M.S., Fichtner, H., and Borrmann, T., Modulation of anomalous protons: Effects of different solar wind speed profiles in the heliosheath, J. Geophys. Res., 111, 01106:1-14, 2006.

Longair, M.S., Cosmic rays and the Galactic radio background emission, in Low Frequency astrophysics from Space, Springer-Verlag, 362, 227-236, 1990.

Manuel, R., Ferreira, S.E.S. and Potgieter, M.S., Cosmic ray modulation in the outer heliosphere: Predictions for cosmic ray intensities up to the heliopause along Voyager 1 and 2 trajectories, Adv. Space Res., 48, 874-883, 2011.

McDonald, F.B., Webber, W.R., Stone, E.C., et al., Physics of the inner heliosheath: Theory, and Future Prospects, in IAP Conf. Proc., ed., Heerishuisen, J., et al., (Melville, NY: IAP), 858, 79-85, 2006.

McDonald, F.B., Webber, W.R., Stone, E.C., et al., Voyager observations of galactic cosmic ray electrons in the heliosheath, Eos Trans. AGU, Fall Meet., Abstract SH11A-082007, 3992-3995, 2007.

Mocchiutti, E., Adriani, O., Barbarino, G.C., et al., The PAMELA experiment, arXiv: 0905.225v1, [astro-ph. HE], 2009.

Moeketsi, D.M., Modeling of galactic and Jovian electrons in the heliosphere, M.Sc. dissertation thesis, Potchefstroom University, South Africa, 2004.

Moeketsi, D.M., Potgieter, M.S., Ferreira, S.E.S., et al., The heliospheric modulation of 3-10 MeV electrons: Modeling changes in the solar wind speed in relation to perpendicular polar diffusion, Adv. Space Res., 35, 597-604, 2005.

Moskalenko, I.V., Strong, A.W., and Reimer, O., Diffuse galactic gamma-rays: constraining cosmic ray origin and propagation, AIP Conf. Proc., 510, 283-290, 2000.

Moskalenko, I.V., Strong, A.W., Ormes, J.F., et al., Secondary antiprotons and propagation of cosmic rays in the galaxy and heliosphere, Astrophys. J., 565, 280-296, 2002.

Moskalenko, I.V., Ptuskin, V.S., Jones, F.C., et al., Dissipation of Magnetohydrodynamic waves on energetic particles: The impact on interstellar turbulence and cosmic ray transport, Astrophys. J., 642, 902-916, 2006.

Ndiitwani, D.C., A study of modulation of modulation of galactic time dependent cosmic rays in the heliosphere, M.Sc. dissertation, North -West University, South Africa, 2005.

Ndiitwani, D.C., Ferreira, S.E.S., Potgieter, M.S., and Heber, B., Modeling cosmic ray intensities along the Ulysses trajectory, Ann. Geophys., 23, 1061-1070, 2005.

Ngobeni, M.D., Aspects of the modulation of cosmic rays in the outer heliosphere, M.Sc. dissertation, North-West University, South Africa, 2006.

Ngobeni, M.D., and Potgieter, M.S., The heliospheric modulation of cosmic rays: effects of a latitude dependent solar wind termination shock, Adv. Space Res., 46, 391-401, 2010.

Nkosi, G.S., A study of cosmic ray anisotropies in the heliosphere, M.Sc. dissertation, North-West University, South Africa, 2006.

Nkosi, G.S., Potgieter, M.S., and Ferreira, S.E.S., Electron anisotropies in the inner heliosphere, Planet. Space Sci., 56, 501-509, 2008.

Nkosi, G.S., Potgieter, M.S., and Webber, W.R., Modeling of low–energy galactic electrons in the heliosheath, Adv. Space Res., 48, 1480-1489, 2011.

Opher, M., Richardson, J.D., Toth, G., and Gombosi, T.I., Confronting observations and modeling: The role of the interstellar magnetic field in Voyager 1 and 2 asymmetries, Space Sci. Rev., 143, 43-55, 2009.

Parker, E.N., Dynamics of the interplanetary space and magnetic fields, Astrophys. J., 128, 664-676, 1958.

Parker, E.N., The stellar wind regions, Astrophys. J., 134, 20-27, 1961.

Parker, E.N., The passage of energetic charged particles through interplanetary space, Planet. Space Sci., 13, 9-49, 1965.

Picozza, P., Galper, A.M., Castellini, G., et al., PAMELA- a payload for antimatter matter exploration and light-nuclei astrophysics, Astropart. Phys., 27, 296-315, 2007.

Potgieter, M.S., The modulation of galactic cosmic rays as described by a three dimensional drift model, Ph.D thesis, Potchefstroom University, South, Africa, 1984.

Potgieter, M.S., The heliospheric modulation of galactic electrons: Consequences of new calculations for the mean free path of electrons between 1 MeV and ~10 GeV, J. Geophysics. Res., 101, 411-424, 1996.

Potgieter, M.S., The heliospheric modulation of cosmic ray protons: The role of enhanced perpendicular diffusion during periods of minimum solar modulation, J. Geophys. Res., 105, 18295-18304, 2000.

Potgieter, M.S., Challenges to cosmic ray modeling from beyond the solar wind termination shock, Adv. Space Res., 41, 245-258, 2008.

Potgieter, M.S., and Ferreira, S.E.S., The importance of perpendicular diffusion in the heliospheric modulation of cosmic ray electrons, Adv. Space Res., 23, 463-466, 1999.

Potgieter, M.S., and Ferreira, S.E.S., Effects of the solar wind termination shock on the modulation of Jovian and galactic electrons in the heliosphere, J. Geophys. Res., 107, SSH 1:1-9, 2002.

Potgieter, M.S. and Strauss, R.,du,T., Heliospheric physics: shock acceleration in the heliosphere and anomalous cosmic rays, Nigerian J. Space Res., 8, 144-160, 2010.

Potgieter, M.S., le Roux, J.A., and Burger, R.A., Interplanetary cosmic ray radial gradients with steady state modulation model, J. Geophys. Res., 94, 2323-2332, 1989.

Potgieter, M.S., Ferreira, S.E.S., Heber, B., et al., Implications of the heliospheric modulation of cosmic ray electrons observed by Ulysses, Adv. Space Res., 23, 467-470, 1999.

Ptuskin, V.S., Moskalenko, I.V., Jones, F.C., et al., Dissipation of magnetohydrodynamic waves on energetic particles: The impact on interstellar turbulence and cosmic ray transport, Astrophys. J., 642, 902-916, 2006.

Richardson, J.D., Kasper, J.C., Wang, C, et al., Cool heliosheath plasma and deceleration of the upstream solar wind at the termination shock, Nature, 454, 63-66, 2008.

Scherer, K., Fichtner, H., Strauss, R.du,T., et al., On cosmic ray modulation beyond the heliopause: where is the modulation boundary? Astrophys. J., 735, 128-132, 2011.

Simpson, J.A., Cosmic radiation: Particle astrophysics in the heliosphere, in Frontiers in cosmic physics: Symposium in memory of Serge Korff, edited by Mendell, R.B., and Mincer, A. J., New York Academy of Sciences, New York, 655, 95-137, 1992.

Simpson, J.A., The cosmic radiation: Reviewing the present and future, Proc. 29th Inter Cosmic Ray Conf. (Durban): Invited, Rapporteur and Highlighted papers, 8, 4-23, 1997.

Snyman, J.L., Modeling of the heliosphere and cosmic rays transport, M.Sc. dissertation, North-West University, South Africa, 2007.

Stawicki, O., On solar wind magnetic fluctuations and their influence on the transport of charge particles in the heliosphere, Ph.D. thesis, Ruhr-Universität Bochum, Germany, 2003.

Stone, E.C., Cummings, A.C., McDonald, F.B., and Webber, W.R., The distance to the solar wind termination shock in 1993 and 1994 from the observations of anomalous cosmic rays, J. Geophys. Res., 101, 11017-11025, 1996.

Stone, E.C., Cummings, A.C., McDonald, F.B., et al., Voyager1 explores the termination shock region and the heliosheath beyond, Science, 309, 2017-2020, 2005.

Stone, E.C., Cummings, A.C., McDonald, F.B., et al., An asymmetric solar wind termination shock, Nature, 454, 71-74, 2008.

Strauss, R.du,T., Modeling of anomalous cosmic rays, M.Sc. dissertation, North-West University, South Africa, 2010.

Strauss, R.du,T., and Potgieter, M.S., The heliospheric transport and modulation of multiple charged anomalous oxygen revisited, Astron. Astrophys, 513, 1-6, 2010.

Strauss, R.du,T., Potgieter, M.S., Ferreira, S.E.S., and Hill, M.E., Modeling anomalous cosmic ray oxygen in the heliosheath, Astron. Astrophys., 522, 1-8, 2010.

Strauss, R.du,T., Potgieter, M.S., Kopp, A., and Büsching, I., Modeling the modulation of galactic and Jovian electrons by stochastic process, Astrophys. J., 735, 83-96, 2011.

Strong, A.W., Bennett, K., Bloemen, H., et al., Diffuse continuum gamma rays from the galaxy observed by COMPTEL, Atron. Astrophys, 292, 82-91, 1994.

Strong, A.W., Moskalenko, I.V., and Reimer, O., Diffuse continuum gamma rays from the Galaxy, Astrophys. J., 537, 763-784, 2000.

Strong, A.W., Moskalenko, I.V., and Ptuskin, V.S., Cosmic ray propagation and interaction in the galaxy, Annul. Rev. Nucl. Part. Sci., 57, 285-327, 2007.

Teufel, A., and Schlickeiser, R., Analytical calculation of the parallel mean free path of the heliospheric cosmic rays I. Dynamical magnetic slab turbulence and random sweeping model, Astron. Astrophys., 393, 703-715, 2002.

Webber, W.R., A comparison of predictions of a wavy neutral sheet drift model with cosmic ray data over a whole modulation cycle: 1976-1987, Astrophys. J., 349, 634-640, 1990.

Webber, W.R., A study of the propagation of cosmic rays in the galaxy using a Monte Carlo Diffusion Model- The source spectra of protons, Helium nuclei and electrons and locally observed spectra of these components, Proc. 26^{th} Inter. Cosmic Ray Conf., 4, D219-D221, 1999.

Webber, W.R., and Lockwood, J.A., Heliocentric radial intensity profiles of galactic cosmic rays measured by the MPI, Voyager and Pioneer spacecraft in solar cycles of opposite magnetic polarity, 109, A11101:1-7, 2004.

Webber, W.R., and Higbie, P.R., Limits on the interstellar cosmic ray electron spectra below ~1-2 GeV derived from the galactic polar radio spectrum and constrained by new Voyager 1 measurements, J. Geophys. Res., 113, A11106:1-10, 2008.

Whang, Y.C., and Burlaga, L.F., Anticipated Voyager crossing of the termination shock, 27, 1607-1610, 2000.

Williams, T., The influence of the wavy heliospheric neutral sheet on the modulation of cosmic rays (in Afrikaans), M.Sc. dissertation, Potchefstroom University, South Africa, 1990.

http://cohoweb.gsfc.nasa.gov.

http://pamela.roma2.infn.it.

http:/solarscience.msfc.nasa.gov/sunspotcycle.shtml.

htttp://ulysses.jpl.nasa.gov/.

http://voyager.jpl.nasa.gov/mission/interstellar.html.

http://wso.stanford.edu

www.oulu.fi/spaceweb/textbook/sun.html.

Acknowledgements

I would like to thank the following persons and institutions for support:

- God for giving me knowledge and letting me make it this far.
- Prof. M.S. Potgieter, my supervisor for assistance, his excellent leadership, motivation throughout this study. I would like also to thank him for giving more insight about the subject.
- Prof. S.E.S. Ferreira for his useful discussion and his assistance on various occasions.
- Mr. Sibusiso Nkosi for his assistance with the model and for useful discussion we had.
- Mrs. Petro Sieberhagen, Mrs. Lee-Aan van Wyk and Mrs. Elanie van Rooyen for all their administrative assistance.
- The Center for Space Research at the North West University, the South African National Research Foundation and the Department of Labour of South Africa for the financial support throughout my studies.
- Mr. Stephen Peter for proof reading my thesis.
- Mr. Katlego Moloto and Mrs. Sannet Taylor for their friendship motivation and support.

A special thanks to:

- My parents, Gerson and Elisah Nndanganeni, for their unconditional love and support throughout and your love for education.
- My sisters, Rudzani and Takalani Nndanganeni for their love and support.
- My grandmother Mrs. Maria Lithudzha for all her wisdom and love for education.

I dedicate this thesis to my daughter, Zwivhuya Vision Nemulodi